





## **Bridging the Terahertz Gap: High-Speed Photodiodes on Silicon Nitride**

**Dennis Maes**

Doctoral dissertation submitted to obtain the academic degree of  
Doctor of Electrical Engineering

### **Supervisors**

Prof. Bart Kuyken, PhD\* - Prof. Sam Lemey, PhD\* - Emilien Peytavit, PhD\*\*

\* Department of Information Technology  
Faculty of Engineering and Architecture, Ghent University

\*\* Université de Lille, France

December 2024



ISBN 978-94-6355-938-6

NUR 959

Wettelijk depot: D/2024/10.500/143

## **Members of the Examination Board**

### **Chair**

Prof. Filip De Turck, PhD, Ghent University

### **Other members entitled to vote**

Joan Ramirez, PhD, III-V Lab, France

Prof. Kasper Van Gasse, PhD, Ghent University

Prof. Geert Van Steenberge, PhD, Ghent University

Mathias Vanwollegem, PhD, Université de Lille, France

Prof. Xin Yin, PhD, Ghent University

### **Supervisors**

Prof. Bart Kuyken, PhD, Ghent University

Prof. Sam Lemey, PhD, Ghent University

Emilien Peytavit, PhD, Université de Lille, France



# Dankwoord

## *Acknowledgments*

Dit doctoraal proefschrift, *dit boekje*, vormt de samenvatting van mijn wetenschappelijk werk de voorbije jaren. Als onderzoeker heb ik naar antwoorden gezocht op wetenschappelijke vragen waar we tot voor kort geen antwoord op hadden. Als doctoraatsstudent heb ik heel veel mogen bijleren. Maar vooral: als ingenieur heb ik kunnen experimenteren, kunnen *prutsen op microschaal*, om tot deze antwoorden (en minstens evenveel nieuwe vragen) te komen. Dit alles was niet mogelijk geweest zonder het advies, de hulp, en de steun van collega's, familie en vrienden, die ik bij deze graag wil bedanken.

Op persoonlijk vlak wil ik al mijn familie en vrienden bedanken voor de onvoorwaardelijke steun en vertrouwen. Eerst en vooral mijn mama, die de wetenschappelijke vonk in mij heeft aangewakkerd. Was het niet door de eettafelgesprekken over je werk, dan wel de occasionele uitstapjes waar ik mee mocht naar de universiteit. Wat als kind een grijze wereld van glazen buisjes, luide machines en ingewikkelde praatjes leek, bleek later de kiem van mijn eigen wetenschappelijke nieuwsgierigheid. Ook mijn vriend Cedric wil ik expliciet bedanken, niet alleen om dit avontuur samen te doorstaan, maar ook voor je kritische blik op het academisch gebeuren. Jouw steun en reflecties hebben mij meer geholpen dan je misschien beseft. Tot slot verdienen ook mijn immer-trotse grootouders, die – soms op het gênante af – overal over hun kleinzoon stoefen, een bijzondere vermelding.

Op professioneel vlak dan, wil ik graag al mijn collega's bedanken. Zij hielpen me niet alleen door verschillende wetenschappelijke problemen heen, maar gaven ook kleur aan het dagelijks leven op bureau, in de cleanroom en het lab. Voor dit deel van het dankwoord schakel ik dan ook over naar de dagelijkse voertaal op bureau: English. Maybe not everyone knows this,

but all three of my supervisors were so kind to give me a desk and office space: two in Ghent, on the 3<sup>rd</sup> and 11<sup>th</sup> floor of iGent, and one in Lille, at IEMN. Most scientists know that the three-body problem is notoriously complex and lacks a closed-form solution. My PhD, however, turned out to be a real-life experimental setup of the "three-office problem."

Much like the three-body problem, the three-office is very sensitive to boundary and initial conditions. One such initial condition was my master thesis at the EM-group. Suddenly my thesis counselors became the nicest colleagues: thank you Olivier, Quinten, Laura and Igor! From the thesis room on the 11<sup>th</sup> floor I moved only a few doors down the hallway to an office full of extremely intelligent, and by times geeky, colleagues. Martijn, Pieter, Dries, Simon, Gert-Jan, Michiel, thank you for introducing me to the ADIV end-of-year puzzles. If I was stuck on an actual PhD research problem, I could easily forget this by spending hours making zero progress on a mathematics puzzle. A special thanks also goes to Arno and Nicolas. We started our PhDs together in the same group after completing our theses in the EM group. We stuck together, and now we finish them in the same year.

After a while, the stable state of the 11<sup>th</sup>-floor office was disturbed by an external boundary condition: as it turned out, getting an elevator up to the 11<sup>th</sup> floor takes a lot longer than taking the stairs to the 3<sup>rd</sup> floor. In this office at the Photonics group, I could also ask all my photonics-related questions. Artur, thank you for teaching me so much about cleanroom processing and photonics in general. I also want to thank Camiel for his guidance, sense of humor, and the focused-grating coupler GDS-cells I use to this date! Emmanuel, for making my day lighter with your battle against every evil corporate CEO. Valeria, for not giving in by drinking the black tar coming out of the machine on the 4<sup>th</sup> floor, and for enjoying a nice balanced cup of coffee together. Tom VA, for openly sharing your frustrations in other people in the most wholehearted way possible (and in doing so, making us feel just a little better about ourselves). Abdul, for sharing your profound wisdom in the field of photonics — I have yet to encounter a researcher or company in the field that you don't know! That said, the investment advice in a certain 'rock-solid' photonics company that didn't quite live up to its name. Ewoud, for reminding me in time it was almost time for lunch *\*clap\**, for coffee (15:00) and for weekend (Mondays at 10:00). And also Awanish, Emiel, Tom S, Robbe, Ruben and Patrick for making our third floor corner office the best office the PRG has ever seen.

Besides the fellow PhD and post-doc researchers, I also want to thank the support staff for helping me deal with all things related to HR, IT, measurement setups, etc. A special shout-out to Liesbet, Steven, Muneeb, and Elif. I cannot recall how often I have asked for a metal deposition or SEM pictures... Thank you!

I also want to thank all professors I had the pleasure to work with: Roel and Dries, for allowing me to try out new questions in the microphotonics course, Günther, for all the transfer-print knowledge, Guillaume, for measuring together with me in the lab, and also Wim, for being just as big an IT-nerd as I am.

Reinier, Margot, Mohammad, Nele, it was an honor to supervise your thesis projects. I hope a part of my enthusiasm was what drove you to start a PhD, and will continue to help you inspire future PhD researchers.

Reading back the previous paragraphs, it feels like I only scratched the surface of anecdotes that I collected over the past years. This list could continue with all colleagues in the other offices – on all floors and in all buildings – I can call my friends: Max, Tom VDK and Tom R, Stijn C and Stijn P, Laurens, Xin, Lam, Antonietta, Korneel... and everyone I might have – shame on me – forgotten.

Het laatste deel van dit dankwoord hou ik voor de meest belangrijke personen voor dit doctoraat, mijn promotoren, Bart, Sam en Emilien. Bedankt voor jullie visie en initieel onderzoeksidee aan mij toe te vertrouwen. Vijf jaar lang hebben jullie mij het vertrouwen gegeven om te werken aan dit prachtige project, ook op momenten dat – wat we ook probeerden – niks leek te lukken. Ik wil jullie ook bedanken om mij kennis te laten maken met de fascinerende wereld van academisch onderzoek. Enerzijds met tips over welke conferenties ik het best bijwoon, of advies voor het publiceren van resultaten. Anderzijds ook om me zorgeloos onderzoek te laten doen, zonder bekommernissen over onderzoeksfinanciering of universitaire bureaucratie (ook al is dat laatste niet volledig gelukt). Merci voor alles!

*Gent, 17 december 2024*  
*Dennis Maes*



# Contents

<b>Dankwoord</b>	<b>i</b>
<b>Contents</b>	<b>v</b>
<b>List of Acronyms</b>	<b>ix</b>
<b>Samenvatting</b>	<b>xv</b>
<b>Summary</b>	<b>xxiii</b>
<b>1 Introduction</b>	<b>1</b>
1.1 Integrated Photonics . . . . .	2
1.1.1 Micro-transfer printing . . . . .	3
1.2 Terahertz Communications . . . . .	5
1.2.1 On-chip Terahertz transmit array . . . . .	8
1.3 Contribution & Outline . . . . .	8
1.3.1 Thesis outline . . . . .	10
1.3.2 Publications . . . . .	11
<b>2 Design and fabrication of high-speed photodiodes for SiN</b>	<b>15</b>
2.1 Introduction . . . . .	16
2.2 Uni-traveling carrier photodiodes . . . . .	17
2.2.1 Working principle . . . . .	17
2.2.2 UTC epitaxial stack in this work . . . . .	18

2.3	Transforming diodes into coupons . . . . .	20
2.3.1	Micro-transfer printing ( $\mu$ TP) . . . . .	20
2.3.2	Coupon design . . . . .	21
2.3.3	Coupon fabrication details . . . . .	23
2.3.4	Considerations for contact metallization . . . . .	27
2.3.5	Considerations for low dark current . . . . .	29
2.3.6	Considerations for transfer-printing pickup yield . . . . .	30
2.3.7	Considerations for high responsivity . . . . .	32
2.4	Photodiode performance . . . . .	34
2.4.1	Dark current . . . . .	34
2.4.2	Responsivity & Saturation power . . . . .	37
2.4.3	Impedance and equivalent circuit . . . . .	37
2.4.4	Bandwidth . . . . .	40
2.5	Conclusion . . . . .	42
2.6	Ongoing and future Work . . . . .	43
<b>3</b>	<b>High-speed link at 300 GHz enabled by UTC photodiodes on SiN</b>	<b>47</b>
3.1	Introduction . . . . .	48
3.2	Experimental setup for a 300 GHz link . . . . .	49
3.3	System performance . . . . .	51
3.3.1	Error Vector Magintude (EVM) . . . . .	51
3.3.2	Results . . . . .	53
3.4	Conclusion . . . . .	58
3.5	Ongoing and Future work . . . . .	59
<b>4</b>	<b>A high-speed datacom link enabled by UTC photodiodes on SiN</b>	<b>61</b>
4.1	Introduction . . . . .	62
4.2	Experimental setup for an IM/DD link . . . . .	63
4.3	System performance . . . . .	64

---

4.3.1	From line rates to net bit rates . . . . .	65
4.3.2	Results . . . . .	66
4.4	Conclusion . . . . .	68
4.5	Towards coherent detection . . . . .	68
4.5.1	Chip design . . . . .	70
4.5.2	Fabrication (and its challenges) . . . . .	72
4.6	Future work . . . . .	75
<b>5</b>	<b>Conclusion and Outlook</b>	<b>77</b>
5.1	General Conclusions . . . . .	77
5.2	Outlook & Perspectives . . . . .	79
5.2.1	Improved UTC photodiode chiplets . . . . .	79
5.2.2	Complex SiN-based photonic systems . . . . .	79
5.2.3	Opto-antennas for THz communication . . . . .	80
5.2.4	Micro-transfer printing at high TRL . . . . .	80
<b>A</b>	<b>Fabrication recipes</b>	<b>81</b>
A.1	Dry etch recipes . . . . .	81
A.2	Wet etch recipes . . . . .	83
A.3	Lithography recipes . . . . .	84
A.4	Deposition recipes . . . . .	85
<b>References</b>		<b>R-1</b>



# List of Acronyms

## A

ASE	Amplified Stimulated Emission
AWG	Arbitrary Waveform Generator
AWGN	Additive White Gaussian Noise

## B

B2B	Band-to-band
BCB	Benzocyclobutene
BEOL	Back end of line
BER	Bit Error Rate
BPD	Balanced Photodiode
BOX	Buried Oxide
BTO	Barium Titanate

## C

CAGR	Compound Annual Growth Rate
CMOS	Complementary Metal-Oxide Semiconductor
CPW	Coplanar Waveguide
cTLM	circular Transfer Length Method

## D

DFB	Distributed-Feedback
DWDM	Dense Wavelength-Division Multiplexing

**E**

EDFA	Erbium-doped Fiber Amplifier
EME	Eigenmode Expansion
ESA	Electrical Spectrum Analyser
EVM	Error Vector Magnitude

**F**

FDTD	Finite-Difference Time-Domain
FEC	Forward Error Correction

**G**

GBd	Gigabaud
GSG	Ground Signal Ground

**H**

HD-FEC	Hard-Decision FEC
--------	-------------------

**I**

ICP	Induction Coupled Plasma
IM/DD	Intensity-Modulated Direct-Detection

**L**

LiDAR	Light Detection and Ranging
LN	Lithium Niobate
LO	Local Oscillator
LoCa	Local Cavity
LPCVD	Low-Pressure Chemical Vapor Deposition

**M**

MMI	Multi-Mode Interferometers
MPW	Multi-Project Wafer
MZM	Mach-Zehnder Modulator
MZI	Mach-Zehnder Interferometer
μTP	Micro-Transfer Printing

**N**

NGMI	Normalized Generalized Mutual Information
NRZ	Non-Return-to-Zero

**O**

OBFN	Optical Beamforming Network
OSA	Optical Spectrum Analyser

**P**

PA	Power Amplifier
PAM	Pulse Amplitude Modulation
PD	Photodiode
PDMS	Polydimethylsiloxane
PECVD	Plasma-Enhanced Chemical Vapor Deposition
PDM	Polarization-Division Multiplexing
PIC	Photonic Integrated Circuit

**Q**

Q-factor	Quality factor
QAM	Quadrature Amplitude Modulation
QPSK	Quadrature Phase Shift Keying

**R**

RF	Radio Frequency
RIE	Reactive Ion Etching
RMS	Root Mean Square
RoF	Radio over Fiber
RTO	Real-time Oscilloscope

**S**

SD-FEC	Soft-Decision FEC
SiN	Silicon Nitride
SMF	Single-Mode Fiber
SOA	Semiconductor Optical Amplifier
SOI	Silicon-on-Insulator
SRH	Shockley-Read-Hall

**T**

TAT	Trap-Assisted Tunneling
THz	Terahertz
TIA	Transimpedance Amplifier
TPA	Two-photon absorption
TRL	Technology readiness level

**U**

UTC	Uni-Traveling Carrier
-----	-----------------------

**V**

VNA	Vector Network Analyser
-----	-------------------------



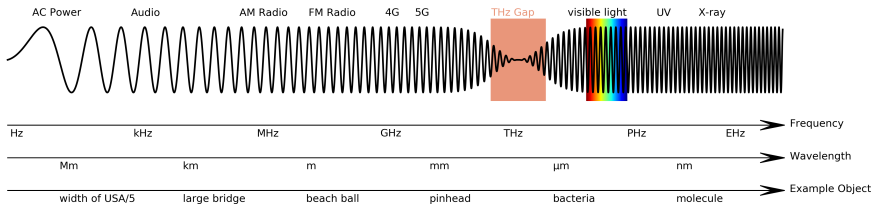


# Samenvatting

## Inleiding

In onze steeds meer geconnecteerde wereld blijft de vraag naar snellere en efficiëntere communicatienetwerken exponentieel groeien. We verwachten ook steeds meer van deze netwerken: ze moeten niet alleen een stabiele en snelle internetverbinding bieden, de apparaten die ermee verbonden zijn moeten ook compact en energiezuinig zijn. Deze eisen drijven de huidige technologieën tot het uiterste, wat onderzoekers aanzet om met creatieve oplossingen te komen. Twee opkomende vakgebieden zijn hierin cruciaal: de geïntegreerde fotonica en draadloze terahertz (THz) communicatie. Geïntegreerde fotonica brengt de kracht van licht naar het chipniveau, vergelijkbaar met hoe elektronische circuits de computertechnologie revolutionair veranderden. Tegelijkertijd maakt THz-communicatie gebruik van een grotendeels onbenut deel van het elektromagnetische spectrum met immense bandbreedtes. Met deze bandbreedtes zijn in theorie datasnelheden mogelijk die met kop en schouders uitsteken boven de mogelijkheden van huidige draadloze technologieën. Dit PhD-onderzoek bevindt zich op de intersectie van deze twee *cutting-edge* domeinen. Hoewel ze misschien niet enorm verschillend lijken, biedt hun combinatie unieke opportuniteiten voor innovatie en wetenschappelijke vooruitgang.

Geïntegreerde fotonica, het eerste domein, maakt het mogelijk om optische componenten te verkleinen tot nano- en micrometerschaal, en biedt zo de mogelijkheid om allerhande functionaliteiten te combineren op één enkele chip. In dit veld springt *Silicon Photonics* (inclusief de siliciumnitridegebaseerde variant hiervan) er uit dankzij zijn fabricage die CMOS-compatibel is. Een uitgebreid ecosysteem van (elektronische) chipfabrieken – zogenaamde CMOS-fabs – faciliteert op die manier het productieproces van lichtgebaseerde chips op een schaalbare manier. Hoewel de fotonische chips op basis van siliciumnitride erg veel voordelen bieden, ontbreken er enkele belangrijke functionaliteiten, bv. de mogelijkheid om optische signalen rechtstreeks om te zetten naar elektrische signalen. In dit proefschrift wordt de techniek *micro-transfer printing* ( $\mu$ TP) toegepast om dit probleem aan te pakken.  $\mu$ TP maakt het mogelijk om componenten uit verschillende



*Figuur 1: Het THz spectrum omvat frequenties boven 300 GHz en biedt immense bandbreedtes voor draadloze communicatie.*

materialen en technologieën (de 'bron'-technologie) te combineren op één doelplatform, in dit geval siliciumnitride. Zo'n combinatie techniek staat bekend als heterogene integratie. Met sub-micron precisie kunnen er kleine chips met een specifieke functie, zogenaamde chiplets, getransfereerd worden naar één grote chip. Op die manier brengen we de beste eigenschappen van meerdere technologische platformen samen tot één complexe fotonisch geïntegreerde schakeling.

Het THz-spectrum biedt een enorm potentieel voor communicatie met ultra-hoge snelheid, door de grote bandbreedtes die beschikbaar zijn in de frequentiebanden boven 300 GHz. Het benutten van dit potentieel is echter niet zo simpel: deze straling met korte golflengtes (<1 mm) wordt sterk verzwakt door de atmosfeer – zeker bij regenweer. Ook het genereren en detecteren van deze signalen is erg moeilijk: op dit probleem richt dit doctoraatsonderzoek zich en wendt zich hierbij tot de THz-fotonica. Centraal in deze fotonische aanpak staat de techniek van *photomixing*: door twee lasers met een net iets andere golflengte te laten interfereren op een ultrasnelle fotodetector, wordt er een signaal in het THz-bereik, proportioneel aan het frequentieverschil van de twee lasers, gegenereerd.

In dit doctoraatsonderzoek ontwikkel ik een nieuw type component dat het genereren van THz-signalen mogelijk maakt op een siliciumnitride fotonische chip. Ik ga in op het ontwerp (rakelingse koppeling aan een golfgeleider) en de fabricage (met behulp van micro-transfer printing) van hogesnelheidsfotodetectoren, alsook hoe deze componenten zijn opgemeten en hun (baanbrekende) snelheden zijn geverifieerd. Vervolgens toon ik ook aan hoe deze component bijdraagt tot het succes van complexe communicatiesystemen door middel van twee systeem-niveau tests. Het eerste experiment zet een THz-link op rond de centrale frequentie van 300 GHz waarbij datasnelheden gehaald worden van meer dan 100 Gbit/s. In het tweede experiment wordt een optische link opgezet, zoals in een datacenter, met een glasvezel van 200 m, waarbij datasnelheden tot 300 Gbit/s worden gehaald.

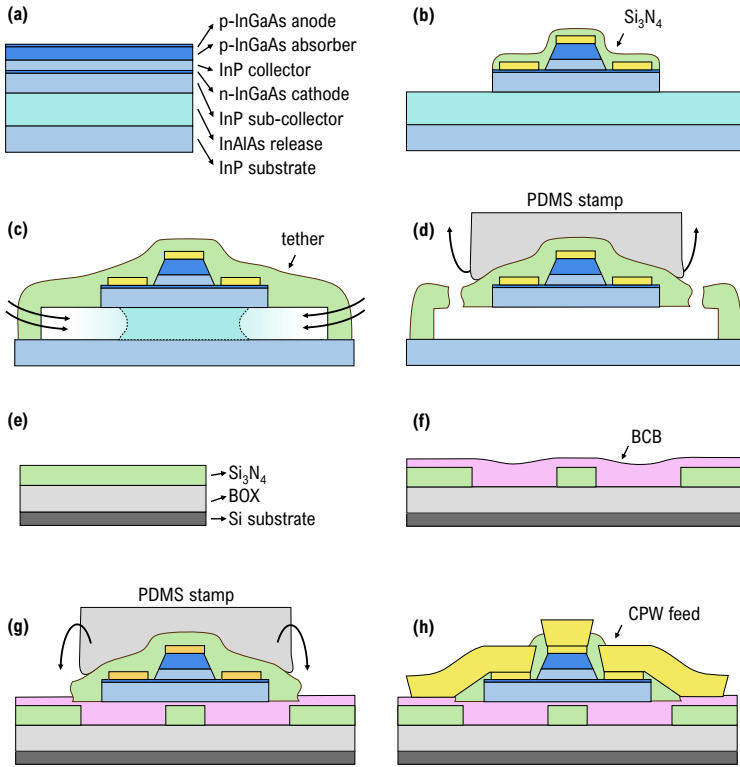
## Resultaten

Om ultrasnelle fotodetectoren naar een SiN-gebaseerd fotonisch platform te brengen, kijken we naar een type III/V-fotodetector met een uniek ladingstransportmechanisme: de *uni-traveling carrier* (UTC) fotodiode. In een UTC-fotodiode bewegen alleen elektronen door het depletiegebied, terwijl gaten vast blijven zitten in de p-type laag. Omdat gaten een veel lagere mobiliteit hebben dan elektronen, kan er een significante verbetering behaald worden in de *transit-time* beperking. Vergeleken met een meer klassieke p-i-n fotodiode, wordt de taak van het genereren van ladingen en het transporteren van ladingen gesplitst in twee afzonderlijke lagen: een p-type absorptielaag (waar de generatie gebeurt) en een niet-absorberende transportlaag van het intrinsieke type (niet gedoteerd). De tweede belangrijke bandbreedtebeperking is de RC-tijdconstante. Deze kan geminimaliseerd worden door het actieve gebied van de fotodiode zo klein mogelijk te maken.

Door het ontwerp zo aan te passen dat de fotodiode dezelfde vorm heeft als de golfgeleider en deze raketings raakt, kan de actieve oppervlakte drastisch verkleind worden, zonder in te boeten op de totale hoeveelheid geabsorbeerd licht – en dus de responsiviteit van de fotodiode.

De fabricage van de UTC-fotodiode chipelets begint op hun oorspronkelijke III/V-halfgeleidersubstraat, waarbij zorgvuldig aandacht is besteed aan het ontwerp van de verschillende epitaxiale halfgeleiderlagen, het type contactmetallisatie en de mesa-ets. Figuur 2 vat de grote stappen in het fabricageproces samen:

1. Eerst wordt de fotodiode gemaakt op zijn oorspronkelijk substraat (a) met optimalisaties voor het  $\mu$ TP-proces. Dit omvat een twee-staps mesa-etsproces waarbij een droge (ICP) en natte ets gecombineerd worden. De nu reeds volledig functionele fotodiode wordt hierna gepassiveerd met een encapsulatielaag van SiN (b).
2. De chipelets worden vervolgens getransformeerd in printklare coupons door *tethers* te definiëren die de coupon vasthouden zodra de opofferlaag eronder weg-geëtsd wordt (c).
3. De SiN-chip wordt apart gemaakt (e), met laag-verlies golfgeleiders en roosterkoppelaars, waarna een dun laagje BCB (f) wordt gedeponeed dat zorgt voor een betere adhesie tijdens het transfer-printen.
4. Ten slotte worden de fotodiode-coupons ge-transfer-print op de SiN-chip (g), gevolgd door enkele aanvullende stappen om de elektrische contacten te maken (h).

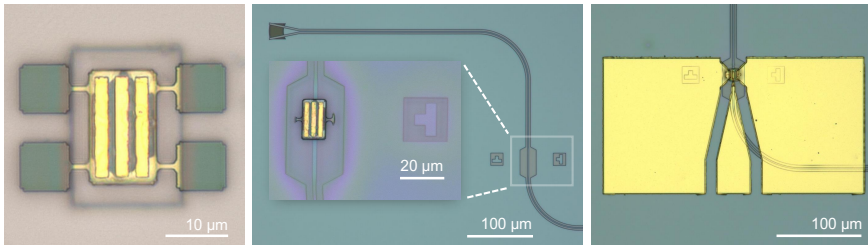


Figuur 2: De verschillende fabricagestappen om een golfgeleider-gekoppelde UTC-fotodiode te maken.

De resulterende chip wordt getoond in Figuur 3: links is de coupon afgebeeld op het oorspronkelijke substraat, in het midden is de  $\text{SiN}$ -chip te zien voor en na (inzet) het transfer-printen, en helemaal rechts de afgewerkte chip met de elektrische contactlagen.

De afgewerkte fotodiodes werden opgemeten en bereikten een responsiviteit van  $0.3 \text{ A/W}$  bij  $1550 \text{ nm}$ , wat overeenkomt met een externe kwantumefficiëntie van  $23 \%$ . Verder werd er een donkerstroom van  $10 \text{ nA}$  gemeten bij een aangelegde spanning van  $-1 \text{ V}$ , wat wijst op een geringe bijdrage aan ruis. Het meest indrukwekkende resultaat is echter de uitzonderlijk hoge bandbreedte van deze fotodiodes: bij een spanning van  $-1 \text{ V}$  behalen ze een  $3\text{-dB}$  bandbreedte van  $155 \text{ GHz}$ , terwijl dit zelfs bij  $0 \text{ V}$  nog  $135 \text{ GHz}$  bedraagt.

Deze hoge bandbreedtes zijn een significante vooruitgang ten opzichte van eerdere  $\text{SiN}$ -geïntegreerde fotodetectoren (Q. Yu, Opt. Express, 2020) en



Figuur 3: SiN-gebaseerde fotonisch geïntegreerde chip met een ge-transfer-printe UTC fotodiode.

overtreffen zelfs sommige Silicon-on-Insulator (SOI) tegenhangers in hun prestaties (S. Lischke, Nat. Photonics 2021) op 0 V.

Deze resultaten bevestigen dat ge-micro-transfer-printe UTC-fotodiodes een veelbelovende technologie vormen voor snelle optische detectie in SiN-gebaseerde fotonische chips. Hierdoor worden nieuwe toepassingen mogelijk gemaakt in telecommunicatie en andere velden die ultrasnelle fotodetectie vereisen.

Voortbouwend op de succesvolle resultaten van deze hogesnelheids UTC-fotodiodes, demonstreren we de praktische toepasbaarheid van deze componenten in een communicatielink die werkt rond 300 GHz. Met succes hebben we een fotonische zender opgezet die gebruikmaakt van de geïntegreerde UTC-fotodiode om hoogfrequente signalen te genereren. Met een reeks experimenten hebben we de prestaties en limieten van het systeem bepaald, waarbij indrukwekkende datasnelheden van meer dan 100 Gbit/s werden bereikt met zowel QPSK- als 16-QAM-modulatieschema's. Belangrijk om op te merken is dat de signaalkwaliteit hoog blijft bij hoge symboolsnelheden. Dit toont het potentieel aan voor toekomstige THz-communicatiesystemen.

Hoewel THz-communicatie de oorspronkelijke motivatie was voor ons onderzoek, hebben we nu een component die potentieel ook andere taken binnen de telecommunicatie kan vooruithelpen. Om dit te verifiëren, hebben we een glasvezelverbinding over korte afstand (200 m) binnen de C-band (1550 nm) tot stand gebracht met de UTC-fotodiode geplaatst aan de kant van de ontvanger. Verschillende systeemconfiguraties werden getest: variaties in symboolsnelheden van 128 tot 200 GBd en meerdere constellatieformaten van het simpele twee-niveaus NRZ tot hogere level PAM-8 constellaties. Op basis van de genormaliseerde gegeneraliseerde wederzijdse informatie (NGMI) van de ontvangen symbolen, berekenen we vervolgens de netto haalbare datasnelheden. Bij deze datasnelheid wordt rekening gehouden met de vereiste *overhead* voor error-correctie. Deze resultaten bevestigen niet alleen het potentieel van ge-transfer-printe fotodiodes

op SiN voor snelle optische communicatie an sich, maar benadrukken ook hun veelzijdigheid in verschillende toepassingsdomeinen.

## Conclusie

Dit PhD-onderzoek heeft aanzienlijke vooruitgang geboekt in het veld van de geïntegreerde fotonica voor terahertz (THz) communicatie. De belangrijkste prestatie ligt in het succesvolle ontwerp en fabricage van hogesnelheids *uni-traveling carrier* (UTC) fotodiodes, en hun integratie op siliciumnitride-gebaseerde fotonische chips met behulp van micro-transfer printing. Dit werk heeft geresulteerd in verschillende noemenswaardige prestaties:

1. De (tot nu toe) snelste fotodiode geïntegreerd op een SiN-platform. Ten opzichte van de huidige state-of-the-art fotodiodes die heteroëen geïntegreerd zijn op SiN is dit een achtvoudige verbetering van het vorige snelheidsrecord.
2. De snelste geïntegreerde fotodiode bij 0 V, alle fotonische platformen in acht genomen.
3. Een succesvolle demonstratie van communicatie in de THz-band. Hierbij werden onze UTC-fotodiodes gebruikt in een datalink op 300 GHz waarbij datasnelheden van meer dan 100 Gbit/s gehaald werden.
4. Een succesvolle demonstratie van optische glasvezellink op C-band link die netto datasnelheden haalde van meer dan 350 Gbit/s haalde, en symboolsnelheden tot wel 200 GBd.

Deze resultaten onderstrepen het potentieel van onze heteroëen geïntegreerde fotonische componenten voor de volgende generatie van communicatiesystemen. Hierbij wordt ingespeeld op de groeiende vraag naar verhoogde bandbreedte in zowel draadloze als optische netwerken. We vestigen ge-transfer-printe UTC-fotodiodes als een veelbelovende technologie voor snelle optische detectie in SiN fotonische platforms, wat mogelijk nieuwe toepassingen mogelijk maakt in telecommunicatie en andere velden die ultrasnelle fotodetectie vereisen.

Met het oog op de toekomst dienen zich verschillende spannende wegen aan voor verder onderzoek en ontwikkeling: van incrementele verbeteringen aan het ontwerp en de fabricage van de in dit werk gepresenteerde devices, over het uitbreiden van de functionaliteit van de SiN PIC, tot het realiseren van een volledig geïntegreerd sub-THz opto-antenne zendsysteem. Dit

proefschrift is een stap in de ontwikkeling van de volgende generatie geïntegreerde fotonische devices voor THz-communicatie, maar het is belangrijk om te erkennen dat er nog een lange weg te gaan is. Terwijl ik en andere onderzoekers de grenzen van snelheid, efficiëntie en integratie in fotonische devices blijven verleggen, brengt elke incrementele vooruitgang ons dichterbij het realiseren van het volledige potentieel van THz-communicatie.



# Summary

## Introduction

In our increasingly connected world, the demand for faster, more efficient communication continues to grow exponentially. We also expect more of these networks: not only should they provide stable, high-speed connections to the internet, but the devices connected to them should also be compact and energy efficient. These demands push current technologies to their limits, prompting researchers to explore new frontiers in engineering. At the forefront of this exploration are two emerging fields: integrated photonics and terahertz (THz) communication. Integrated photonics brings the power of light generation and manipulation to the chip scale, much like how electronic integrated circuits revolutionized computing. Meanwhile, THz communication taps into a largely unused portion of the electromagnetic spectrum, promising data speeds far beyond current wireless technologies. This PhD research is positioned at the intersection of these two cutting-edge domains. While they may not seem vastly different, their combination offers a unique playground for innovation and scientific advancement.

Integrated photonics, the first domain, enables the creation of compact, cost-effective devices by shrinking optical functionalities onto a single chip. Silicon Photonics (including Silicon Nitride-based platforms) stand out in this field, owing its popularity to the compatibility with CMOS manufacturing processes. A vast ecosystem of electronic chip foundries – so-called CMOS fabs – facilitates the seamless integration of optical and electronic components in a scalable manner. Despite many great properties of Silicon Nitride platforms, some crucial features, like photodetection to convert optical into electrical signals, are lacking natively. To overcome this obstacle, I turn to micro-transfer printing ( $\mu$ TP). This versatile technique allows for the combination of multiple material platforms during fabrication, a process known as heterogeneous integration. With sub-micron-scale precision,  $\mu$ TP transfers pre-fabricated chiplets to extend the functionalities of a photonic integrated circuit (PIC).

Secondly, the THz range holds immense potential for ultra-high-speed com-

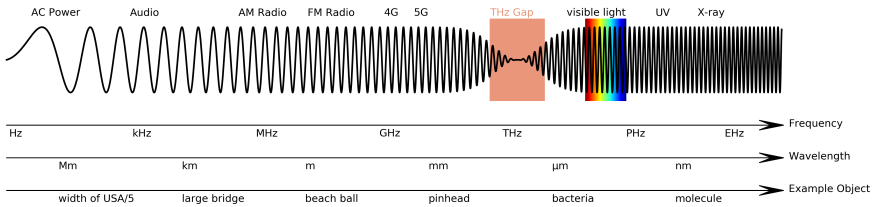


Figure 4: The THz spectrum starts at 300 GHz and offers immense bandwidths for wireless communication.

munications and sensing applications. More precisely, the portion of the broad THz range closest to the microwave spectrum, the so-called sub-THz range (100 GHz to 1 THz) offers vast bandwidths for wireless communication. However, harnessing this potential is not without challenges. Difficult atmospheric propagation and the complexities of generating and detecting THz signals present significant hurdles. To overcome these obstacles, this research shifts its attention to THz photonics. Central to this approach is the technique of photomixing: by beating two lasers with slightly different, yet well-controlled, frequencies on an ultra-high-speed photodetector, a signal in the sub-THz range is generated.

In this work, novel devices are presented that enable the generation of sub-THz signals on a Silicon Nitride PIC. I present the design and fabrication of high-speed waveguide-coupled photodetectors using micro-transfer printing, as well as the characterization of their record-high bandwidths. The capabilities of these devices are then demonstrated in a sub-THz link at 300 GHz, achieving data rates over 100 Gbit/s, and in a short-reach optical datacom link, with data rates going up to 300 Gbit/s.

## Results

To bring ultra-fast photodetectors to the SiN platform, I look into a type of III/V photodetector with a unique carrier transport mechanism: the uni-traveling carrier (UTC) photodiode. In a UTC photodiode, only electrons travel through the depletion region while holes are confined to the p-type layer. Owing to the higher mobility of electrons, a significant improvement in the transit-time limitation is achieved. Compared to a more classical p-i-n photodiode, the carrier generation and transport is split into two separate layers: a p-type absorption layer and a non-absorbing intrinsic type transport layer. A second important bandwidth limitation is the RC time constant, which can be minimized by making the active region as small as possible. Without sacrificing the amount of light absorbed – and thus

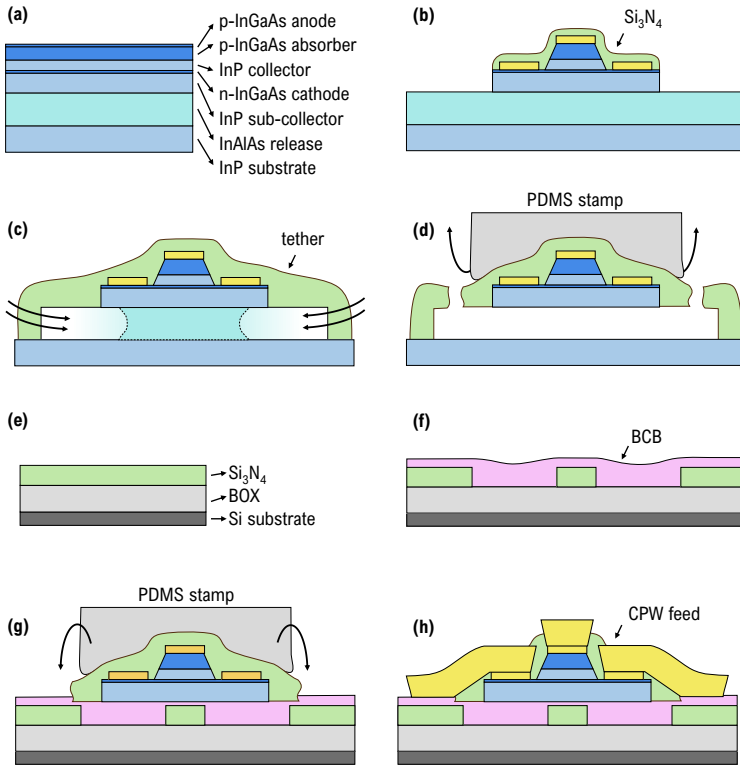


Figure 5: The different fabrication steps to create a waveguide-coupled UTC photodiode.

responsivity of the photodiode –, I relied on a narrow waveguide-coupled design.

Fabrication of the UTC photodiode chiplets starts on their native III-V substrate, where careful consideration was given to the epitaxial stack design, contact metallization, and mesa etching. Figure 5 summarizes all necessary steps in the fabrication process:

1. First, the photodiode is processed on its native substrate (a), which was optimized for the  $\mu$ TP process. This involves a two-step mesa etching process, combining ICP dry etching and wet etching, to create the waveguide-shaped active region. The fully-functional photodiode is passivated in a SiN encapsulation layer (b).
2. The chiplets are then transformed into transferable coupons by defining tethers and underetching the sacrificial release layer (c).
3. The SiN PIC was fabricated separately (e), featuring low-loss waveguide-

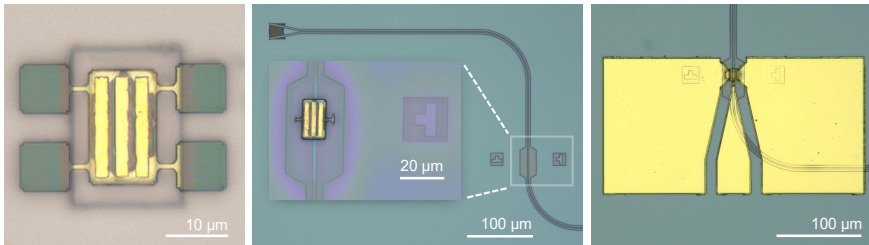


Figure 6: Example of a SiN photonic integrated circuit (PIC) with a transfer-printed UTC photodiode.

guides and grating couplers, and covered with a thin layer of BCB (f) for better adhesion during transfer-printing.

4. Finally, the photodiode coupons are transfer-printed onto the SiN chip (g), followed by post-processing steps to create electrical contacts (h).

The final chip can be seen in Figure 6: on the left, the coupon is shown on the source chip, in the middle the SiN PIC can be seen before and after (inset) transfer-printing, and on the right the fully post-processed chip is shown.

The resulting devices were characterized and achieved a responsivity of  $0.3 \text{ A/W}$  at  $1550 \text{ nm}$ , corresponding to an external quantum efficiency of 23%. Dark currents of  $10 \text{ nA}$  were measured at reverse bias voltages greater than  $-1 \text{ V}$ , indicating low noise contribution. And most notably, these photodiodes exhibited record-breaking bandwidths. At  $-1 \text{ V}$  bias, they achieved a 3-dB bandwidth of  $155 \text{ GHz}$ , while reaching  $135 \text{ GHz}$  even at zero bias.

These values represent a significant advancement over previous SiN-integrated photodetectors (Q. Yu, *Opt. Express*, 2020) and even surpass some of the best Silicon-on-Insulator (SOI) counterparts at their zero bias performance (S. Lischke, *Nat. Photonics* 2021) These results establish micro-transfer-printed UTC photodiodes as a promising technology for high-speed optical detection in SiN photonic platforms, potentially enabling new applications in telecommunications, microwave photonics, and other fields requiring ultra-fast photodetection.

Building upon the successful results of these high-speed UTC photodiodes, I demonstrate the practical application of these devices in a cutting-edge  $300 \text{ GHz}$  communication link. A photonic transmitter utilizing the integrated UTC photodiode is successfully implemented to generate high-frequency signals. Through a series of experiments, the system's performance was characterized, achieving impressive data rates with both QPSK

and 16-QAM modulation schemes. Notably, our setup maintained good signal quality even at high symbol rates, demonstrating the potential of integrated photonic devices for next-generation THz communications.

Even though sub-THz communications were the initial motivation for our research, the proposed photodiode could potentially also advance other fields of communication. To test this, a short-reach (600 m) fiber link at C-band (1550 nm) was set up, with the UTC photodiode at the receiver side. Various system configurations were tested: variations in symbol rate from 128 to 200 GBd and multiple constellation formats from two-level NRZ to higher level PAM-8 schemes. Based on the normalized generalized mutual information (NGMI) of the received symbols, the net achievable bit rates are then determined. This is the bit rate taking into account the required overhead for forward error correction (FEC). These results not just validate the potential of transfer-printed photodiodes on SiN for high-speed baseband optical communications but also highlight their versatility across different application domains.

## Conclusion

This PhD thesis has made significant strides in advancing the field of integrated photonics for terahertz (THz) communications. The primary achievement lies in the successful design and fabrication of high-speed uni-traveling carrier (UTC) photodiodes, and their integration on a silicon nitride (SiN) photonic platform using micro-transfer printing technology. This work has resulted in several noteworthy accomplishments:

1. The demonstration of the fastest photodiode integrated on a SiN platform to date. This represents an approximately eight-fold improvement over the current state-of-the-art photodiodes heterogeneously integrated on SiN.
2. The fastest zero-bias photodiode across all integrated photonic platforms, surpassing even the best Silicon-on-Insulator (SOI) counterparts.
3. In sub-THz communications, I successfully operated these UTC photodiodes at 300 GHz, achieving data rates beyond 100 Gbit/s.
4. For fixed access interconnects, a short-reach C-band link was demonstrated, supporting net data rates exceeding 350 Gbit/s, as well as transmissions with symbol rates up to 200 GBd.

These results underscore the potential of our heterogeneously integrated photonic devices for next-generation communication systems, addressing

the growing demand for increased bandwidth in both wireless and optical networks. They establish micro-transfer-printed UTC photodiodes as a promising technology for high-speed optical detection in SiN photonic platforms, potentially enabling new applications in telecommunications, microwave photonics, and other fields requiring ultra-fast photodetection.

Looking to the future, several exciting avenues for further research and development emerge: from incremental improvements to the design and fabrication of the devices presented in this work, over extending the functionality of the SiN PIC, to realizing a fully integrated sub-THz opto-antenna transmit system. This PhD thesis represents a step in the development of the next generation of integrated photonic devices for THz communications, but it is important to recognize a long journey is still ahead. As other researchers and I continue to push the boundaries of speed, efficiency, and integration in photonic devices, each incremental advancement brings us closer to realizing the full potential of THz communications.

# 1

## Introduction

---

<b>1.1</b>	<b>Integrated Photonics</b> . . . . .	<b>2</b>
1.1.1	Micro-transfer printing . . . . .	3
<b>1.2</b>	<b>Terahertz Communications</b> . . . . .	<b>5</b>
1.2.1	On-chip Terahertz transmit array . . . . .	8
<b>1.3</b>	<b>Contribution &amp; Outline</b> . . . . .	<b>8</b>
1.3.1	Thesis outline . . . . .	10
1.3.2	Publications . . . . .	11

---

Modern science increasingly values and stimulates interdisciplinary research. This approach, which involves the combination of theoretical knowledge, practical know-how, and perspectives from multiple disciplines, is lauded for driving innovation and its ability to solve complex problems that lie beyond the scope of a single field.

While integrated photonics and THz communication might not represent disparate fields in the broad sense of interdisciplinary research, their combination nonetheless offers a rich ground for innovation and scientific advancement. THz communication, with its promise of ultra-high-speed wireless data transmission, provides the motivation and context for this research. It presents a set of challenges and opportunities that drive the exploration of new technologies and approaches. Integrated photonics, on the other hand, offers the technological framework and toolset within which

these challenges can be addressed. It provides the means to manipulate light at the chip scale, and the technological framework to work on and extend for the development of high-performance THz components and systems. The interplay between these two fields creates a unique research space, within which this PhD is positioned.

It is not our goal to educate you on both topics by providing exhaustive, historically complete summaries of both topics – let alone of the vast and complex field of telecommunications and microfabrication they are a part of. Nevertheless, for readers of all backgrounds, a brief introduction to both topics of engineering cannot be withheld. Our aim is to provide you with the necessary context to appreciate the research presented in this thesis. By understanding the basics of these two areas and their potential for synergy, we can better grasp the significance of the work undertaken and its potential impact on future communication technologies.

In the next section (Section 1.1), we will introduce the concept of chips working on light, rather than the electrons moving around in the microchips you might be more familiar with, as well as the novel technology of micro-transfer printing that is used to extend the functionality of these chips even further. The second introductory section (Section 1.2) will present the concept of THz communications, a technology under development due to the ever-increasing demand for wireless bandwidth, and an envisioned THz transmitter based on photonic technologies.

## 1.1 Integrated Photonics

The field of integrated photonics has revolutionized the way we manipulate and control light, offering a stark contrast to traditional bulk optics. While bulk optical systems rely on discrete, often large components such as lenses, mirrors, and beam splitters, integrated photonics miniaturizes these functionalities onto a single chip. This paradigm shift enables the creation of compact, robust, and cost-effective photonic devices. By leveraging semiconductor fabrication techniques, one can create a chip with channels that confine and guide the light, so-called waveguides on a photonic integrated circuit (PIC). Depending on the material platform used, one can not only guide the light through the chip but also generate light with integrated lasers, manipulate the phase or amplitude of the light using a modulator, or convert light into electrical signals by means of photodetectors.

Unlike electronics, which relied on Silicon for chips from its early days

on, photonic chips are made out of a wide range – often exotic – materials: Indium Phosphide (InP), Gallium Arsenide (GaAs), Lithium Niobate (LN), Barium Titanate (BTO)... each one with its own benefits and drawbacks. Silicon Photonics (SiN) however, has emerged as a particularly promising material platform due to its compatibility with existing CMOS (Complementary Metal-Oxide-Semiconductor) fabrication processes. This compatibility is a game-changer, as it allows silicon photonic devices to be manufactured using the same infrastructure and techniques developed for the microelectronics industry over decades. The ability to leverage CMOS fabs offers several significant advantages: it facilitates easier scaling of production, dramatically reduces costs through economies of scale, and enables the seamless integration of photonic and electronic components on a single chip. Moreover, the maturity of silicon processing techniques ensures high yield and reliability, making silicon photonics an attractive choice for both research and commercial applications.

The versatility of silicon photonics, including its silicon nitride (SiN) variant, has led to its adoption across a diverse range of applications. In telecommunications, silicon photonic devices form the backbone of high-speed, long-distance data transmission systems, enabling faster and more efficient internet connectivity. The field of sensing has been transformed by silicon photonic biosensors, capable of detecting minute quantities of biomolecules for medical diagnostics and environmental monitoring. In microscopy, silicon photonics enables super-resolution imaging techniques, pushing the boundaries of what we can observe at the nanoscale. LiDAR (Light Detection and Ranging) systems for autonomous vehicles and robotics benefit from the compact and low-cost nature of silicon photonic chips. Perhaps most excitingly, silicon photonics is playing a crucial role in the development of quantum computing hardware, offering a scalable platform for manipulating quantum states of light. As research continues, the potential applications of silicon photonics and SiN-based devices continue to expand.

### 1.1.1 Micro-transfer printing

Micro-transfer printing ( $\mu$ TP) is a technology that enables the transfer of pre-fabricated devices or materials from a source substrate to a target substrate with micron-scale precision. These devices are often called coupons – as an analogy to paper discount coupons.

Micro-transfer printing is a versatile technology for heterogeneous integration, i.e. combining multiple material platforms during the fabrication

process. Hybrid integration, on the other hand, is often defined as combining devices from different material platforms during the packaging step. One of the biggest benefits of micro-transfer printing in that sense, is that source and target technology remains largely decoupled. Because the material or device transfer can be postponed to one of the final fabrication steps, only minimal changes to both source and target platform technologies are needed. As such it also allows the combination of technologies that have a different maturity level, i.e. a highly novel device – like the research-grade coupons described in this work – can be printed on a commercial chip, made in a large volume fab [1,2].

Other benefits of micro-transfer printing for photonic integration include:

- High accuracy: Coupons can be printed with a misalignment well below  $1\ \mu\text{m}$ . Especially for optical evanescent coupling this is important.
- Multi-material integration: Various materials and pre-fabricated chiplets can be combined on a single substrate, regardless of their growth compatibility.
- Flexible source wafer processing: Devices can be fully processed on their native substrates before transfer, allowing for optimal material quality and device performance.
- Efficient III/V usage: Only the required source material, e.g. expensive III/V wafers, is used, leading to more efficient use of these expensive materials compared to full wafer bonding.
- Parallelization possible: Multiple devices can be transferred simultaneously using array stamps, increasing throughput and scalability.

The actual process of micro-transfer printing itself involves the use of an elastomeric stamp, often made of polydimethylsiloxane (PDMS), to pick up devices from the source wafer and place them onto the target wafer. This transfer is made possible by controlling the adhesion forces between the stamp and the devices through careful manipulation of the stamp's velocity, shear movement, and force, during the picking and placing steps. The adhesion to the stamp only relies on Van der Waals forces.

For example, Figure 1.1 shows a schematic visualization of micro-transfer printing with a  $2 \times 2$  array of coupons being picked from a smaller wafer (e.g. a 2" III/V-semiconductor wafer) and printed onto a larger wafer (e.g. a 4" Silicon Photonic wafer).

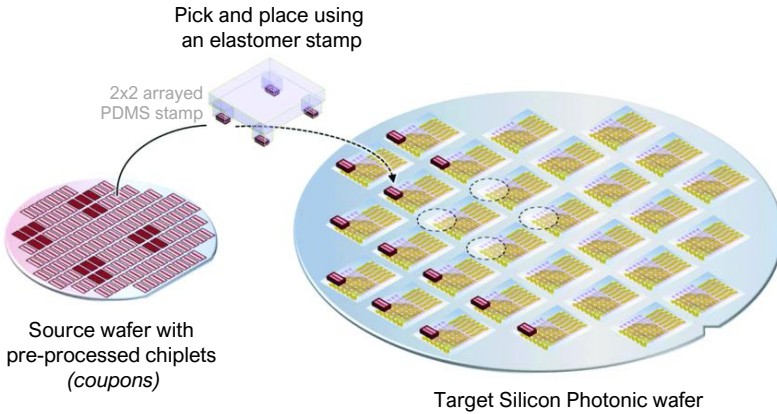


*Figure 1.1: Micro-transfer printing is a technology for heterogeneously integrating pre-processed coupons (e.g. III/V-semiconductor photodiodes) on a target photonic integrated circuit (e.g. SiN) using an elastomer stamp.*

In recent years, this technology has become very popular for all the reasons listed above, and a wide range of novel photonic devices has been enabled by it: Vertical-cavity surface-emitting lasers (VCSELs) [3], high-performance grating couplers [4], external cavity lasers [5], modulators based on transfer-printed Lithium Niobate (LN) [6], photodiodes at 870 nm [7], and many more [2]. Also in this work, it is a key technology to create novel photodiodes. In Chapter 2 you can read all details on how micro-transfer printing was used to integrate high-speed III/V photodiodes on a Silicon Nitride photonic platform.

## 1.2 Terahertz Communications

The electromagnetic spectrum encompasses all types of radiation, ranging from low-frequency radio waves to high-energy gamma rays. Within this vast spectrum lies a region known as the Terahertz (THz) gap, commonly defined as the frequency range between 0.1 THz and 10 THz (resp. wavelengths from 3 mm to 30  $\mu\text{m}$ ). This is illustrated in Figure 1.2. This band bridges the gap between microwaves and infrared light, occupying a unique position that has long been underutilized due to technological limitations [8–10]. On the one hand, THz waves face difficulties in generating and detecting such relatively long wavelengths using typical optical techniques. On the other hand, electronic devices struggle to operate at

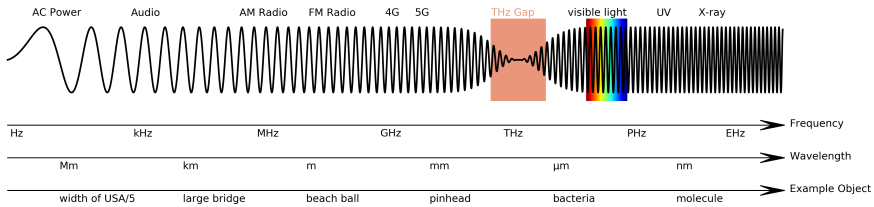


Figure 1.2: In the vast range of the electromagnetic spectrum, the terahertz gap (1–10 THz) lies between the microwave frequencies and infrared light. (add ref or remake figure)

such high frequencies due to parasitic capacitances and transit time effects.

The sub-THz range, generally considered to go up to 1 THz (or have wavelengths below 3 mm), is of particular interest for wireless communication because it holds immense potential for ultra high-speed communications due to the large available bandwidths [11]. It is a stepping stone from the upper end of the microwave range and goes beyond what is typically defined as the millimeter wave (mmWave) spectrum, i.e. the spectral range defined from 30 GHz up to 300 GHz (or wavelengths starting at 1 cm going down to 1 mm).

As data demands continue to grow exponentially, current communication technologies operating at lower frequencies – even those used in current 5G networks – are approaching their capacity limits. The Ericsson annual mobility report – one of the largest wireless technology manufacturers – predicts that global monthly data traffic will reach 400 EB (this is 400 million TB) by 2028. This corresponds to a Compound Annual Growth Rate (CAGR) of around 20 % [12] between 2029 and 2029. In the same company’s Microwave Outlook report, it is remarked that E-band (60 - 90 GHz) has become a commonplace for mobile backhaul, and they openly wonder how long before even higher bands (in the sub-THz region) are needed [13].

THz communications offer the promise of data rates in the terabit-per-second (Tbits/s) range. Such capabilities are not only revolutionizing for mobile communications, but could also benefit satellite communication and intra- and inter-data centers links. However, harnessing the THz spectrum comes with significant challenges. Chief among these are difficult propagation conditions in the atmosphere, e.g. attenuation due to water vapor absorption, and the technological challenges of generating and detecting THz signals have proven difficult with traditional electronic approaches, as they lie beyond the reach of conventional oscillators.

To overcome these challenges and exploit the potential of THz commu-

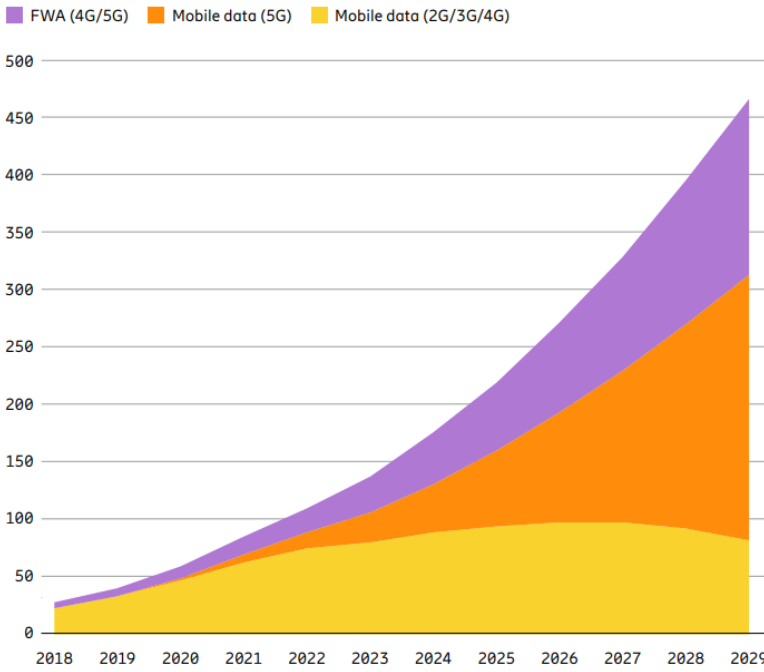


Figure 1.3: Global mobile network data traffic (EB per month). Reproduced from [12].

nications, researchers have turned to THz photonics [14]. Of particular importance is the technique of photomixing to generate THz signals: it leverages the field of photonics by beating two lasers with slightly different frequencies. When these two optical signals are combined on a photoconductive antenna or a photodetector, they produce a beat signal at the difference frequency, which falls within the THz range. The great advantage of this approach is that integrated photonic technologies (See section 1.1) can be used to modulate data and photonic waveguides can be used to distribute data in a system (e.g. in an antenna array). Compared to photonic waveguides, THz waveguides are often bulkier and have higher propagation losses [15]. THz photonics thus bridges the gap between the optical and electronic domain, allowing for the generation of high-frequency signals with the precision and flexibility of photonic systems.

### 1.2.1 On-chip Terahertz transmit array

The future of THz communications holds the promise of compact, efficient, and directive transmitters. Scalable high-gain antenna arrays will be possible thanks to continued technological integration and miniaturization efforts.

We can envision a next-generation THz transmit system that capitalizes on the strengths of integrated photonics [16]. Such a system is illustrated in Figure 1.4. At its core would be a SiN PIC, serving as the foundation for signal generation, manipulation, and distribution. This future PIC could incorporate two tunable lasers to generate the optical signals necessary for THz production, a high-speed modulator to encode data onto these optical carriers, and high-speed photodetectors, acting as the critical interface between the optical and THz domains. By controlling the signals fed to each antenna through the optical distribution network, such a system could achieve beam steering and shaping, enabling dynamic control of the THz radiation pattern. This Silicon-based chip would serve a second purpose as the substrate for the fabrication of highly efficient and wideband on-chip antenna elements, as envisioned in the work of [17].

## 1.3 Contribution & Outline

Although the promise of fully integrated on-chip THz transmit arrays is very exciting, a long road of technological roadblocks still lies ahead, and

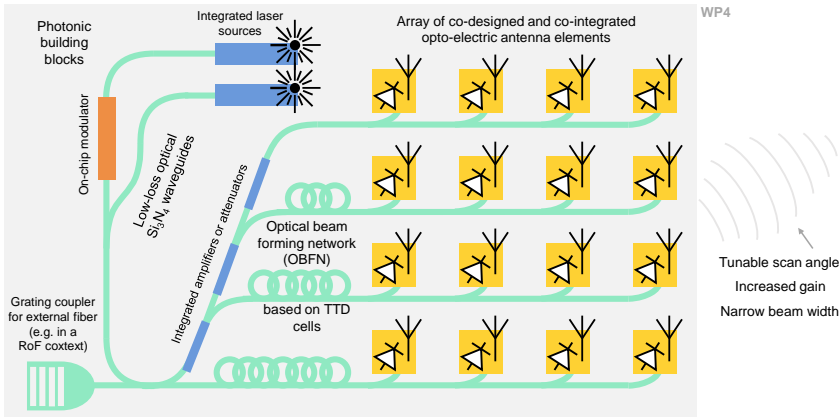


Figure 1.4: The concept of a fully integrated THz transmit array on a PIC: next the optical components – low-loss waveguides, lasers, modulators, high-speed photodetectors – also the antenna elements are integrated in a SiN-based platform.

the complete system remains a future goal. The goal of this PhD thesis is to remove some of these obstacles and develop technologies that bring us closer to their realization. This PhD work focuses on developing novel components for THz generation through photomixing and maturing the Silicon Nitride-based photonic platform that brings this vision of a THz transmit array significantly closer to its realization.

This PhD project is firmly rooted in the domain of electrical and photonic engineering. Being applied scientific disciplines, they fundamentally revolve around the design, creation, and characterization of novel systems. As such, the primary objective is to push the boundaries of technology by developing new devices and technologies, rigorously testing their capabilities, and benchmarking their performance against existing solutions.

The typical research questions that arise from this mindset are typically *How can we design system X to be...faster? more efficient? more compact?*, the former is especially the case for communications systems. Consequently, for any new design, secondary questions arise: *How can this actually be fabricated?* and *How will we measure the performance?* Specifically, in this doctoral project, the research objectives can be summarized by the following overarching questions:

1. How can one make faster transducers for THz photonics?
2. How can these devices be fabricated on SiN photonics?

3. What is the performance of these devices?
4. How do these devices behave in complex communication systems?

As with any research project in engineering, there are no guarantees that the innovations developed during this PhD will find their way into the market or real-life products, as the path from laboratory to commercial application is often complex and unpredictable. Nevertheless, the ultimate goal of engineering research is to create solutions that can positively impact the world, which means that we always consider manufacturability, cost-effectiveness, and compatibility with existing technologies for our design choices and research directions. By keeping these practical aspects in the back of our minds throughout the research process, we strive to develop innovations that are not only technologically advanced but also have the potential to overcome the hurdles of real-world implementation and market adoption.

### 1.3.1 Thesis outline

**Chapter 2** of this thesis presents the successful integration of waveguide-coupled uni-traveling carrier (UTC) photodiodes on a Silicon Nitride (SiN) photonic integrated circuit using micro-transfer printing. With this approach, we could combine the best properties of ultra-fast UTC photodiodes without compromises on a SiN platform. The developed UTC photodiodes demonstrate impressive characteristics, including a record-high bandwidth that represents the fastest photodiode integrated on a SiN platform.

In **Chapter 3** we explore the application of these UTC photodiodes in a high-speed wireless communications link at sub-THz frequencies. The experimental setup achieved data rates of up to 160 Gbit/s while maintaining good signal integrity. This demonstration underscores the potential of heterogeneously integrated photonic devices for next-generation wireless communication systems, addressing the growing demand for increased bandwidth in future networks.

Next, **Chapter 4** focuses on the application of the heterogeneously integrated photodiodes in fixed access interconnects, particularly for data center and short-reach optical communication applications. The chapter demonstrates a short-reach C-band link capable of supporting net data rates exceeding 350 Gbit/s. These results validate the potential of transfer-printed photodiodes on SiN for high-speed baseband optical communications and highlight

their versatility for applications beyond the sub-THz communications domain.

Finally, in **Chapter 5**, we draw the general conclusions resulting from this PhD work, linking the results and conclusions of all chapters to answer the research questions stated above. This chapter also provides an outlook on future research directions, discusses potential improvements in technology, and explores new applications that could further leverage the capabilities of these high-speed photodetectors in integrated photonic systems. We also look forward to some new research questions that came up during this PhD and the new experiments that are needed to answer them.

## 1.3.2 Publications

### Journal publications

1. **D. Maes**, S. Lemey, G. Roelkens, M. Zaknoune, V. Anvramovic, E. Okada, P. Szriftgiser, E. Peytavit, G. Ducourneau and B. Kuyken. "High-speed Uni-Traveling-Carrier Photodiodes on Silicon Nitride." in *APL Photonics*, vol. 8, no. 1, 2023.
2. G. Roelkens, J. Zhang, L. Bogaert, M. Billet, D. Wang, B. Pan, C. J. Kruckel, E. Soltanian, **D. Maes**, T. Vanackere, T. Vandekerckhove, S. Cuyvers, J. De Witte, I. Luntadila Lufungula, X. Guo, H. Li, S. Qin, G. Muliuk, S. Uvin, B. Haq, C. Op de Beeck, J. Goyvaerts, G. Lepage, P. Verheyen, J. Van Campenhout, G. Morthier, B. Kuyken, D. Van Thourhout, and R. Baets. "Micro-Transfer Printing for Heterogeneous Si Photonic Integrated Circuits" in *IEEE Journal of Selected Topics in Quantum Electronics*, vol. 29, no. 3, pp. 1-14, 2023.
3. Günther Roelkens, Jing Zhang, Laurens Bogaert, Emadreza Soltanian, Maximilien Billet, Ali Uzun, Biwei Pan, Yang Liu, Evangelia Delli, Dongbo Wang, Valeria Bonito Oliva, Thi Ngoc Lam Tran, Xin Guo, He Li, Senbiao Qin, Konstantinos Akritidis, Ye Chen, Yu Xue, Margot Niels, **Dennis Maes**, Max Kiewiet, Tom Reep, Tom Vanackere, Tom Vandekerckhove, Isaac Luntadila Lufungula, Jasper De Witte, Luis Dos Reis, Stijn Poelman, Ying Tan, Hong Deng, Wim Bogaerts, Geert Morthier, Dries Van Thourhout, and Bart Kuyken. 2024. "Present and Future of Micro-Transfer Printing for Heterogeneous Photonic Integrated Circuits." in *APL Photonics*, vol. 9, no. 1, 2024.

### Proceedings of international conferences

1. **Dennis Maes**, Gunther Roelkens, Mohammed Zaknounge, Camiel Op de Beeck, Stijn Poelman, Maximilien Billet, Muhammad Muneeb, Sam Lemey, Emilien Peytavit, and Bart Kuyken. "Heterogeneous Integration of Uni-Travelling Carrier Photodiodes using Micro-Transfer-Printing on a Silicon-Nitride Platform." In Conference on Lasers and Electro-Optics Europe and European Quantum Electronics Conference (CLEAO/EUROPE-EQEC), 2021.
2. **D. Maes**, L. Reis, S. Poelman, E. Vissers, V. Avramovic, M. Zaknounge, G. Roelkens, S. Lemey, E. Peytavit, and B. Kuyken, "High-Speed Photodiodes on Silicon Nitride with a Bandwidth beyond 100 GHz," in *Conference on Lasers and Electro-Optics (CLEO)*, 2022.
3. **Dennis Maes**, Sam Lemey, Günther Roelkens, Mohammad Zaknounge, Vanessa Avramovic, Etienne Okada, Pascal Szriftgiser, Emilien Peytavit, Guillaume Ducournau, and Bart Kuyken. "UTC Photodiodes on Silicon Nitride Enabling 100 Gbit/s Terahertz Links at 300 GHz." in *European Conference and Exhibition on Optical Communication (ECOC)*, 2022.
4. **Dennis Maes**, Qian Hu, Robert Borkowski, Yannick Lefevre, Günther Roelkens, Sam Lemey, Emilien Peytavit, and Bart Kuyken. "High-Bandwidth Photodiodes on Silicon Nitride Supporting Net Bitrates in Excess of 350 Gbit/s." in *European Conference and Exhibition on Optical Communication (ECOC)*, 2022.
5. **Dennis Maes**, Günther Roelkens, Sam Lemey, E. Peytavit, and Bart Kuyken. 2022. "Micro-Transfer-Printed Photodiodes on Silicon Nitride for High-Speed Communications." in *Proceedings of IEEE Benelux Photonics Symposium 2022*, 2022.
6. Maximilien Billet, Tom Vanackere, Tom Vandekerckhove, Margot Niels, Luis Reis, **Dennis Maes**, Tom Vanackere, Tom Vandekerckhove, Stijn Poelman, Max Kiewiet, Isaac Luntadila Lufungula, Xin Guo, He Li, Jasper De Witte, Guy Lepage, Peter Verheyen, Joris Van Campenhout, Bart Kuyken, Geert Morthier, Dries Van Thourhout, Roel Baets and Günther Roelkens. "Filling the gap of silicon nitride photonic platform functionalities using micro-transfer printing." in *Integrated Photonics Research, Silicon and Nanophotonics*, 2023.
7. Peter Ossieur, Bart Moeneclaey, Joris Lambrecht, J Craninckx, E Martens, J Van Driessche, J Declerq, Shengpu Niu, Tinus Pannier, Ye Gu, Jing

Zhang, Tom Vanackere, **Dennis Maes**, R.M. Oldenbeuving, X Zhang, Joris Van Campenhout, P Absil, Bart Kuyken, Xin Yin, Guy Torfs, Günther Roelkens, and Johan Bauwelinck. 2023. "High Speed Transceivers beyond 1.6Tb/s for Data Center Networks." in *European Conference on Optical Communications (ECOC)*, 2023.

## Awards

1. Huawei Tech Arena Competition for Silicon Photonics - Silver medal, October 2023  
For the paper: "High-speed Uni-Traveling-Carrier Photodiodes on Silicon Nitride." in *APL Photonics*, vol. 8, no. 1, 2023.



# 2

## Design and fabrication of high-speed photodiodes for SiN

Adapted from and expanded on "Heterogeneous integration of uni-traveling-carrier photodiodes using micro-transfer-printing on a silicon-nitride platform" proceedings of the 2021 Conference on Lasers and Electro-Optics Europe & European Quantum Electronics Conference (CLEO/Europe-EQEC) [18] and "High-speed uni-traveling-carrier photodiodes on silicon nitride" published in 2023 in APL Photonics [19].

---

<b>2.1</b>	<b>Introduction</b>	<b>16</b>
<b>2.2</b>	<b>Uni-traveling carrier photodiodes</b>	<b>17</b>
2.2.1	Working principle	17
2.2.2	UTC epitaxial stack in this work	18
<b>2.3</b>	<b>Transforming diodes into coupons</b>	<b>20</b>
2.3.1	Micro-transfer printing ( $\mu$ TP)	20
2.3.2	Coupon design	21
2.3.3	Coupon fabrication details	23
2.3.4	Considerations for contact metallization	27
2.3.5	Considerations for low dark current	29
2.3.6	Considerations for transfer-printing pickup yield	30
2.3.7	Considerations for high responsivity	32
<b>2.4</b>	<b>Photodiode performance</b>	<b>34</b>

---

2.4.1	Dark current . . . . .	34
2.4.2	Responsivity & Saturation power . . . . .	37
2.4.3	Impedance and equivalent circuit . . . . .	37
2.4.4	Bandwidth . . . . .	40
2.5	<b>Conclusion</b> . . . . .	42
2.6	<b>Ongoing and future Work</b> . . . . .	43

---

## 2.1 Introduction

Integrated photonic solutions are key to solve many challenges for next-generation telecommunication, LIDAR and quantum computing systems. More specifically, Silicon Nitride (SiN) platforms prevail over other materials thanks to the very low-loss waveguides and some of the best integrated filters [20]. Unfortunately, active devices are not natively available. In recent years, the heterogeneous integration of amplifiers and lasers has been demonstrated [21,22]. However, for communication – be it telecom, datacom or microwave photonics – the compact integration of high-speed detectors is even more important.

Widespread adoption of SiN platforms is held back by the absence of such high-bandwidth photodiodes. Table 2.1 shows a comparison of the state-of-the-art waveguide-coupled photodetectors at 1550 nm for different material platforms. Germanium on Silicon [23] (Ge-on-Si) currently offers some of the best waveguide-coupled photodiodes for photonic integration, although this solution is not transferable to low-loss SiN platforms. A Ge-on-Si photodiode coupled to a SiN waveguide is demonstrated at O-band [24], but uses Plasma Enhanced Chemical Vapor Deposition (PECVD) of SiN. For true low-loss waveguides at C-band, Low Pressure Chemical Vapor Deposition (LPCVD) of SiN is required. Monolithic III-V photodiodes [25,26] – often uni-traveling-carrier photodiodes (UTC PDs) – also show very high bandwidths, but these lossy waveguide platforms are not suitable for large-scale photonic integration. On the other hand, current solutions to bring III-V photodiodes to SiN show only limited bandwidths. So far, wafer bonding held the highest record with a bandwidth of 20 GHz [27]. Although wafer bonding can potentially reach identical performance, it lacks the versatility of micro transfer-printing that allows native source-wafer processing, heterogeneous integration of multiple material sources and Back-End-Of-Line (BEOL) integration on non-flat surfaces (e.g. a local recess in the top cladding).

Also on native platforms, i.e. monolithic III-V, progress is being made in

increasing the bandwidth of high-speed photodiodes. As can be seen in Table 2.1, most recent advances are still made without heterogeneous or hybrid integration [28–33].

Table 2.1: State of the art of high-speed waveguide-coupled photodetectors at 1550 nm.

Platform [Ref.]	Year	Responsivity	Bandwidth	Bandwidth at zero bias
III-V, monolithic [25]	2010	0.36 A/W	108 GHz	3 GHz
III-V, monolithic [29]	2014	0.5 A/W	> 110 GHz	-
III-V, monolithic [30]	2018	0.11 A/W	330 GHz	-
III-V, monolithic [31]	2019	0.19 A/W	> 67 GHz	-
III-V, monolithic [26]	2020	0.48 A/W	100 GHz	66 GHz
III-V on SiN, bonded [27]	2020	0.80 A/W	20 GHz	-
Ge-on-Si, monolithic [23]	2021	0.30 A/W	265 GHz	> 67 GHz <sup>1</sup>
<b>III-V on SiN, transfer-printed (This work)</b>	<b>2023</b>	0.30 A/W	155 GHz	135 GHz
III-V, monolithic [32]	2023	0.07 A/W	200 GHz	-
III-V, monolithic [33]	2024	0.16 A/W	>220 GHz	-

## 2.2 Uni-traveling carrier photodiodes

### 2.2.1 Working principle

The Uni-Traveling Carrier (UTC) photodiode represents a significant advancement in photodetector technology, offering superior performance characteristics compared to classical PIN (P-type/Intrinsic/N-type) photodiodes.

The operating principle of a UTC photodiode is based on its unique structure, which consists of a separate absorption layer made out of a p-doped material, and an undoped collection layer. This configuration creates a distinctive carrier transport mechanism. Of the electron-hole pairs generated in the absorption region, the electrons exist as minority carriers in this p-doped material and quickly diffuse into the collection layer due to the built-in electric field. Holes, on the other hand, being majority carriers in the p-doped region, do not significantly participate in the photocurrent.

<sup>1</sup>For photocurrents above 1 mA this drops below 67 GHz.

This unidirectional flow of electrons in UTC photodiodes leads to several advantages over traditional PIN photodiodes. The primary benefit is the achievement of higher speeds. Since only electrons, which have a higher mobility than holes, contribute to the photocurrent, UTC photodiodes can achieve faster response times due to the reduced transit-time ( $\tau_{TT}$ ) limitation.

The electron-only current flow also results in a reduced space-charge effect. This minimization allows for higher output current levels before saturation occurs and contributes to improved linearity in the photodiode's response, particularly at high optical input powers. Consequently, UTC photodiodes can handle higher optical input powers without compromising their high-speed performance, making them suitable for applications requiring both high speed and high power.

These combined advantages make UTC photodiodes particularly well-suited for applications in high-speed optical communication systems, THz generation, and radio-over-fiber (RoF) technologies. In these fields, the superior performance characteristics of UTC photodiodes can be fully utilized, offering significant improvements over classical PIN photodiodes.

## 2.2.2 UTC epitaxial stack in this work

The design of the epitaxial layer stack is based on the work of Latzel et al. [34]. Their work features an optimized epitaxial layer for high-power signal generation at 300 GHz through photomixing at 1550 nm. Albeit their approach relies on vertical illumination through a semi-transparent metal top contact, it is also an excellent stack for evanescent coupling. The UTC epitaxial stack features an undoped collector of 100 nm and a 150 nm-thick absorption region with a graded composition. This results in a graded bandgap that improves the electron transport in the absorption layer by boosting the built-in electric field. This thin absorber region yields a transit-time cut-off frequency ( $f_{TT}$ ) of 424 GHz for an estimated electron drift velocity of  $3.5 \times 10^7$  cm/s.

In this work, Latzel's optimized epitaxial layer stack is extended by including a 500 nm release layer between the InP substrate and the functional layers (See Table 2.2). This sacrificial layer is essential for the creation of suspended coupons needed for the micro-transfer printing process.  $\text{In}_{0.52}\text{Al}_{0.48}\text{As}$  is chosen as the material for this release layer. Compared to InGaAs, InAlAs it is etched isotropically and thus faster. This ensures that the bottom surface of the coupon is flat and the potential *dishing* effect of

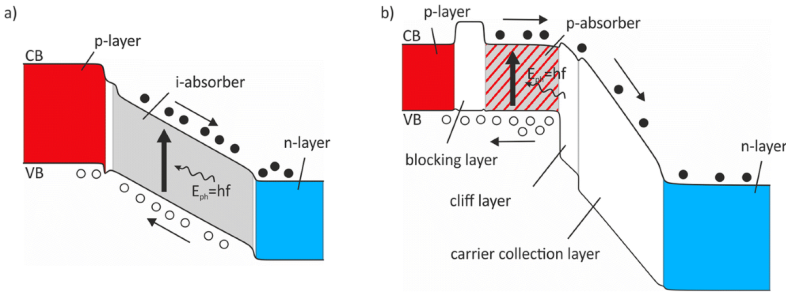


Figure 2.1: Comparison of a PIN photodiode vs UTC photodiode band diagram. Reproduced from [36].

the under etch is limited [35].

Table 2.2: UTC epitaxial layer stack

Feature	Material	T [nm]	Doping [ $\text{cm}^{-3}$ ]
Anode contact	$\text{In}_{0.4}\text{Ga}_{0.6}\text{As}$	10	$p = 1.10^{20}$
Diffusion barrier	$\text{Al}_{0.075}\text{In}_{0.53}\text{Ga}_{0.395}\text{As}$	20	$p = 5.10^{19}$
Absorption region	${}^2\text{In}_{0.47}\text{Ga}_{0.53}\text{As}$ to $\text{In}_{0.4}\text{Ga}_{0.6}\text{As}$	150	$p = 1.10^{18}$
Spacer	$\text{Al}_{0.235}\text{In}_{0.53}\text{Ga}_{0.235}\text{As}$	20	n.i.d.
Cliff layer	InP	7	$n = 1.10^{18}$
Collector region	InP	100	n.i.d.
Sub-collector	InP	50	$n = 3.10^{19}$
Cathode contact	$\text{In}_{0.4}\text{Ga}_{0.6}\text{As}$	10	$n = 3.10^{19}$
Sub-contact	InP	300	$n = 3.10^{19}$
Etch stop	$\text{In}_{0.4}\text{Ga}_{0.6}\text{As}$	20	$n = 3.10^{19}$
<b>Release layer</b>	<b><math>\text{In}_{0.52}\text{Al}_{0.48}\text{As}</math></b>	<b>500</b>	$n = 1.10^{18}$
Buffer	InP	17.5	n.i.d.

<sup>2</sup>Graded composition

## 2.3 Transforming diodes into coupons

### 2.3.1 Micro-transfer printing ( $\mu$ TP)

From the introduction, it became clear that Silicon Nitride (SiN) has emerged as a crucial photonic integration platform, gaining significant traction in recent years due to its excellent optical properties like low propagation losses, wide transparency window, and absence of two-photon absorption (TPA). However, SiN is inherently passive and lacks the ability to generate, modulate, or detect light efficiently. This limitation necessitates the heterogeneous integration of active components, such as high-speed UTC photodiodes, to create fully functional photonic integrated circuits (PICs).

Micro transfer-printing has proven to be an exceptionally effective technology for integrating III-V photonic devices onto SiN chips [1, 2]. This technique allows for the precise placement of pre-fabricated active devices – so-called coupons – onto the target SiN substrate, enabling the creation of hybrid photonic circuits that combine the best properties of both material systems. In the context of UTC PD integration, micro transfer-printing offers several advantages compared to wafer bonding, die-bonding, or other heterogeneous integration techniques:

1. **Versatility:** different types of devices, from different source wafers, made out of different materials, can be integrated on the same SiN chip.
2. **Dense integration:** these different types of devices can be printed closely together on the target PIC.
3. **Selective integration:** only known-good devices are transferred, improving yield and reducing waste.
4. **Scalability:** the transfer of coupons is parallelizable, allowing for the simultaneous transfer of multiple devices.
5. **Efficient wafer usage:** the whole source wafer can be used to create active devices, minimizing the wast of expensive III-V material.
6. **Alignment precision:** sub-micron alignment accuracy ensures optimal coupling between SiN waveguides and III-V devices.

To optimize the performance of integrated UTC PDs while maintaining a compact footprint, the devices are designed with a waveguide shape.

This configuration allows for evanescent coupling of light from the SiN waveguide into the photodiode, which happens naturally thanks to the higher optical index of the III/V coupon ( $n_{III/V} > 3$ ), compared to SiN ( $n_{SiN} \approx 2$ ). By employing this approach, the junction size can be reduced without compromising responsivity, as the light interaction length can be extended along the waveguide axis. This design strategy results in high-performance photodetectors that seamlessly integrate with the SiN photonic circuitry, enabling efficient light detection in a compact form factor.

### 2.3.2 Coupon design

The design of the individual waveguide photodiodes consists of a central mesa, the active layer of the photodiode that contains the absorbing and collecting layer, as well as the anode contact on top. This mesa is flanked by two cathode contacts, separated only 500 nm apart, to allow the wider base of the mesa caused by its slanted sidewalls. Electromagnetic simulations, including 3D finite-difference time-domain (FDTD) simulations, show a waveguide (mesa) width of 2  $\mu\text{m}$  to be ideal in terms of mode coupling efficiency and overall absorption, as well as tolerance for transfer-printing alignment. In Figure 2.2, a cross-sectional simulation of light evanescently coupling from a SiN waveguide to the UTC photodiode shows efficient absorption within the first few micrometers and minimal light loss. From the two separate mode simulations also shown in Figure 2.2, it is clear there is a large mode overlap between both. Photodiodes with three different waveguide lengths (12, 16 and 20  $\mu\text{m}$ ) were designed as a trade-off between absorption length and increased junction capacitance.

Introducing a taper in the non-absorbing, InP sub-contact layer might reduce the reflections at the high index contrast transition. However, eigenmode expansion (EME) propagation simulations showed little to no improvement in the amount of light reflected if a taper were introduced. The simulations showed that by intelligently choosing the waveguide width and coupon separation, reflections are very low. Simulations of the optimized design show reflections below 1 %.

The UTC PD is made entirely on the III-V source wafer (Fig. 2.3a). This process includes two metal depositions for anode and cathode contacts. A self-aligned 2  $\mu\text{m}$ -wide waveguide mesa is etched down to the cathode contact layer, followed by a device etch down to the release layer using a SiN hard mask. (Fig. 2.3b).

To make transfer-printing possible, these diodes need to be converted into

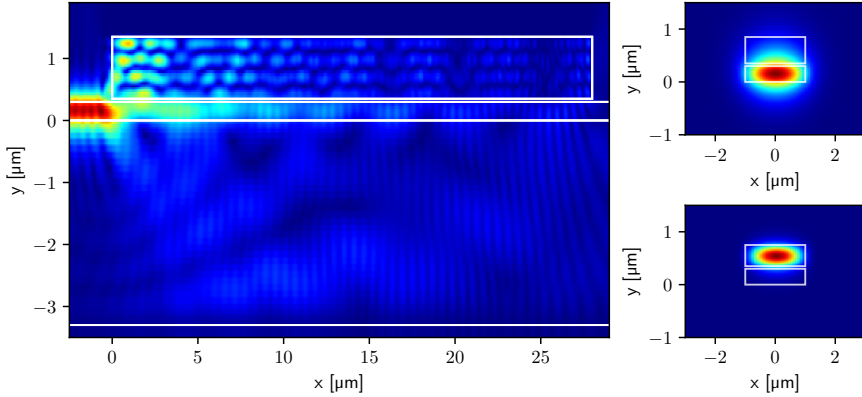


Figure 2.2: **(left)** Cross-sectional simulation of light evanescently coupling from a SiN waveguide to the UTC photodiode, showing efficient absorption within the first few micrometers and minimal light loss. **(top right)** Fundamental mode in the SiN waveguide. **(bottom right)** fundamental mode in the III-V coupon.

diode coupons, i.e. pickable chiplets. To do so, the release layer is first etched anisotropically with a padding of a few micrometers around the diode. A SiN encapsulation layer is deposited and tethers that support the diode are patterned and etched within. The thickness of this layer is 500 nm, which yields a layer strong enough to support the coupon, but still weak enough to break during the pick-up step of transfer-printing. Finally, the remainder of the InAlAs release layer is underetched isotropically using a chilled  $\text{FeCl}_3$  solution, resulting in a suspended coupon (Fig. 2.3c). In Figure 2.6 a SEM image of a released coupon with 4 tethers can be seen.

Next, a photonic integrated circuit (PIC) was designed and fabricated on a SiN platform using in-house ebeam lithography. The material stack of the silicon target wafer consists of 3.3  $\mu\text{m}$ -thick buried oxide (BOX) and 300 nm-thick SiN (Fig. 2.3e). The design features an array of simple printing sites. For easy coupling, each photodiode is fed by a 0.5 mm long waveguide connected to a focused grating coupler. A thin layer of benzocyclobutene (BCB) is spin-coated on the sample that makes adhesion better during transfer-printing and fixes the coupon after curing (Fig. 2.3f).

The coupon is then transfer-printed by picking it up from the source wafer (Fig. 2.3d) and printing it on the target wafer (Fig. 2.3g) using a dedicated flexible stamp, made out of polydimethylsiloxane (PDMS). As a final step after transfer-printing, vias are etched in the SiN-layer and a coplanar waveguide (CPW) of 100  $\mu\text{m}$  is deposited. This allows us to probe the photodiode electrically.

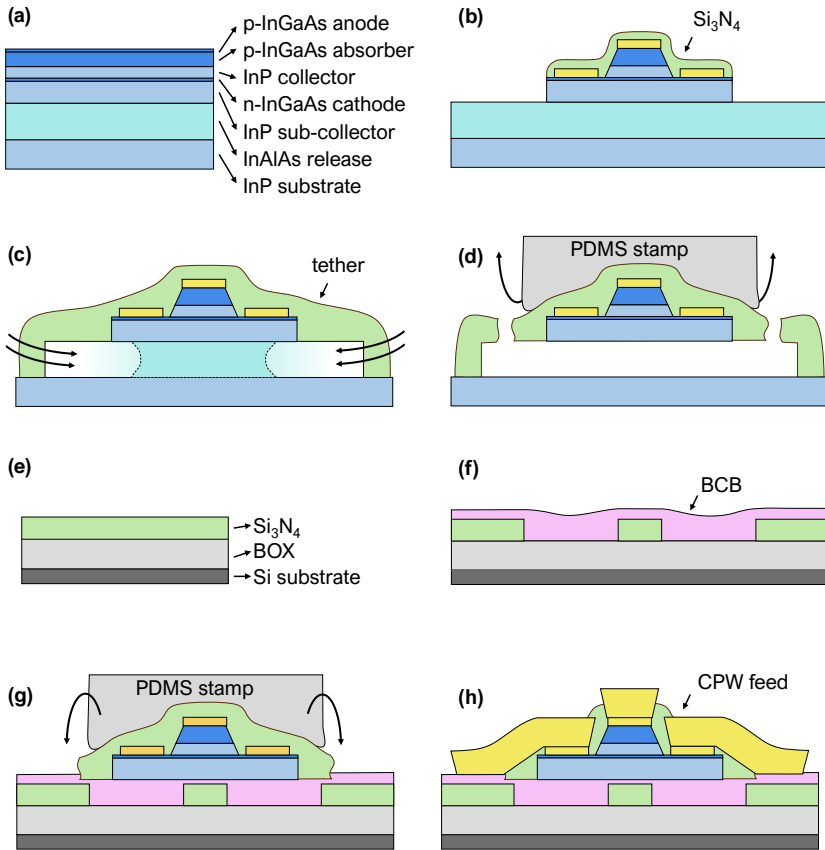


Figure 2.3: Fabrication flow (a) Epitaxial growth of the source III-V wafer (b) Creating a diode by etching the mesa, depositing anode and cathode contacts, and SiN passivation. (c) After tethering the diode to the substrate with a new layer of SiN, the release layer is etched away. (d) This suspended coupon is then picked up by a PDMS stamp of the micro-transfer printer. (e) The silicon target wafer with 300 nm SiN on top of the BOX. (f) Waveguides are created and a thin layer of BCB is spin-coated. (g) The coupon is then printed on top of the waveguide and (h) post-processed to create electrical contacts.

### 2.3.3 Coupon fabrication details

Figure 2.3 shows the overview of how UTC coupons are fabricated in seven big steps. In this section, we will go more into detail on the different fabrication steps that were required to make UTC photodiodes, transform them into suspended coupons, and make the interface with a coplanar waveguide (CPW) for measurements. Below, the different process steps to create a UTC photodiode are listed. More details on the tools and specific

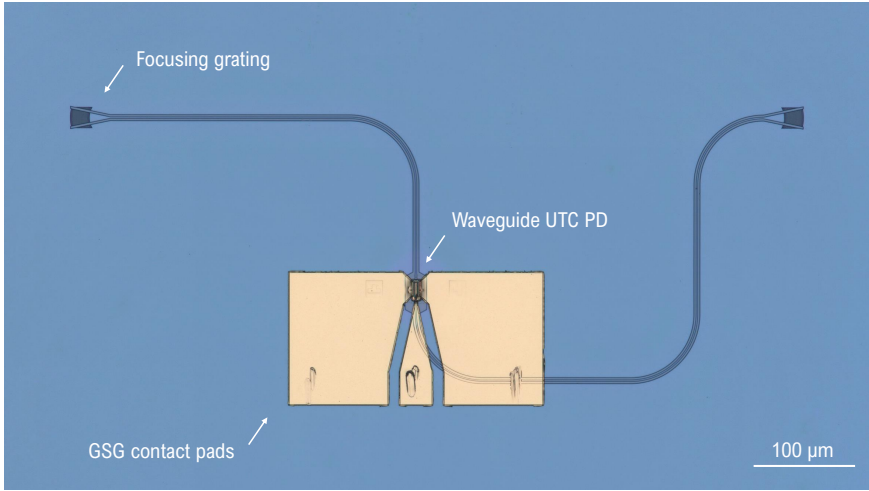


Figure 2.4: Picture of the fabricated PIC: the UTC PD coupon is printed on top of a SiN waveguide for the light to evanescently couple into it. The chip is optically fed using a focusing grating coupler, and electrically probed via GSG contact pads.

recipes used for fabrication can be found in appendix A.

1. First, the anode contact is created using metal lift-off. For this the waveguide shaped anode contact are patterned using e-beam lithography (EBL).
2. Conveniently, the anode metal contact is used as a self-aligned hard-mask to etch the mesa. This is done using a two step procedure consisting of first a ICP dry etch that results in vertical side walls, followed by a wet etch of the remaining InP layer in a  $H_3PO_4:HCl$  solution. The latter has a very high selectivity with respect to InGaAs and will stop as such on the cathode layer.

In figure 2.5 the result of the two-step approach is clearly visible: the mesa sidewall is a combination of a vertical sloped wall that is perfectly aligned with the metal contact – thanks to the anisotropic ICP-etch and high selectivity of the superseding wet etch – and a widening mesa thanks for this we aligned the sample along the  $[01\bar{1}]$  crystal direction.

3. The cathode contact is created again using metal evaporation and lift-off after EBL patterning. A gap of  $1\ \mu m$  is left between mesa and cathode metal. At this point, a functional UTC photodiode is essentially created on the source substrate

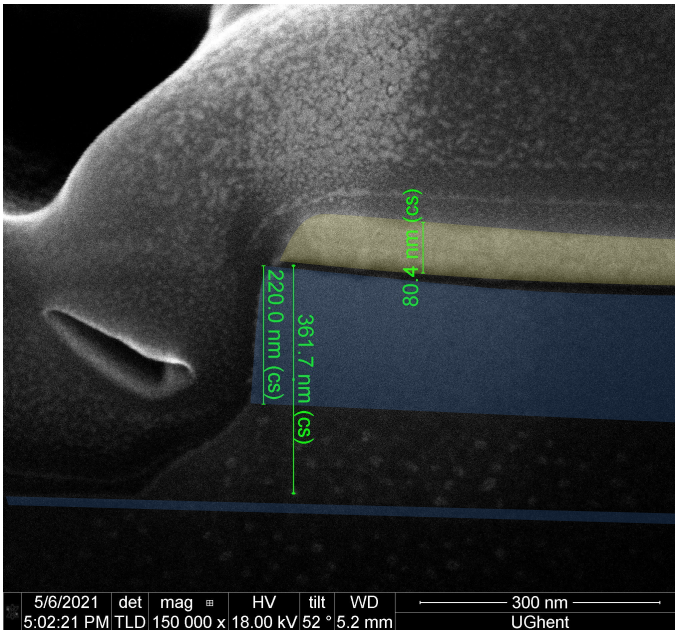


Figure 2.5: SEM image of a FIB cross section of the photodiode mesa. The Au and InGaAs layers are overlaid in yellow and blue respectively.

4. Next, we will define the size of the diode chiplet that will be transferred from its native substrate. A SiN hard-mask is deposited using PECVD and patterned, again with EBL. The hard mask is then etched using RIE followed by a ICP etch of the exposed InP sub-contact layer. To keep the size of the chiplet as small as possible, a margin of only  $0.5 \mu\text{m}$  is taken around the outer edges of the cathode contact.
5. The previous step of depositing a SiN hard-mask is repeated, this time for the *island* etch. This is the area that will be patterned and remain under the chiplet to be etched away during release. Since accuracy is less important in this step – the tether stick out of the chiplet by multiple microns – this layer is patterned using optical lithography.
6. Finally, a third layer of SiN is deposited. This layer will not function as a hard mask, but will be used as tether layer and must be strong enough to support the chiplet once release, yet not too strong so it can still be picked up during transfer-printing. The tethers are patterned using optical lithography and etched using RIE.

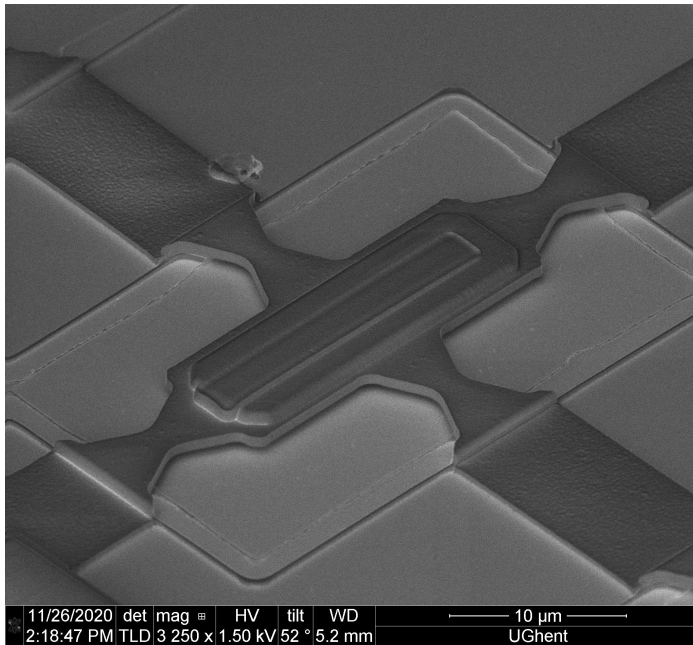


Figure 2.6: SEM image of a released photodiode coupon that is suspended by four SiN tethers. The coupon is floating 500 nm above the substrate.

### 2.3.4 Considerations for contact metallization

An important consideration for the photodiode fabrication is the metal stack. The choice of which metals to use and with which thicknesses not only determines the electrical performance, i.e. a proper Ohmic connection with the semiconductor material, but also has a big influence on the optical absorption and reflection. This effect is even stronger for waveguide-coupled photodiodes than for vertically illuminated photodiodes, as the light might couple into highly absorbing plasmonic optical modes. To achieve a high responsivity, and thus high quantum efficiency, it is of course important that a maximal portion of the light is absorbed by the absorption region of the UTC photodiode. Industry standard metallization stack for Ohmic contacts on InGaAs are combinations of Ti, Ni, Ge, Pd, Pt, Au, and Al [37]. Ti is often added to promote the adhesion with the InGaAs layer. Ni is often chosen because of its low contact resistance with InGaAs, combined with good adhesion. Au and Al mostly serve as top metal layers because they have a high electrical conductivity and have a high resistance to oxidation. Pt, Pd, and Ge are popular choices for intermediate layers that prevent diffusion of the top layer contact into the contact layer or semiconductor stack. [37]

We limited ourselves to combinations of Ti, Pt and Au. This was done out of practical considerations: Ti, Pt and Au are readily available in the cleanroom of Ghent University. A series of FDTD simulations was performed to determine the influence of the metal stack on the light propagation and absorption in a waveguide-shaped photodiode. The epitaxial layer stack discussed in the previous section was used for this. A first set of simulations shows that the influence of the anode metal contact next to the photodiode mesa was negligible compared to the absorption on top of the cathode contact, much closer to the optical mode.

More detailed simulations were then performed to quantify the absorption and light propagation properties with different metal stacks. In each simulation, a waveguide-shaped photodiode with a mesa width of  $2\ \mu\text{m}$  was considered, and a length of  $10\ \mu\text{m}$  was simulated. The results of these simulations are shown in Table 2.3. It is clear that the presence of Ti, and especially Pt, had a big influence on the performance. When using only an Au top layer, 82% of the propagating light is absorbed after  $10\ \mu\text{m}$  with only 6% lost in the Au layer and 76% useful absorption in the InGaAs absorption layer. Whereas a combination of 20 nm Ti, 20 nm Pt, and 20 nm Ti results in 92% absorption with only 38% useful absorption in the InGaAs absorption layer, but 54% lost in the metal layers.

To maximize the amount of useful light absorbed, the first generation of photodiode coupons was fabricated with only-Au contacts. Results of earlier work showed that all-Au contacts were a feasible option for low-resistance Ohmic contacts [34].

The contact metallization not only impacts the photodiode's light absorption, but also its electrical properties. A good Ohmic contact is necessary to create a proper, linear, electrical connection with a low resistance. Different surface treatments were tested before metallization to get the best possible contact: RIE Ar sputtering, a diluted HCl (1:10 DI) dip of 10 seconds and a combination of both. In Figure 2.7 you can see the different test structures on the source chip for the characterization of the contact resistance. Two sets of circular Transfer Length Method (cTLM) test structures are included: all with a 150  $\mu\text{m}$  radius, and a varying gap size, i.e. the transfer length, of 1, 2, 5, 10, 15, 25 and 30  $\mu\text{m}$ .

Based on the measured resistance for each gap size and the corresponding linear fit, the contact resistance  $P_C$ , transfer length  $L_T$ , sheet resistance  $R_S$ , and specific contact resistance  $\rho_c$  could be determined. The results for the p-type InGaAs contact are summarized in table 2.4. It is clear that the HCl treatment to remove the native oxide improved the (specific) contact resistance almost an order of magnitude. The Ar sputtering is ineffective, or even makes the contact perform slightly worse than the untreated sample. The short period between unloading the chip from the RIE-chamber and loading in the evaporation tool is enough to regrow the native oxide. A metal evaporation tool with built-in Ar sputtering was not available for testing. However, the HCl treatment is very effective and yields low contact resistances on par with literature [34].

Table 2.3: Power absorption in an evanescent-coupled waveguide photodiodes for different metallization stacks. (Simulation results)

Ti [nm]	Pt [nm]	Au [nm]	$P_{\text{abs}}$ III/V	$P_{\text{abs}}$ Metal
0	0	300	76%	6%
10	0	300	66%	19%
20	0	300	55%	34%
10	10	300	51%	39%
0	50	300	40%	50%
20	40	300	38%	54%

Table 2.4: Contact resistance properties for different surface treatments before Ti/Pt/Au metallization (p-type InGaAs)

Treatment	$P_C$ [ $\Omega$ ]	$L_T$ [ $\mu\text{m}$ ]	$R_S$ [ $\Omega/\text{sq}$ ]	$\rho_c$ [ $\Omega\text{cm}^2$ ]
Untreated	25	9.0	1320	$2.0 \cdot 10^{-5}$
Ar sputter	25	9.5	1250	$2.3 \cdot 10^{-5}$
HCl dip	4	3.4	596	$5.0 \cdot 10^{-7}$

### 2.3.5 Considerations for low dark current

As important as a high responsivity is for a high-performance photodiode, other electrostatic metrics like dark current are also important. If the dark current of a photodiode is too high, this will impact the noise levels and sensitivity of the system it is used in. In literature, UTC photodiodes for high-speed applications show very low dark currents in the order of tens of nano-amps or even lower.

The first generation of transfer-printed UTC photodiodes showed high dark currents, in the order of micro-amps with  $10\text{-}20 \mu\text{A}$  and  $20\text{-}50 \mu\text{A}$  at respectively  $-0.5 \text{ V}$  and  $-1.0 \text{ V}$  biasing [18], as can be seen in Figure 2.8. A more detailed analysis of the different physical phenomena contributing to

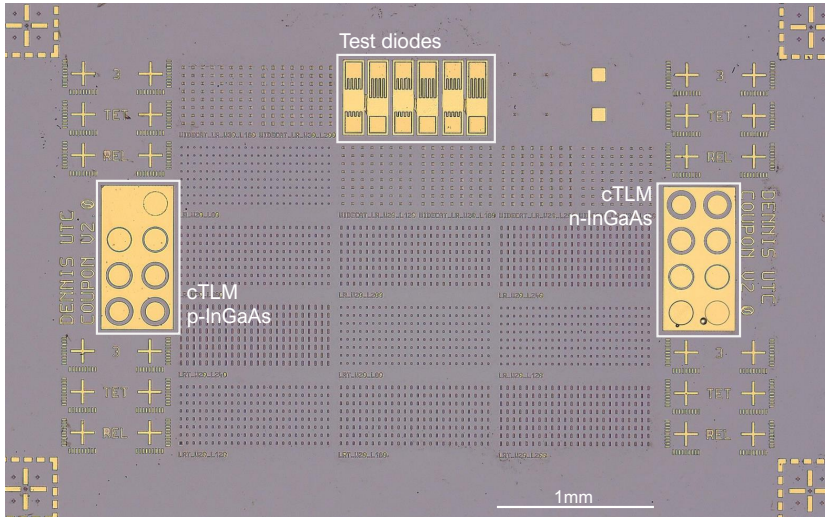


Figure 2.7: The source chip contains different test structures: test diodes with a varying circumference-to-area ratio and cTLM structures for n- and p-InGaAs.

the dark current is given later.

We attribute this to sidewall leakage currents due to dangling bonds. A proper passivation of the mesa in the second generation greatly reduced the dark currents. For this, the mesa sidewalls are passivated with a SiN layer deposited at low temperatures using PECVD. The dark current performance of this second generation coupon with low dark currents is discussed in section 2.4.1.

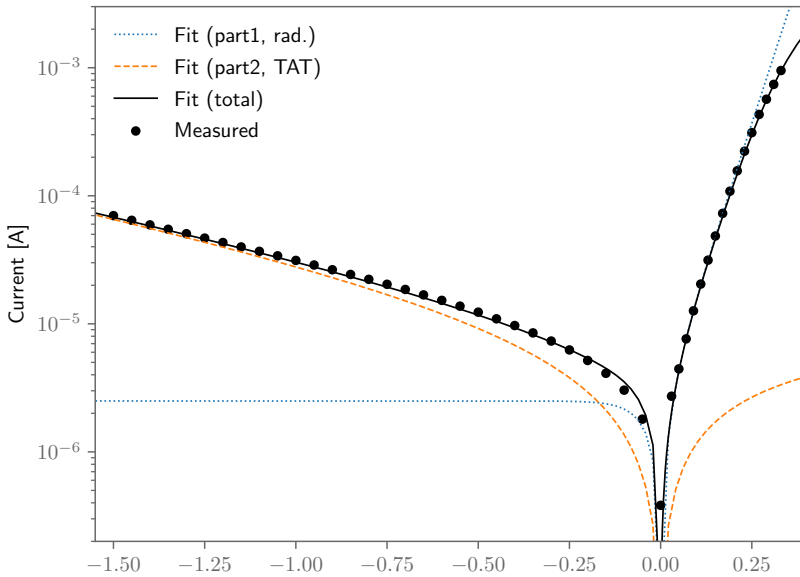


Figure 2.8: The first generation of photodiodes show very high dark currents in the order of 10's of  $\mu\text{A}$ .

### 2.3.6 Considerations for transfer-printing pickup yield

To keep the photodiode's bandwidth as high as possible, its size should be kept to the absolute minimum. Not only should the junction size itself be kept to a minimum, but the overall size of the diode chiplet should be as small as possible. The junction capacitance is the main contribution to the RC-bandwidth limitation, but also the other parts of the chiplet contribute to different parasitic capacitances: stray capacitance between cathode and anode contacts, stray capacitance between the cathode layer and the substrate it will be printed on, etc. As such, not only should the

cathode contact, and equally large underlying mesa waveguide, be small, but also the overall coupon size should be kept to a minimum.

Some of the smallest photonic devices created using micro-transfer printing in the past were also photodiodes, with a mesa size  $25 \times 25 \mu\text{m}^2$  and an overall coupon size of  $75 \times 75 \mu\text{m}^2$  [7,38]. However, in this work the photodiodes are almost two orders of magnitude smaller, with the smallest coupons measuring only  $8 \times 11 \mu\text{m}^2$ . This includes a  $0.5 \mu\text{m}$  margin at all four sides of the SiN tether encapsulation layer. This strong reduction in size brings practical challenges with it: an analysis of the tethers suspending the coupons is required. There are also advantages to the small coupon dimensions: the high-stress materials used for tethering and passivation like SiN have a less pronounced effect on the thin-layer device, i.e. no deformation.

To investigate the ideal tether, a set of dummy coupons was created with variations in the number of tethers, the tether shape, tether width, and tether length. For this study, the tether material and thickness were kept constant: a 600 nm-thick SiN layer was used to ensure proper protection of the coupon during release etch and proper step coverage of the different parts of the coupon. In figure 2.9 four coupons on the source chip can be seen: two of them are tethered with a single hourglass-shaped tether, left and right, and two coupons are tethered with 4 simple tethers, respectively 2 on the left and 2 on the right.

These dummy coupons were transfer-printed on a blank Silicon sample with a 50-nm thin layer of BCB4022 spincoated on top of it. Four important conclusions arose from these tests:

1. Tether width  $W$  is the most determining factor in pick-up success: only tethers of  $1.0 \mu\text{m}$  or  $1.5 \mu\text{m}$  would break. The breaking point for a coupon tethered with  $2.0 \mu\text{m}$ -wide tethers is too strong.
2. Tether length  $L$  played also an important role in pick-up: longer tethers have a lower pick-up yield than short tethers. This can be explained intuitively: if a tether is longer, the same amount of stress will cause strain (flexion) before breaking.
3. The position of a tether is less important than the number of tethers: no difference was noticed between pickup yield for coupons with different tether locations, e.g. 2 left and 2 right vs. 1 at each side.
4. Tether shape had almost no influence: due to limited resolution in patterning the tethers, the *stepped* and *hourglass* shaped tethers have an almost identical shape after etching. A straight tether on the other

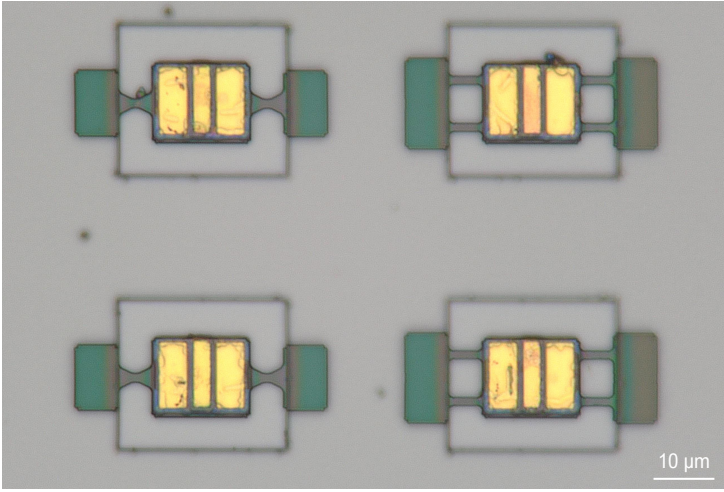


Figure 2.9: Picture of four UTC photodiode coupons on the source chip tethered on their sides with 2 hourglass-shaped tethers (left) and 4 simple tethers (right).

hand has the down side of breaking randomly on the weakest point along it, whereas this will always be the most narrow point for a tapered shape.

To ensure proper waveguide coupling from SiN to the coupons mesa, configurations with a tether on top of the incoming waveguide were avoided in further designs. Since all coupons were properly suspended after release, i.e. no coupons collapsed onto the substrate due to their own weight, a preference was given to the configurations with fewer, smaller tethers.

### 2.3.7 Considerations for high responsivity

In this work, even though responsivity is also very important for the systems used by these photodiodes, the focus is on achieving a high bandwidth, rather than responsivity. Unfortunately, the prerequisite for good contact metallization, discussed in the previous section, put a limit on the total absorbed light, and also the final responsivity.

A 3D-FDTD simulation was performed to investigate the coupling efficiency between SiN waveguide and III-V coupon. For this, the metal layers were no longer taken into consideration. The results show that already more than 80 % of the optical power is absorbed after 12 μm, and 90 % at 16 μm. This can be seen in Figure 2.10, where the fitted curve follows the following

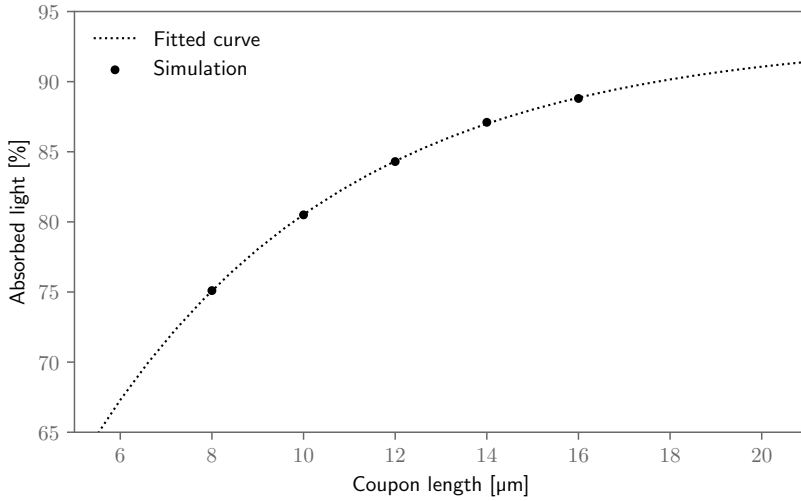


Figure 2.10: Simulated (FDTD) useful light absorption of coupon of  $2\ \mu\text{m}$  wide in function of its length.

relationship:

$$P_{abs} = P_{max} - ke^{-x/L} \quad (2.1)$$

with  $P_{max}$  the maximal power (i.e. light not lost to scattering or reflection),  $k$  a scaling constant, and  $L$  the coupling length.

This first generation of waveguide coupled UTC photodiodes did indeed show high responsivity. Photodiodes with a mesa of  $2 \times 10\ \mu\text{m}^2$  showed a responsivity of  $0.8\ \text{A/W}$ , which corresponds to a quantum efficiency of  $\eta = 65\%$  [18]. This is in line with the simulation results for light absorption in section 2.3.4 comparing different metallization stacks. As well as the simulation results of Figure 2.10. The second generation diodes showed lower values for responsivity [19].

For future generations UTC photodiodes on silicon nitride, a redesign of the epitaxial stack is required to improve the responsivity. By moving the anode contact further from the mode in the III-V, the unwanted absorption can be reduced.

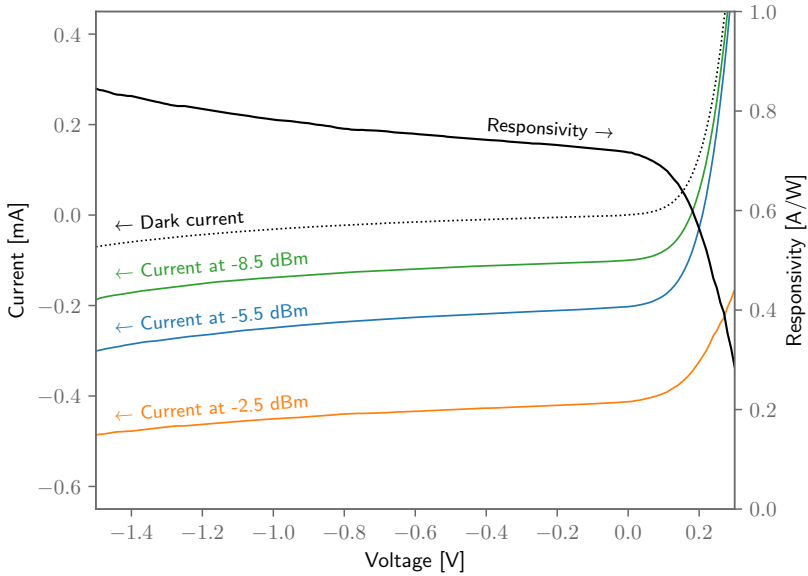


Figure 2.11: A responsivity of  $0.8 \text{ A/W}$  is achieved for a  $2 \times 12 \mu\text{m}^2$  coupon with Au-only metal contacts.

## 2.4 Photodiode performance

### 2.4.1 Dark current

Different physical phenomena give rise to dark current. A simple model of recombination, i.e. independent of the reverse bias voltage, does not fully explain the dark current behavior. Based on the work of Verdun et al. [39], we constructed an empirical model to characterize the dark current and attribute it to three physical contributions:

1. Radiative recombination: dominates the dark current for the highest (positive) dark currents.
2. Trap-assisted tunneling (TAT): this is basically Shockley-Read-Hall recombination (SRH) enhanced by tunneling effects, and dominates the dark current for for moderately low (negative) bias voltages
3. Band-to-band (B2B) tunneling: this contribution is the dominant source of dark current for stronger (negative) bias voltages, and highly governed by defects.

Considering this model, the dark current  $I_{dark}$ , in function of bias voltage  $V$ , consists of three components and is given by

$$I_{dark} = I_S e^{V/V_t - 1} - AV^2 e^{B/V} - I_B e^{-v/V_{t,rev} - 1} \quad (2.2)$$

with  $I_S$  the saturation current,  $V_t$  the threshold voltage,  $A$  and  $B$  two empirical parameters for the trap-assisted tunneling component,  $I_B$  the reverse breakdown current, and  $V_{t,rev}$  the reverse threshold voltage.

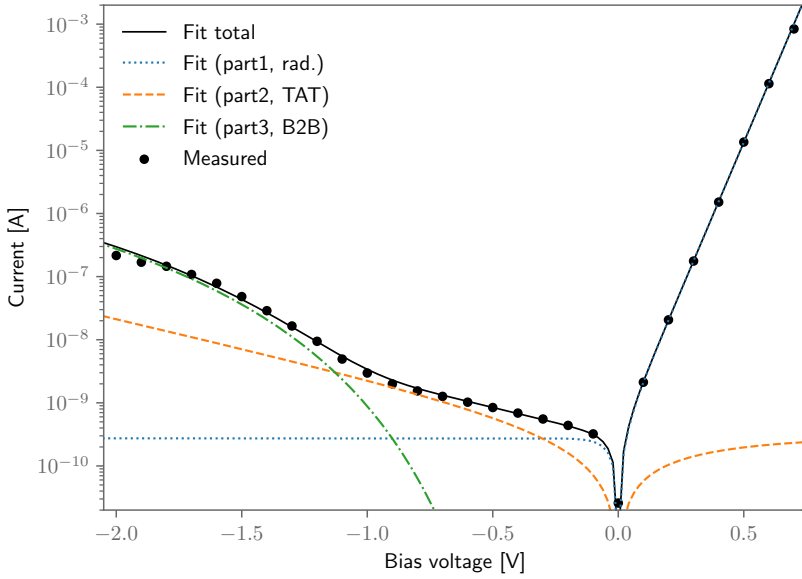
In table 2.5 and figure 2.12 the results of the dark current analysis of two transfer-printed photodiodes are shown. Diode 1 and 2 respectively have a  $2 \times 12$  and  $2 \times 16 \mu\text{m}^2$  mesa. It is clear that the model has a very good fit over the whole bias voltage range, and the three different current contributions each have a clear dominant region. Diode 1 and 2 have almost identical current parameters, except for the TAT contribution of the dark current, which is considerably higher for diode 2. We believe that most defects, and thus possible locations for traps, are sidewall defects. The increased perimeter-to-surface ratio of the  $16 \mu\text{m}$ -long vs. the  $12 \mu\text{m}$ -long is in line with this hypothesis.

Also for the first generation devices, with very high dark current, this model could be applied. As can be seen in Figure 2.8, the dark current is dominated by the trap-assisted tunneling effect: the values for  $I_S$  and  $I_B$  are orders of magnitude larger.

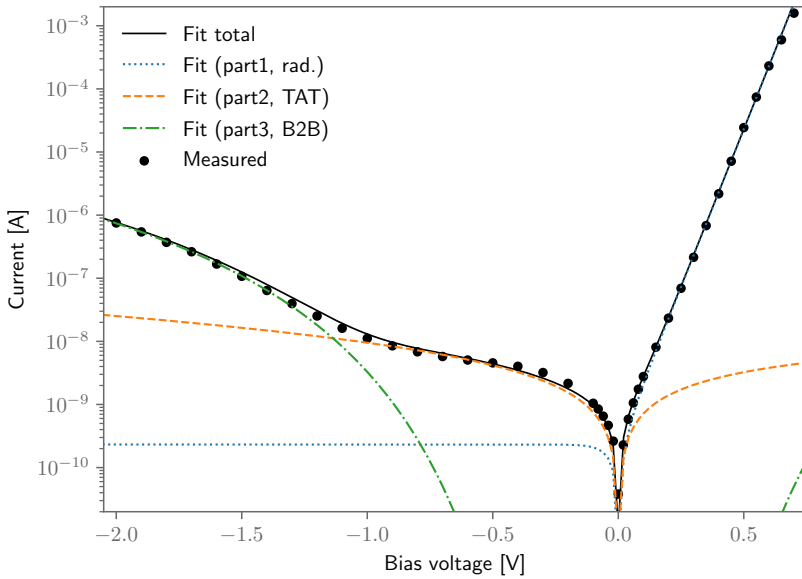
Table 2.5: Dark current parameters

Mesa [ $\text{m}^2$ ]	$I_S$	$V_t$	A	B	$I_B$ [nA]	$V_{t,rev}$
$2 \times 12 \mu\text{m}^2$	0.27 nA	0.046 V	$0.3 \mu\text{A}/\text{V}^2$	0.5 V	5.4 nA	8.7 V
$2 \times 16 \mu\text{m}^2$	0.23 nA	0.043 V	$14.9 \mu\text{A}/\text{V}^2$	2.0 V	9.9 nA	8.0 V
$2 \times 10 \mu\text{m}^2$ (Gen 1 PD)	$2.5 \mu\text{A}$	0.050 V	-	-	$9 \mu\text{A}$	0.71 V

The measured values for currents above 0.5 mA show a slight deviation from the expected exponential behavior, as can be seen in figure 2.12. This can be explained by the voltage drop over the series resistance. A first guess of the series resistance can be made using these data points, and corresponds with a value around  $10 \Omega$  for both diode 1 and 2. A more detailed analysis of the diode impedance is given in section 2.4.3. This effect is even more pronounced in the first generation of PDs, where a series resistance of  $40 \Omega$  is measured (See Figure 2.8).



(a) Diode 1 with a mesa size of  $2 \times 12 \mu\text{m}^2$



(b) Diode 2 with a mesa size of  $2 \times 16 \mu\text{m}^2$

Figure 2.12: Dark current analysis for two different photodiodes: a empirical model breaks down the dark current into three contributions: radiative recombination, trap-assisted tunneling (TAT) and band-to-band (B2B) tunneling currents.

## 2.4.2 Responsivity & Saturation power

The responsivity of the photodiodes at a wavelength of 1550 nm is measured to be 0.3 A/W. This responsivity was verified to be constant for bias voltages ranging between  $-2.5$  V and 0 V, as well as at low and high power levels, up to multiple milliwatts of on-chip power.

The formula for the photocurrent is given by

$$I_{phot} = \eta \frac{q}{h\nu} = \eta \frac{q\lambda}{hc} \quad (2.3)$$

with  $\eta$  the (quantum) efficiency,  $h$  Planck's constant,  $\nu$  the frequency of the light and  $q$  the elementary charge of an electron,  $\lambda$  the wavelength of the light and  $c$  the speed of light. Given the above responsivity, this results in a (waveguide-referenced) external quantum efficiency (EQE) of 23 %.

Although photodiodes with different waveguide lengths – 12, 16 and 20  $\mu\text{m}$  long – were made, no significant correlation with increased responsivity is found. It is believed that the excess light is absorbed in areas not contributing to the photocurrent, such as the metal contacts. Hence, increasing the length of the waveguide-coupled UTC PD is not beneficial.

The 1 dB-saturation point is reached at 4.5 mA photocurrent for  $-1$  V bias with an RF power output of  $-4.1$  dBm at 100 GHz as shown in Fig. 2.13. This is also very close to the thermal breakdown current. For zero bias, saturation is reached at 2.8 mA with an output power of  $-9.7$  dBm at 100 GHz. The effective resistance  $r_{eff}$ , given by  $P_{RF} / I_{phot}^2$ , serves as a good measure for the photocurrent to RF conversion efficiency, independent of the optical power [34]. These diodes show a high efficiency with  $r_{eff}$  going up to 20  $\Omega$ .

The device used for this experiment has a mesa size of  $2 \times 16 \mu\text{m}^2$  and a 3 dB-bandwidth around 115 GHz at  $-1$  V. The bandwidth at 0 V was not explicitly measured, but is assumed to be around 105 GHz, in line with the other results from section 2.4.4. As such, at 100 GHz, the device operates in the soft roll-off region above the 3 dB threshold. This explains the offset in RF power between the measurements at 0 V and  $-1$  V of 1.5 dB.

## 2.4.3 Impedance and equivalent circuit

The theoretical RC-bandwidth limitation in section 2.4.4 can be calculated based on the series resistance  $R_S$  and junction capacitance  $C_j$  of the UTC PD. For this, the equivalent circuit of the devices is needed. Data was acquired

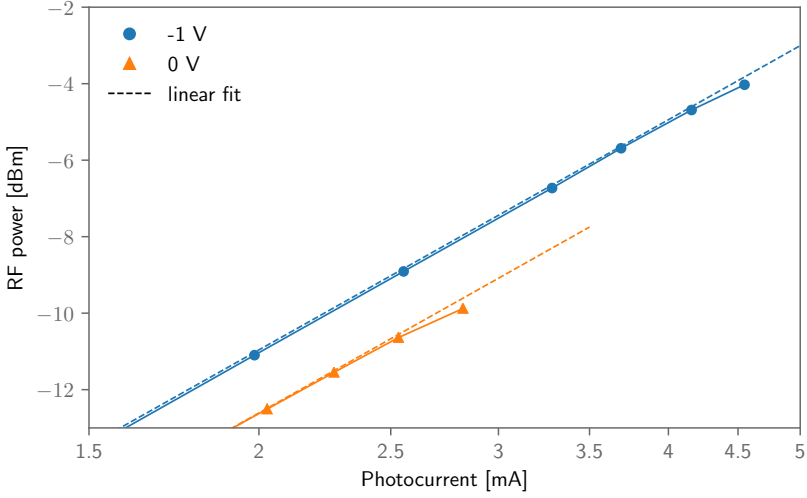


Figure 2.13: RF power at 100 GHz. The 1 dB-saturation current for a PD with a  $2 \times 16 \mu\text{m}^2$  active area is more than 4.6 mA at  $-1$  V bias and more than 2.8 mA at zero bias.

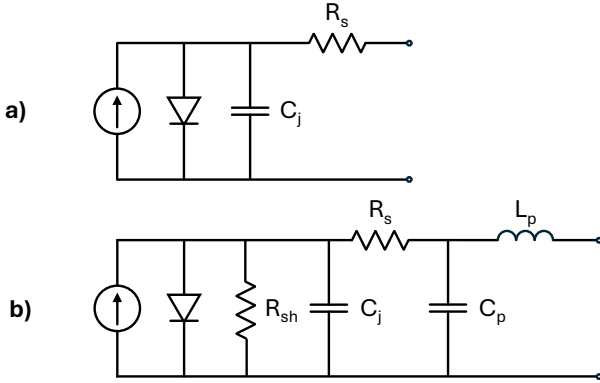


Figure 2.14: Equivalent circuits: **a)** simplified equivalent circuit (applicable after Open-Short de-embedding) and **b)** equivalent circuit including parasitics.

Table 2.6: Fitted values for the resistance  $R_S$ , capacitance  $C_j$ , and shunt resistance  $R_{sh}$  of three different coupons after Open-Short de-embedding.

Mesa size	$C_j$	$R_S$	$R_{sh}$
$2 \times 12 \mu\text{m}^2$	18.5 fF	4 $\Omega$	64 k $\Omega$
$2 \times 16 \mu\text{m}^2$	25 fF	4 $\Omega$	87 k $\Omega$
$2 \times 20 \mu\text{m}^2$	31 fF	7 $\Omega$	25 k $\Omega$

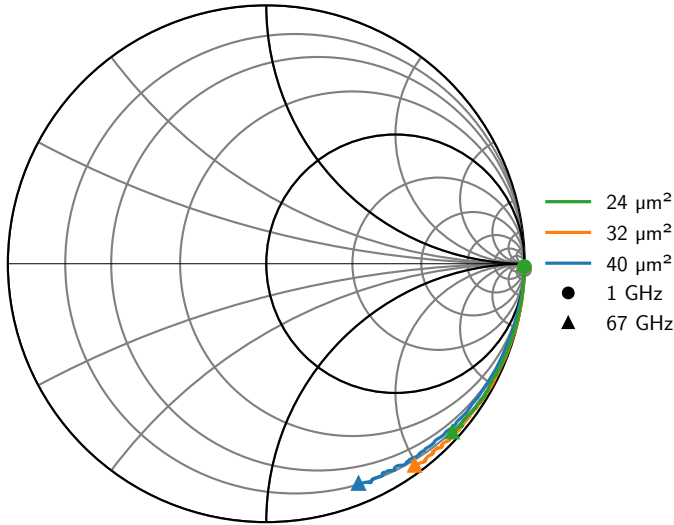


Figure 2.15: The reflection coefficients of three different sizes of waveguide-photodiodes after OpenShort de-embedding. A simple RC-behavior, with increasing capacitance for larger junction areas, is clearly visible.

by measuring the impedance of the transfer-printed photodiodes with a Vector Network Analyzer (VNA) up to 67 GHz: Keysight PNA-X N5247B. The system was first fully calibrated up to the GSG-probe tips: for this, a CS-5 Open-Short-Load (OSL) calibration substrate of Picoprobe is used.

Figure 2.14 shows the two models used for equivalent circuit matching: a simplified version with only the series resistance  $R_S$  and the junction capacitance  $C_j$  of the diode coupon (Figure 2.14a), and a second model that also includes the large parasitic shunt resistance  $R_{sh}$ , as well as the parasitic inductance  $L_p$  and capacitance  $C_p$  of the short interconnects (Figure 2.14b) [40]. To use the former model, the measurement results are first de-embedded with two extra single-ended measurements: an open circuit (no coupon printed) and a short (metal between anode and cathode contacts). This Open-Short de-embed is done using the open source Python package scikit-rf [41]. The S-parameters of the de-embedded measurements are shown in the Smith chart in Figure 2.15.

After de-embedding a very good fit ( $R^2 > 0.99$ ) with the simplified RC model (a) could be made: the extracted junction capacitance  $C_j$  is 18.5, 25, and 31 fF for PDs with a length of 12, 16 and 20  $\mu\text{m}$  respectively. The

series resistance of all coupons is very low, varying between 4 and 10  $\Omega$ , and depends on the success of the metallization of the tiny via connections. The extracted values for three coupons of different sizes are summarized in Table 2.6. When we standardize the capacitance values per unit area, we obtain 0.8 fF/ $\mu\text{m}^2$ , which is marginally less than the anticipated 1 fF/ $\mu\text{m}^2$  for an InP collector with a thickness of 100 nm. At zero bias, the junction capacitance increases by approximately 10%.

Because each coupon shares the same design for the shape of metallization during post-processing, the parasitic parameters show little variability in the fitted results. It is safe to say that all the short metal traces are represented by an inductance  $L_p$  of 59 pH and capacitance  $C_p$  of 27 fF, in correspondence to model b in Figure 2.14.

#### 2.4.4 Bandwidth

The bandwidth of the photodiode was measured using different setups for different frequency ranges, consisting of a combination of RF probes and power meters.

1. DC to 110 GHz: a coaxial probe, bias-tee, and Rohde and Schwarz thermal power meter (R&S NRP-Z58 [42]).
2. 140 GHz to 220 GHz: a WR5-probe with built-in bias tee, in combination with a calorimeter-style power meter (Erickson PM5 [43])
3. 220 GHz to 325 GHz: a WR3-probe with built-in bias tee, in combination with a calorimeter-style power meter (Erickson PM5)

The RF excitation signal was generated using two distributed-feedback (DFB) lasers, locked together with a digital control loop. The measurement results were corrected for probe, bias-tee and THz-waveguide losses, as provided in the datasheets of the suppliers. In figure 2.16 the frequency response of a  $2 \times 12 \mu\text{m}^2$  PD is shown: a record-high 3-dB bandwidth of 155 GHz at  $-1$  V bias, which is faster than any state-of-the-art photodiode heterogeneously integrated on SiN [27, 34]. At zero bias, a bandwidth of 135 GHz is obtained, which is even higher than the best Silicon-on-Insulator (SOI) counterparts [23]. It should be noted that the 135 GHz-bandwidth is based on interpolated data. As there was no probe available for the frequency range between 110 GHz and 140 GHz. This can be seen in the normalized frequency response (Fig. 2.16).

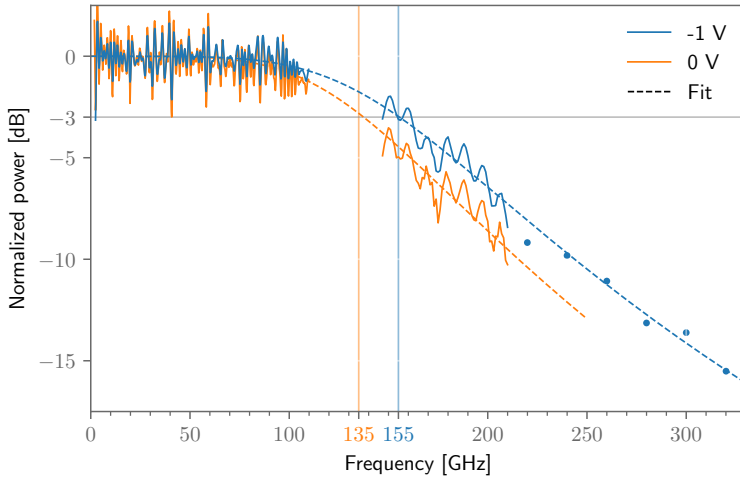


Figure 2.16: The 3-dB bandwidth for a PD with a  $2 \times 12 \mu\text{m}^2$  active area is 155 GHz at  $-1$  V bias and 135 GHz at zero bias, both with a photocurrent of 1 mA.

Due to the thin layer thickness and high electron mobility in the absorption region, the bandwidth is mostly limited by the RC time constant ( $f_{RC}$ ) [44]. If we take into account the extracted junction capacitance  $C_j$  of 18.5 fF, the series resistance  $R_s$  of  $4 \Omega$ , as well as the  $50 \Omega$  impedance of the measurement equipment, the calculated  $f_{RC}$  equals 159 GHz. (See formula 2.4) The transit-time cut-off frequency ( $f_{TT}$ ) is calculated to be 424 GHz for an estimated electron drift velocity of  $3.5 \times 10^7$  cm/s in the 150-nm thick absorber. Combining both bandwidth limitation using formulae 2.5, this results in an overall 3-dB bandwidth of 146 GHz, which is very close to the measured result. The small difference is attributed to the uncertainty on the effective electron velocity in the absorber and possible inductive effects of the CPW contacts. At zero bias, the calculated RC-limit is 145 GHz, implying a small additional decrease in the transit-time bandwidth as well.

$$f_{3dB,RC} = \frac{1}{2\pi(R_{VNA} + R_S)C} \quad (2.4)$$

$$f_{3dB} = \frac{1}{\sqrt{f_{3dB,TT}^2 + f_{3dB,RC}^2}} \quad (2.5)$$

## 2.5 Conclusion

This research demonstrates the successful integration of waveguide-coupled uni-traveling carrier (UTC) photodiodes on a silicon nitride (SiN) photonic integrated circuit (PIC) platform through micro-transfer printing. This novel approach offers significant advantages by allowing separate fabrication of the III-V chiplet and SiN PIC, ensuring efficient material usage, and delivering high-performance waveguide-coupled photodetectors. The ability to fabricate the III-V chiplet and SiN PIC independently allows for optimization of each component without compromising the other. Furthermore, micro-transfer printing ensures efficient use of III-V materials, which are typically more expensive and scarce compared to silicon-based materials. These advantages combine to push the boundaries of current technology in optoelectronic integration.

The UTC PDs developed in this work demonstrate characteristics that underscore their high performance. With a responsivity of 0.3 A/W, these devices show high efficiency in converting optical signals to electrical current, with the potential for further improvement. The low dark current, below 10 nA at reverse bias voltages greater than  $-1$  V, suggests minimal noise contributions which helps to improve the overall sensitivity of the device. But the most impressive feature of these photodiodes is their high bandwidth. At  $-1$  V bias, they achieve a bandwidth of 155 GHz, while even at zero bias, they maintain a remarkable 135 GHz. These values represent a significant advancement in high-speed photodetectors, especially for SiN-based photonic platforms. Additionally, the high saturation current of multiple mA's allows for operation at high optical power levels without performance degradation, further enhancing their versatility.

To the best of our knowledge, this work presents two significant achievements in the field. Firstly, it introduces the fastest photodiode integrated on a SiN platform, with 155 GHz about eight times higher than the current state-of-the-art photodiodes heterogeneously integrated on SiN [26]. Secondly, it showcases the fastest zero-bias photodiode across all platforms, even better than the best Silicon-on-Insulator (SOI) counterparts [23].

## 2.6 Ongoing and future Work

Building upon the successful integration of waveguide-coupled UTC photodiodes on the SiN platform, our ongoing research has already made significant strides towards enhancing the fabrication process and device performance. While these advancements are yet to be published, they represent promising directions for future development and optimization of the technology, albeit with some challenges to address.

A key focus of our recent efforts has been the refinement of the fabrication process. We have proposed and implemented improvements that aim to streamline the manufacturing workflow and enhance the device's structural integrity and performance. One notable change is the relocation of the contact via etching step from the target substrate to the source wafer. This modification serves a dual purpose: it allows for more precise alignment of vias themselves and it reduces the number of post-processing steps required after transfer printing. Specifically, this modification enables the use of lower-resolution optical lithography techniques instead of the previously required electron-beam lithography for the via definition. This shift not only simplifies the fabrication process but also has the potential to reduce production costs and increase throughput in future large-scale manufacturing scenarios.

However, it's important to note that this process modification also introduces new challenges that require careful consideration. Moving the via etch to the source wafer poses potential risks during two critical stages of the fabrication process. Firstly, during the release step, the diode contacts are no longer hermetically sealed from the etchant. This exposure could potentially lead to undesired etching or degradation of the contact materials. And secondly, during the transfer printing process itself, this change allows the stamp to make direct contact with the metal in the vias. This direct interaction between the stamp and the metal contacts could potentially impact the transfer yield or the integrity of the contacts.

In tandem with this process improvement, we have introduced an extra metallization step to the device structure. This additional layer primarily addresses a previous limitation in the width of the anode contact via. At the end of the waveguide device, this third metal layer tapers open to increase the width of the exposed anode contact, and as such simplifies the alignment and reduces the required resolution for the post-transfer-printing metallization step.

The adjusted process can be seen in Figure 2.17, for each panel the top view

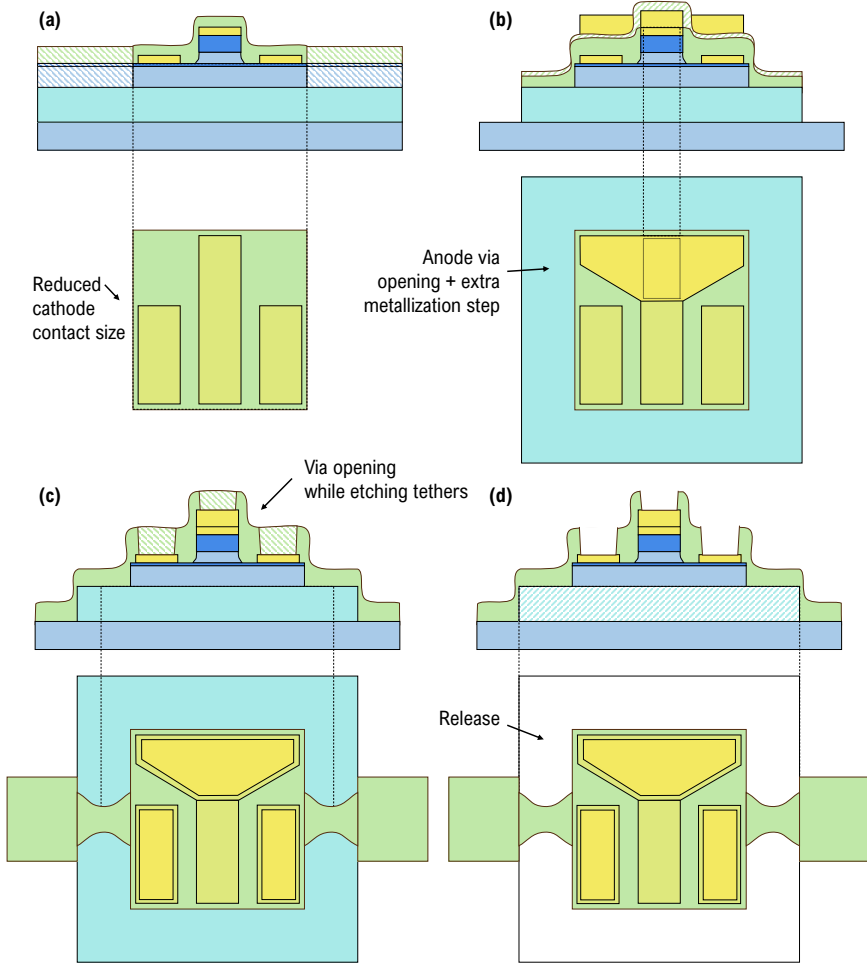


Figure 2.17: Added steps in the new generation of UTC PD coupons. (a) cathode contacts are reduced in size (b) a via is etched on top of the anode contact and a third metal layer is deposited to increase the width of this contact. (c) vias in the SiN encapsulation are etched together with the tethers. (d) the coupon is released.

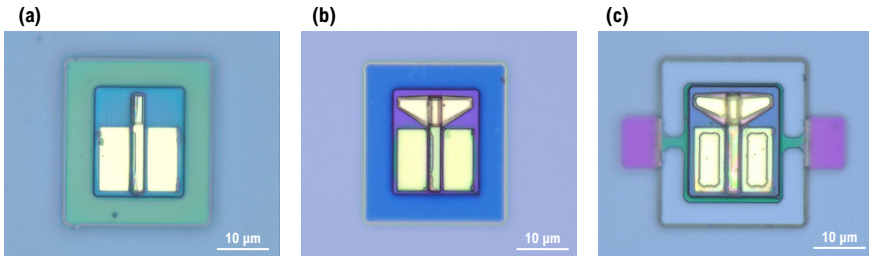


Figure 2.18: Pictures of a coupon with a  $2 \times 20 \mu\text{m}$  mesa. (a) a  $2 \times 6 \mu\text{m}$  via is etched on top of the cathode. (b) a tapered metal contact is deposited to increase the size of the cathode contact. (c) the final vias are etched in the SiN encapsulation, together with the tether etch.

and cross-sectional view are provided. The shape of the cathode metal contacts is reduced to allow a third metal deposition that extends the width of the first anode metal layer at one side of the coupons.

Preliminary measurements of devices fabricated using this improved process have yielded encouraging results. We have observed a responsivity of  $0.3 \text{ A/W}$ , which is consistent with our previous findings and indicates that the new fabrication process maintains the high performance standards established in our earlier work. Moreover, we have seen a marked improvement in the dark current characteristics, with values now falling below  $1 \text{ nA}$  at  $-1 \text{ V}$  bias. This reduction in dark current potentially allows for lower noise operation, which could be particularly beneficial for applications requiring high signal-to-noise ratios.

While these initial results are promising, we recognize that further improvements in responsivity are desired and will likely require modifications to the epitaxial stack design to move the absorbing metal a greater distance from the optical mode inside the waveguide device. In conclusion, our ongoing work demonstrates a clear path forward for enhancing the fabrication and performance of waveguide-coupled UTC photodiodes on SiN platforms, while also highlighting the complexities and trade-offs involved in process refinement. The proposed improvements in the fabrication process, coupled with the encouraging preliminary results, set the stage for the next generation of high-performance, highly integrated optoelectronic devices.



# 3

## High-speed link at 300 GHz enabled by UTC photodiodes on SiN

Adapted from and expanded on "UTC Photodiodes on Silicon Nitride Enabling 100 Gbit/s Terahertz Links at 300 GHz" and proceedings of the 2022 European Conference on Optical Communication (ECOC) and "High-speed uni-traveling-carrier photodiodes on silicon nitride" published in 2023 in APL Photonics.

---

<b>3.1</b>	<b>Introduction</b>	<b>48</b>
<b>3.2</b>	<b>Experimental setup for a 300 GHz link</b>	<b>49</b>
<b>3.3</b>	<b>System performance</b>	<b>51</b>
3.3.1	Error Vector Magintude (EVM)	51
3.3.2	Results	53
<b>3.4</b>	<b>Conclusion</b>	<b>58</b>
<b>3.5</b>	<b>Ongoing and Future work</b>	<b>59</b>

---

## 3.1 Introduction

Next-generation wireless networks will rely on smaller cells and larger bandwidths to accommodate the ever-increasing demand for capacity. As current microwave frequencies become congested, there is a push towards higher frequency bands, particularly in the terahertz (THz) range. These higher frequencies offer vast amounts of available spectrum, potentially enabling unprecedented data rates and network capacity. Radio-over-fiber (RoF) technology allows the implementation of such dense base station networks by keeping the radio head hardware simple, while the miniaturization of the base station hardware, leveraging silicon photonics technologies, keeps the size and cost down.

The THz frequency range, typically defined as electromagnetic waves with a frequency between 100 GHz and 10 THz, bridges the gap between microwaves and infrared light. The lower end of this THz range, the so-called sub-THz range (100 GHz and 1 THz), overlaps with the higher range of the mmWave range (30-300 GHz, which is already in use for 5G and 6G networks). This frequency range offers unique advantages for wireless communications, including broader bandwidths with the potential for ultra-high-speed data transmission. However, harnessing these frequencies for practical applications presents significant technical challenges.

Silicon Nitride (SiN) has emerged as a highly popular photonic platform. Its popularity stems from its exceptional optical properties, including very low-loss waveguides and some of the best integrated filters available. These characteristics make SiN an ideal candidate for high-performance microwave photonic systems. However, to fully exploit the potential of SiN in high-frequency applications, ultra-high-speed transducers are required to efficiently convert signals from the optical to the electrical domain. In the previous chapter, we addressed this challenge by demonstrating the successful integration of ultra-fast photodiodes on a SiN platform, effectively bridging the gap between SiN's excellent optical properties and the high-speed requirements of terahertz applications.

This chapter focuses on an experimental demonstration that leverages our novel photodiode on SiN to operate at sub-THz frequencies around 300 GHz. We present a comprehensive study of a communication link enabled by a heterogeneously integrated uni-traveling-carrier (UTC) photodiode on SiN, like the ones created and characterized in chapter 2, serving as the optoelectronic transducer in the transmitter. The experiment showcases how our SiN photonic integrated circuit (PIC) with heterogeneously integrated

photodiodes generates a THz signal through photomixing. We describe a system setup that demonstrates sufficient power generation at sub-THz frequencies with good noise performance, achieving data speeds exceeding 100 Gbit/s. This achievement represents a crucial step towards realizing the potential of THz communications in next-generation wireless networks, bridging the gap between SiN's excellent optical properties and the high-frequency requirements of future communication systems.

## 3.2 Experimental setup for a 300 GHz link

The experimental setup extends beyond the device under test (DUT), which consists of a SiN PIC with an integrated photodiode. Additional equipment completes the system, as illustrated in Figure 3.1 and 3.2.

The transmitter side comprises two C-band DFB lasers, locked to each other via a digital control loop. The wavelength offset between these lasers determines the carrier frequency of the THz signal. One of the laser lines is modulated using a Mach-Zehnder modulator (MZM), which is directly driven by an arbitrary waveform generator (AWG). After combining the two laser lines, they are amplified using an erbium-doped fiber amplifier (EDFA) before being coupled into the SiN photonic integrated circuit (PIC). Vertical grating couplers are used to couple the light into the PIC, introducing a 9 dB insertion loss.

Depending on the experiment (see below) two different EDFA's were used:

- ThorLabs EDFA100P: 20 dBm  $P_{sat}$
- Manlight C-band, higher  $P_{sat}$  of 27 dBm, but also a higher noise figure.

The mixed terahertz signal is then coupled out of the PIC using a 50  $\mu\text{m}$ -pitched GSG-probe and fed into a WR-3 waveguide channel. It's important to note that our goal was specifically to demonstrate the potential of the PIC at 300 GHz. Therefore, we did not couple the signal into free space or use any additional Monolithic Microwave Integrated Circuit (MMIC) power amplifiers. This setup creates a purely back-to-back (B2B) link with limited losses in the WR-3 waveguide channel.

At the receiver side, a Schottky-based diode mixer down-converts the THz signal. The signal is then post-amplified by 29 dB and sampled by a real-time oscilloscope (RTO) for data processing. The RTO used was a Keysight UXR0404A Infiniium with a 40 GHz bandwidth [45].

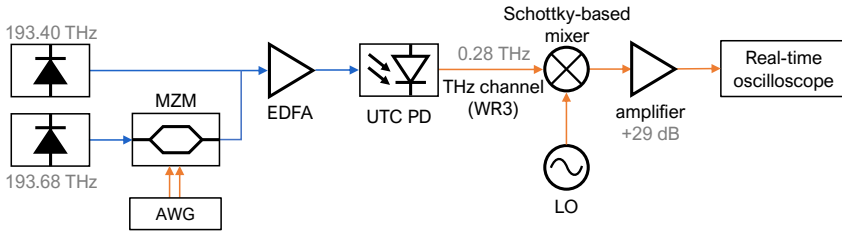


Figure 3.1: In the experimental setup, two separate lasers are used for photomixing. One line is modulated using a MZM, before being combined and amplified by an EDFA. The light is coupled into the PIC using a vertical grating coupler and the mixed terahertz signal is then transferred over a WR-3 waveguide channel before down-mixing and sampling.

To compensate for dispersion introduced by the Schottky-based mixer, a linear equalizer is employed. This equalizer compensates for both the deterministic RF response and IF frequency dependence of the mixer. However, no pre-compensation is applied at the transmit side. Consequently, any remaining distortion is attributed to the uncompensated roll-off behavior of the UTC-PD around 280 GHz.

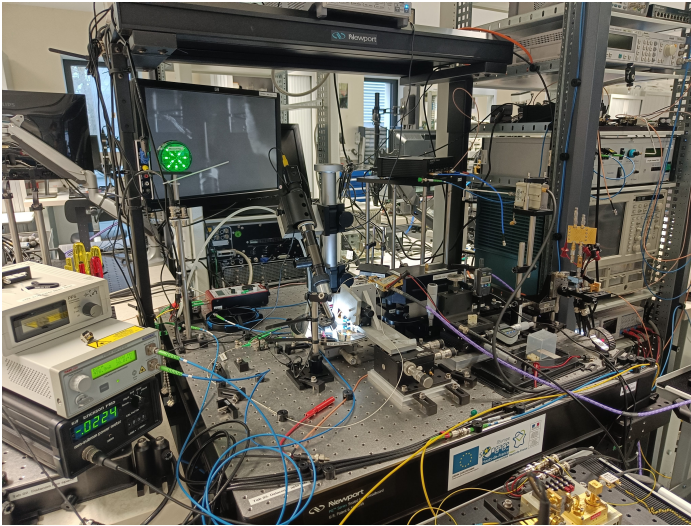


Figure 3.2: Overview picture of the setup: at the heart is the SiN PIC which is probed optically (vertical fiber) and electrically (GSG probe fed to WR-3 waveguide).

### 3.3 System performance

To fully characterize the capabilities and limitations of our communication system working around 300 GHz with the UTC photodiode PIC at its heart, we conducted a series of experiments. Our primary goal was to push the system to its limits by manipulating three key parameters: the constellation format, the symbol rate, and optical power. By incrementally increasing the symbol rate and switching to more complex modulation formats, we aimed to determine the maximum data throughput achievable while maintaining acceptable signal quality. Concurrently, we varied the optical power incident on the photodiode by adjusting the output power of the Erbium-Doped Fiber Amplifier (EDFA). This allowed us to investigate the system's behavior under different photocurrent conditions, providing insights into the photodiode's linearity and noise contributions. During these experiments, we focused on Error Vector Magnitude (EVM) as our primary indicator of signal quality. This methodical approach enabled us to comprehensively assess the potential of our integrated photonic solution for high-speed THz communications and identify any limiting factors in the current setup.

#### 3.3.1 Error Vector Magintude (EVM)

Error Vector Magnitude (EVM) is an important metric in digital communication systems that quantifies the quality of modulated signals. It measures the difference between the ideal symbol locations and the actual received symbol locations in the I-Q plane. The EVM provides a comprehensive assessment of various impairments affecting signal quality, including noise, distortion, and phase errors. Expressed as a percentage, it is calculated using the following formula:

$$\begin{aligned} \text{EVM}_{\text{RMS}} &= \sqrt{\frac{P_{\text{error}}}{P_{\text{symbol}}}} \times 100\% \\ &= \sqrt{\frac{\frac{1}{N} \sum_{n=1}^N |S_n - S_{0,n}|^2}{\frac{1}{N} \sum_{n=1}^N |S_{0,n}|^2}} \times 100\% \end{aligned} \quad (3.1)$$

with  $S_n$  the normalized  $n$ -th symbol  $S_{0,n}$  the corresponding ideal normalized constellation point and  $N$  is the number of unique symbols in the constellation. The normalized symbols represent the complex value of the plane, after scaling all symbols to fit within the rectangle in the I-Q plane, limited by  $[-1, 1]$  and  $[-j, j]$ , on the I- and Q-axis respectively.

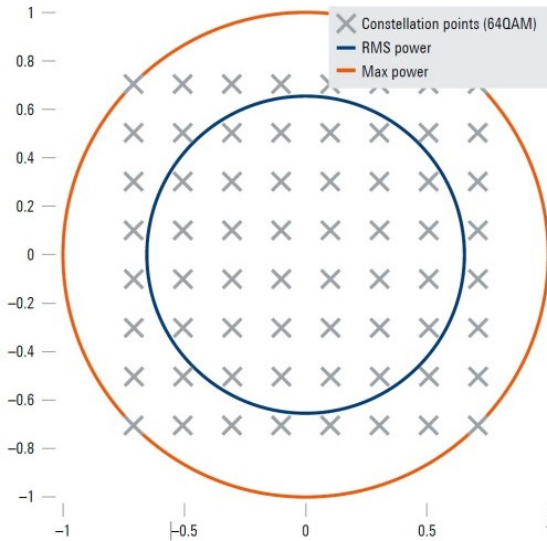


Figure 3.3: Normalizing the EVM of a 64-QAM constellation to its peak or RMS power will lead to a significantly different value. [47]

However, some applications also use the peak power of the reference signal as the reference power instead of the RMS power. This is, for example, the default normalization reference on Keysight equipment [46]. Figure 3.3 shows a comparison between the two power references for a 64-QAM constellation diagram.

Using peak power normalization usually results in values that provide a more physical representation of the signal quality. This is because most systems are fundamentally limited by a maximum absolute power or modulation depth. For example, the MZM in our experiment has a finite modulation depth that constrains the maximum achievable signal swing. In such cases, peak-referenced EVM directly reflects the signal distortion relative to this physical limitation.

On the other hand, using the RMS power normalization offers some different advantages. Most notably, it provides a consistent basis for comparison across different modulation formats and system configurations. Because the RMS value accounts for the actual signal power distribution, it allows for a fair comparison of EVM performance between different constellations and better corresponds to the OSNR. Additionally, the RMS-referenced EVM is more directly related to the statistical properties of the noise and distortion, making it a more robust indicator of overall system quality.

Another benefit of using EVM as a performance metric compared to bit error rate (BER) tests, is the reduced measurement time. Especially for high signal-to-noise ratios (SNR), one should run the experiment for a very long time to detect just a handful of bit errors. On the other hand, it is possible to predict the BER based on a statistical analysis of the constellation points with a cloud of only a few thousand received symbols. If one assumes only additive white Gaussian noise (AWGN), and no other impairments caused by nonlinearities, the BER can be easily approximated with a Q-function [48], which is simply a scaled error function:

$$Q(x) = \frac{1}{2} - \frac{1}{2} \operatorname{erf}\left(\frac{x}{\sqrt{2}}\right) \quad (3.2)$$

E.g. the estimated BER for QPSK and 16-QAM is given by:

$$\operatorname{BER}_{\text{QPSK}} \approx \frac{1}{2} Q\left(\sqrt{\frac{1}{\operatorname{EVM}_{\text{RMS}}^2}}\right) \quad (3.3)$$

$$\operatorname{BER}_{16\text{-QAM}} \approx \frac{3}{4} Q\left(\sqrt{\frac{1}{10 \times \operatorname{EVM}_{\text{RMS}}^2}}\right) \quad (3.4)$$

For 32-QAM, and other constellations where the number of unique symbols is not a power of 2, this formula is less straightforward. We can still approximate this by the generalized formula published in [48] (cfr. formula 13). In the case of 32-QAM, the BER is given by the following equation where  $L$  denotes the count of levels per dimension of the constellation, which comprises  $M$  distinct constellation points.

$$\operatorname{BER}_{32\text{-QAM}} \approx 0.645 \times Q\left(\sqrt{\frac{0.443}{5 \times \operatorname{EVM}_{\text{RMS}}^2}}\right) \quad (3.5)$$

### 3.3.2 Results

The aim of the first experiment was to stress test the system and push the system to its limits in terms of achievable data rate, while maintaining a (near) bit error-free operation and also collecting a significant amount of data points. This conservative approach allowed us to establish a baseline performance. By focusing on this high-speed, error-free target, we aimed to

quantify the maximum potential of our 300 GHz link based on the heterogeneously integrated UTC photodiode. The highest data rate we achieved was 160 Gbit/s (32-QAM at 32 GBd) with an  $\text{EVM}_{\text{PK}}$  of 9.2 %.

A unique feature of this photodiode is its high-bandwidth operation capabilities at low and even zero bias voltage. We repeated the same experiment each time at 0 V bias and only noted a minor decrease in performance, e.g. for the 160 Gbit/s transmission the  $\text{EVM}_{\text{PK}}$  increase to 9.55 %. Table 3.1 gives the EVM and corresponding BER estimate based on the formulas above.

Forward Error Correction (FEC) is a technique used in communication systems to improve the reliability of transmitted data by adding redundant information, allowing for the correction of errors at the receiver. Table 1 shows that all pre-FEC BER values are below  $2.0 \times 10^{-2}$ , meeting the threshold for commonly used Soft-Decision FEC (SD-FEC) decoding schemes with a 20 % coding overhead. Additionally, the top three configurations achieve BERs below  $3.8 \times 10^{-3}$ , the threshold for Hard-Decision FEC (HD-FEC) schemes with a lower 7% overhead [49]. These thresholds highlight the suitability of these configurations for error correction while maintaining efficient data transmission.

The small difference between the  $-1$  V bias and the zero bias case can be explained by the slightly lower responsivity for the same optical power. While the optical power of the Thorlabs EDFA100P erbium-doped fiber amplifier (EDFA) was kept constant at 21 dBm, this resulted in a photocurrent of 2.80 mA and 2.65 mA at  $-1$  V and 0 V respectively. This 5 % lower photocurrent corresponds to a  $-0.5$  dB reduction in RF power. And as such also lowered SNR.

Figure 3.4 shows the constellation diagrams for three different transmission configurations: 16-QAM at 35 GBd (140 Gbit/s), 32-QAM at 25 GBd (125 Gbit/s) and 32-QAM at 32 GBd (160 Gbit/s), and this both at  $-1$  V and 0 V bias voltage.

A second series of experiments was performed to assess the influence of the photocurrent level on the EVM. For a consistent result, this was done at a lower symbol rate of 4 GBd to avoid any influence of other bandwidth limiting devices in the setup. Figure 3.5 shows the relationship between the EVM and photocurrent for both QPSK and 16-QAM modulation schemes. The photocurrent is limited to 1 mA as this was the maximal photocurrent achievable with the Thorlabs EDFA100P erbium-doped fiber amplifier (EDFA), which showed lower noise levels than the higher-powered Man-

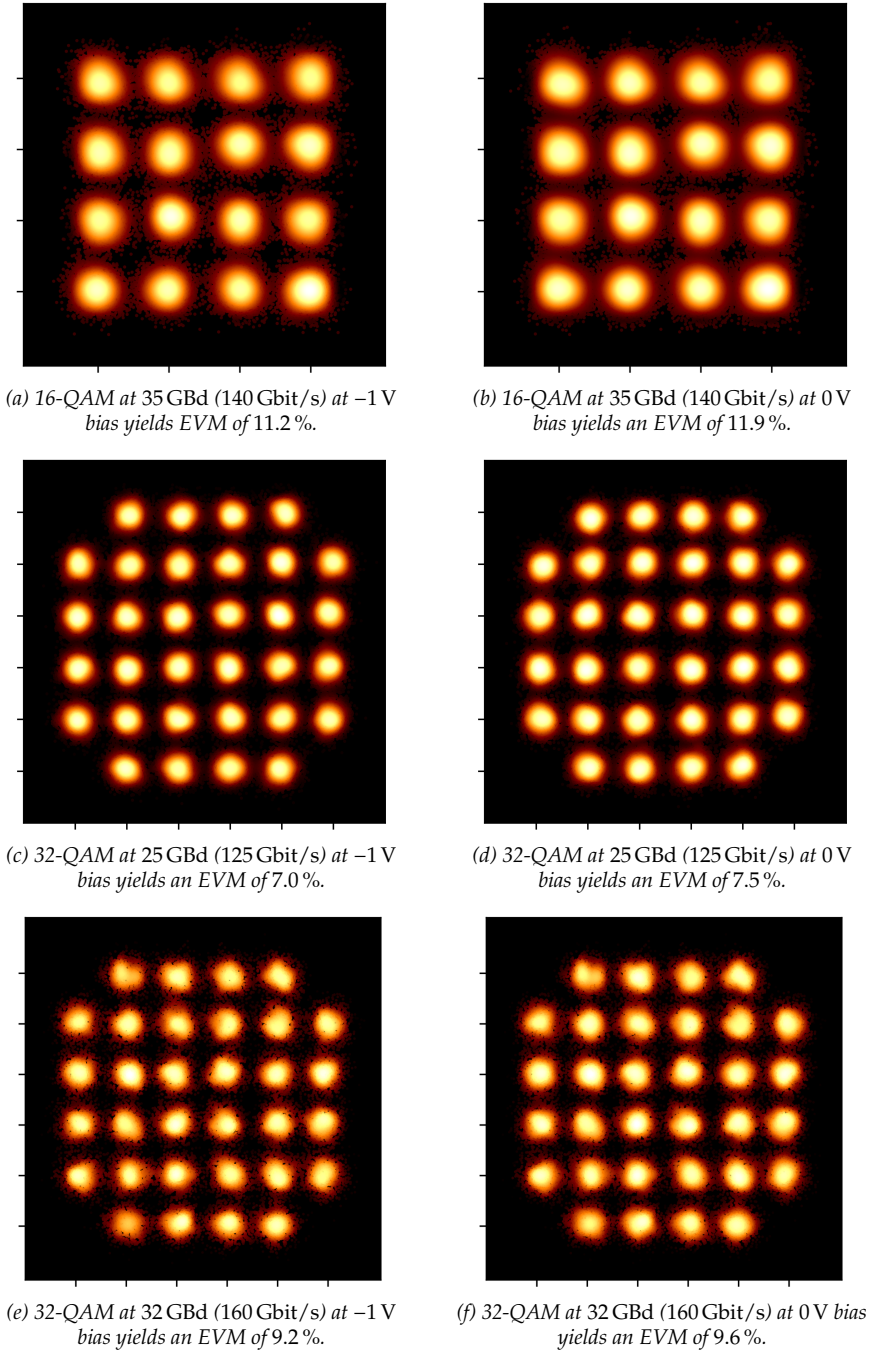


Figure 3.4: All constellation points are clearly distinguishable, even for transmissions up to high data rates of 160 Gbit/s. There is almost no difference between  $-1$  V and 0 V bias.

Table 3.1: EVM and estimated BER values for the high-speed data experiments at 300 GHz.

Constellation	Baud rate	Bit rate	Bias	EVM <sub>pk</sub>	EVM <sub>RMS</sub>	BER
16-QAM	35 GBd	140 Gbit/s	-1V	11.2%	15.9%	1.8E-3
16-QAM	35 GBd	140 Gbit/s	0V	11.9%	16.9%	3.1E-3
32-QAM	25 GBd	125 Gbit/s	-1V	7.0%	11.7%	3.5E-3
32-QAM	25 GBd	125 Gbit/s	0V	7.5%	12.5%	5.6E-3
32-QAM	32 GBd	160 Gbit/s	-1V	9.2%	15.4%	1.7E-2
32-QAM	32 GBd	160 Gbit/s	0V	9.6%	16.0%	2.0E-2

light EDFA.

For increasing power, the EVM decreases according to an inversely-quadratic fit. This demonstrates that the EVM is noise limited, and no linearity effects occur at 1 mA. This behavior is consistent with the expected linear enhancement of the SNR as the photocurrent increases, which is indeed inversely related to the EVM [48]:

$$\text{SNR} \approx \frac{1}{\text{EVM}^2} \quad (3.6)$$

A third experiment was done to understand the relationship between the EVM and the symbol rate. The photodiode was biased at  $-1$  V and the optical power was fixed, to maintain a constant photocurrent of 1 mA between all measurements. The frequencies of both DFB lasers was still the same, with an offset of 280 GHz. Figure 3.6 shows the results, again for both QPSK and 16-QAM modulation schemes. The graph shows a clear linear trend of increasing EVM (RMS normalized) as the symbol rate increases for both modulation formats. The EVM increases from about 7% at 4 GBd to more than 18% at 32 GBd. It is also clear that for 16-QAM, bandwidth-induced limitations can be seen for symbol rates beyond 20 GBd, where the measured values start to deviate from the linear fit.

This can be intuitively explained by the constant output current of the PD, in combination with the increasing bandwidth corresponding to higher symbol rates. First there is the Amplified Spontaneous Emission (ASE) noise from EDFA that will increase linearly with the higher bandwidth, and secondly there is the thermal noise of the receiver that also scales linearly. The shot noise is constant for the same photocurrent. Combined, this yields the linear relationship between the symbol rate  $f_s$  and the EVM.

At the highest symbol rates, 28 GBd and 32 GBd, it can be seen that the EVM

---

values for the 16-QAM scheme start to deviate from the linear fit. This is due to a small reduction in modulation depth when the MZM approaches its 3-dB bandwidth, as well as the non-flat frequency response of the PD, due to its roll-off characteristics around 300 GHz. The effect is indeed more pronounced for a multi-level modulation format like 16-QAM than QPSK.

### 3.4 Conclusion

In this chapter, we have demonstrated the successful operation of a uni-traveling-carrier (UTC) photodiode, heterogeneously integrated on a Silicon Nitride (SiN) platform, for high-speed wireless communications at 300 GHz. Our experimental setup, utilizing this novel device, achieved impressive data rates going up to 160 Gbit/s while maintaining good signal integrity for different data constellations (QPSK to 32-QAM) and symbol rates (4GBd to 32 GBd). The relationship observed between photocurrent and EVM provided valuable insights into the system's limitations and showed that the system is in fact noise limited at least up to photocurrents of 1 mA.

These results underscore the potential of heterogeneously integrated photonic devices for next-generation wireless communication systems. The successful operation at 300 GHz with high data rates paves the way for further research into terahertz communications, addressing the growing demand for increased bandwidth in future networks. While challenges remain in pushing the boundaries of speed and signal quality, our work represents a significant step towards realizing compact, efficient, and high-performance photonic-enabled terahertz communication systems.

### 3.5 Ongoing and Future work

While our current research has demonstrated the potential of integrated UTC photodiodes on SiN platforms for 300 GHz communications, there are several avenues for improvement and expansion that we are actively pursuing. These developments aim to address practical limitations and enhance the system's overall performance and applicability.

One of the primary challenges in our current setup is the relatively low absolute power output, which may be insufficient for realistic, long-range communication systems. To address this limitation, we are exploring the integration of electronic power amplifiers (PAs) with our UTC photodiodes. This combination would significantly boost the output power, extending the potential range and reliability of the communication link. Specifically, we have initiated work on integrating a D-band (from 110 to 170 GHz) PA with our photonic integrated circuit (PIC). This integration is being achieved through a flip-chip bonding process, co-integrated right next to the transfer-printed PDs. This approach allows us minimize the interconnect losses between the photodiode and PA. It's worth noting that while this work focuses on the D-band due to the availability of suitable amplifiers, similar semiconductor solutions for sub-THz frequencies are not yet readily available.

To fully leverage the potential of this integrated PA approach, we are utilizing the improved photodiodes described in the future work section of Chapter 2. These advanced photodiodes potentially offer bandwidths exceeding our current record of 155 GHz. This ongoing work represents the next step towards realizing practical, high-performance terahertz communication systems based on integrated photonic technologies. By addressing key limitations such as output power and system integration, we are paving the way for the next generation of wireless communication infrastructure that can meet the ever-increasing demands for bandwidth and connectivity.

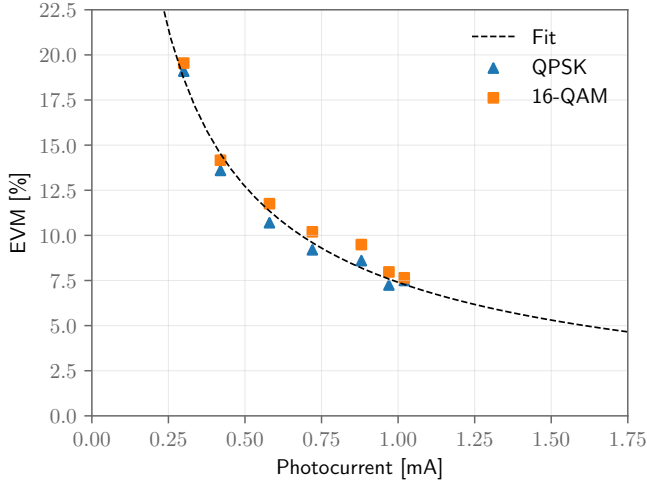


Figure 3.5: Error Vector Magnitude (EVM) versus Photocurrent for QPSK and 16-QAM modulation schemes at a symbol rate of 4 GBd in a 300 GHz communication link.

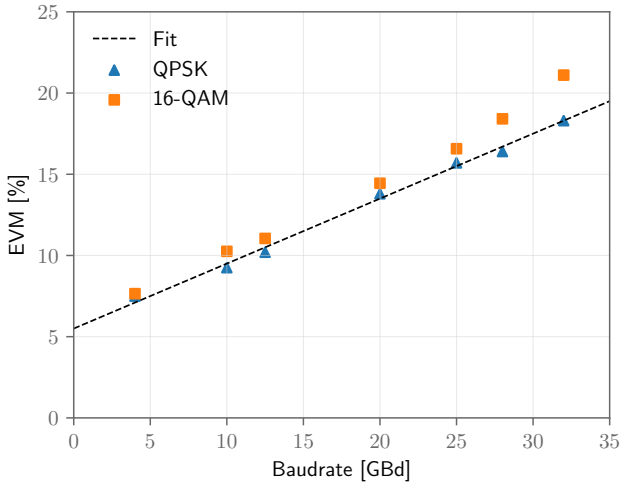


Figure 3.6:  $EVM_{RMS}$  versus the symbol rate for QPSK and 16-QAM modulation schemes at in a 300 GHz communication link using an integrated UTC photodiode on SiN.

# 4

## A high-speed datacom link enabled by UTC photodiodes on SiN

Expanded on the "UTC Photodiodes on Silicon Nitride Enabling 100 Gbit/s" proceedings of the 2022 European Conference on Optical Communication (ECOC).

---

<b>4.1</b>	<b>Introduction</b>	<b>62</b>
<b>4.2</b>	<b>Experimental setup for an IM/DD link</b>	<b>63</b>
<b>4.3</b>	<b>System performance</b>	<b>64</b>
4.3.1	From line rates to net bit rates	65
4.3.2	Results	66
<b>4.4</b>	<b>Conclusion</b>	<b>68</b>
<b>4.5</b>	<b>Towards coherent detection</b>	<b>68</b>
4.5.1	Chip design	70
4.5.2	Fabrication (and its challenges)	72
<b>4.6</b>	<b>Future work</b>	<b>75</b>

---

## 4.1 Introduction

In recent years, the demand for data transmission has been growing at an unprecedented rate. This exponential increase in data traffic poses significant challenges for both inter- and intra-data center interconnects. To address these challenges, high-speed optical transceivers are essential for supporting the next generation of data center interconnects, single links of 1.6 Tbps or faster [50].

Silicon photonics (SiPh) has emerged as a leading technology for high-speed integrated transceivers and is widely adopted in commercial products. Although Silicon-On-Insulator (SOI) platforms are currently the preferred flavor of integration platform, Silicon Nitride (SiN) offers distinct benefits that make it an attractive alternative. In the context of data center communications, SiN presents several key advantages over traditional SOI platforms:

1. Lower propagation losses: SiN waveguides typically exhibit lower propagation losses compared to their silicon counterparts, enabling longer optical paths and more complex integrated circuits. This is particularly beneficial for intra-data center links where signal integrity over distance is crucial.
2. Reduced thermal sensitivity: The lower thermo-optic coefficient of SiN enhances the stability of optical filters and resonators, which is critical for maintaining consistent performance in the variable thermal environments of data centers.
3. Higher power handling: The absence of two-photon absorption in SiN at common datacom wavelengths allows for higher optical power levels without performance degradation. This characteristic is especially valuable in intensity-modulated direct-detection (IM/DD) systems, where higher optical power can translate to improved signal-to-noise ratios and extended reach.
4. Superior filtering capabilities: The ability to fabricate high-quality factor (Q-factor) components in SiN enables the realization of high-extinction-ratio filters and arrayed waveguide gratings (AWGs) for dense wavelength-division multiplexing (DWDM). These components are critical in maximizing the spectral efficiency of optical communication systems, thus increasing the overall data capacity of interconnects.

These properties make SiN platforms particularly well-suited for datacom applications [51]. However, on SiN, no active devices can be grown directly. Amplifiers, modulators, and detectors need to be integrated heterogeneously. This can be done using, for example, wafer-bonding a III-V wafer, or micro-transfer-printing III-V chiplets, on SiN waveguides. Lasers and amplifiers integrated on SiN have been demonstrated [52]. However, the bandwidth performance of detectors demonstrated so far was inferior compared to their SOI counterparts. In chapter 2, we discussed the fabrication and high-speed performance of UTC PDs on the said SiN platform.

In this chapter, we focus on an experimental demonstration of such a high-speed photodetector integrated on a SiN circuit for datacom applications. Specifically, we showcase a 200-meter IM/DD link enabled by this PIC. The experiment aims to explore the limits of data transmission rates achievable with such a configuration and its potential for high-speed interconnects. We will describe the system we built to test this PIC, explain the metrics used to benchmark the system, and the results obtained.

## 4.2 Experimental setup for an IM/DD link

To demonstrate the performance of the waveguide-integrated PD, a short-reach intensity modulation and direct detection (IM/DD) system is set up. This type of optical link is commonly used in fiber optical networks thanks to its simplicity, cost-effectiveness, and robustness. No additional methods of multiplexing, e.g. wavelength division multiplexing (WDM) or polarization division multiplexing (PDM), were used. The UTC PD used in this experiment has a mesa size  $2 \times 16 \mu\text{m}^2$  with a responsivity of 0.3 A/W, and a 3-dB bandwidth of more than 100 GHz. Figure 4.1 shows the SiN PIC with the transfer-printed PD.

In figure 4.2 a schematic of the system with all components can be seen. At the transmitter, a 1550 nm continuous laser signal at a power of 15 dBm is modulated using a Mach-Zehnder Modulator (MZM) biased at the quadrature point. The MZM has a 6-dB bandwidth of 45 GHz and a smooth frequency response roll-off. The electrical signal fed into the MZM is generated by an arbitrary waveform generator (AWG) with a 3 dB bandwidth of 65 GHz, and amplified by an 11 dB driver amplifier with 70 GHz 3-dB bandwidth. Pre-emphasis is applied up to 75 GHz, de-embedding the frequency response of the AWG and driver amplifier, while the frequency response of the MZM is left uncompensated. The optical power at the output of the MZM is 4 dBm. The modulated optical signal is then transmitted over

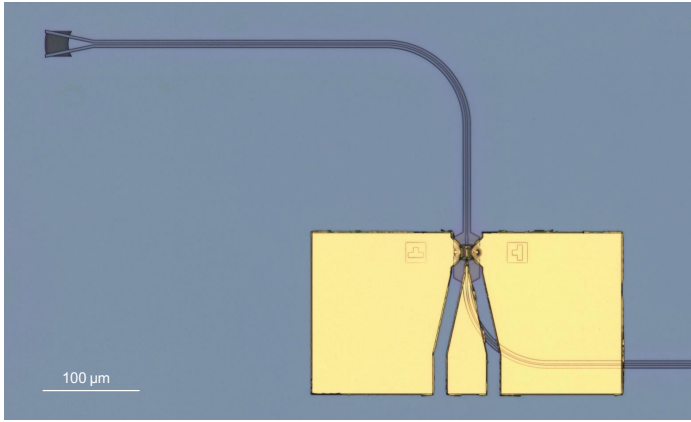


Figure 4.1: The device under test (DUT): a SiN chip with a transfer-printed UTC photodiode.

200 m single-mode fiber (SMF).

At the receiver side, the optical signal is amplified to 23 dBm and passed through a 5 nm band-pass filter to suppress amplified spontaneous emission (ASE) noise. A polarization controller is placed at the input of the UTC PD due to the polarization dependence of the grating coupler. The optical power is 20 dBm at the input of the PIC containing the UTC PD. The grating coupler contributes to 9 dB insertion loss, yielding 11 dBm optical power at the PD. 1.75 mA photocurrent is obtained from the PD, which is then converted to voltage by the  $50\ \Omega$  termination of a real-time oscilloscope (RTO) with 84 GHz bandwidth. This 84 GHz limit is a brick-wall filter to prevent aliasing for the 256 GSa/s sampling in the RTO.

### 4.3 System performance

To evaluate the capability of the UTC PD to support high-speed optical signal detection, pulse-amplitude modulation (PAM) signals with 2, 4, and 8 amplitude levels are transmitted at various symbol rates. In this work, the same transmitter and receiver digital signal processing (DSP) stacks as described in the work of Hu et al. [53] are employed.

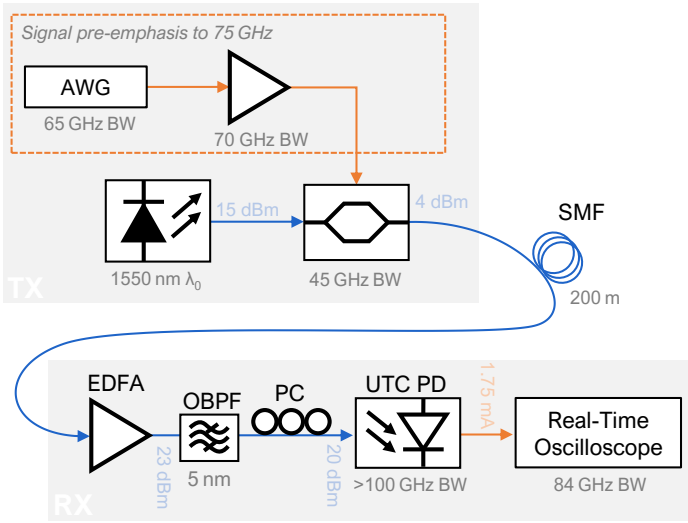


Figure 4.2: The experimental setup of the IM/DD link consists of a MZM and AWG at the transmit side. After transmission over a 200 m-long SMF, this signal is amplified at the receiver side, passed through a polarization controller and band-pass filter, before coupling into the PIC containing the UTC PD. The electrical signal is directly fed into the real-time oscilloscope after opto-electric conversion.

### 4.3.1 From line rates to net bit rates

In a communication system, the line rate (or gross bit rate) is the total number of bits transmitted per second, including both the actual data and any additional bits used for forward error correction (FEC). The net bit rate is the effective data rate, which excludes these additional bits. In our evaluation of the short range data link, we are interested in an accurate estimate of the achievable net bit rate.

A common practice in research on communication systems is to report the FEC limit. It represents the pre-FEC BER at which a specific FEC code can reliably correct errors to achieve a target post-FEC BER (e.g.  $10^{-15}$ ). Using the FEC limit as a performance metric provides a clear and easy-to-understand threshold for system viability.

However, Alvarado et al. proposed in 2015 [54] to replace this standard practice of reporting the FEC limit with a different approach. Their suggestion was to use the (normalized) generalized mutual information (GMI) and the corresponding net bit rate. Especially for complex (multi-level) modulation formats, low code rates, and unpredictable channel conditions,

this metric shows a great increase in accuracy. By stepping away from the single FEC limit, a wider range of limits, each corresponding to different coding scheme with a different coding rate, gives more precision in the achievable net bit rates. The net bit rate also no longer relies on the available coding schemes; e.g. one can achieve a much better performance with a combination of Soft Decision (SD) and Hard Decision (HD) FEC than with a simple HD-FEC scheme.

The choice between reporting FEC limit or GMI often depends on the focus of the research:

- System-level studies or incremental improvements to existing technologies might prefer FEC limit for its simplicity and direct relation to current industry standards.
- Research into novel modulation formats, advanced coding schemes, or pushing the boundaries of channel capacity is more likely to use GMI. It provides a more comprehensive view of the system's potential, especially when the optimal FEC scheme is not yet determined.

In our research, where we focus on the performance of the photodetector as a part of the overall link, and its potential for high-speed data transmission, we preferred the GMI metric. The NGMI is calculated from the channel transition probability, which is computed from the histogram of the equalized signal.

### 4.3.2 Results

Figure 4.3 shows the optical spectrum at the input of the PIC when a 144 GBd PAM-8 signal is transmitted. The LO line is clearly visible at 1549.3 nm with a signal bandwidth from 1548.7 to 1549.9 nm (resp.  $\pm 0.6$  nm), which corresponds to about 75 GHz electrical bandwidth. As such, it is clear that the PD will not form the bandwidth limiting component in this system. This 75 GHz limit arises from the pre-emphasis applied to the signal. Evidently, one would expect a wider spectrum corresponding to a 144 GBd PAM-8 signal.

The captured eye diagram can be seen in Figure 4.4. The 8 levels of the PAM-8 signal are clearly distinguishable.

For our experiment we tested symbol rates starting at 128 GBd up to 200 GBd for PAM-2, up to 160 GBd for PAM-4 and up to 148 GBd for PAM-8. The

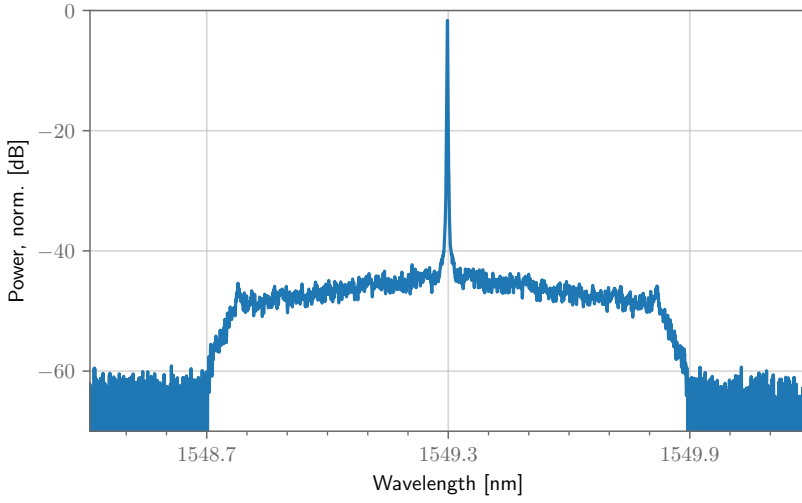


Figure 4.3: Optical spectrum captured with an OSA before coupling into the PIC.

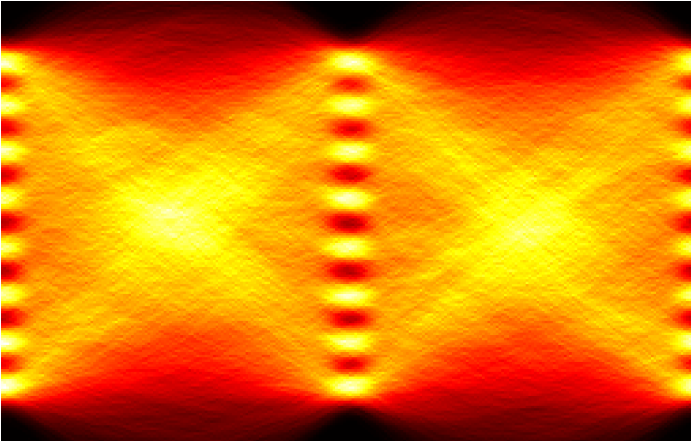


Figure 4.4: Eye diagram of a 144 GBd PAM-8 signal.

results are shown in Figure 4.5. For both PAM-2 and PAM-4 the lower symbol rates yielded a NGMI of near 1, resulting in net bit rates close to the line rate. For PAM-8, the NGMI at 128 GBd dropped already to 0.92 at the starting symbol rate. Peak net data rates of 160.75, 278.84 and 353.97 Gbit/s were achieved, for respectively PAM-2, PAM-4 and PAM-8.

## 4.4 Conclusion

This chapter shows a second demonstration of the heterogeneously integrated photodiodes by means of transfer-printing. Whereas Chapter 3 focused on the potential of these devices for a high-speed wireless link at sub-THz frequencies, this chapter focuses on a data experiment for fixed access interconnects, particularly for data center and short-reach optical communication applications.

Our experimental results demonstrate the potential of this technology for high-speed optical communications. Specifically, we have successfully implemented a short-reach C-band link capable of supporting net data rates exceeding 350 Gbit/s. This achievement underscores the high-performance capabilities of our heterogeneously integrated photodiodes. Furthermore, we pushed the boundaries of non-return-to-zero (NRZ) or Pulse Amplitude Modulation-2 (PAM-2) transmission, demonstrating the ability to achieve symbol rates as high as 200 GBd. This impressive feat resulted in a net data rate of 152 Gbit/s. The ability to achieve such high data rates with NRZ signaling is particularly noteworthy, as it offers a balance between performance and system complexity that could be interesting for practical implementations.

These results not only validate the potential of transfer-printed photodiodes on SiN for high-speed base-band optical communications but also highlight their versatility across different application domains. The successful demonstration in both wireless (Chapter 3) and fixed optical link scenarios (this chapter) underscores the broad applicability of this technology.

## 4.5 Towards coherent detection

The demonstrator system presented in this chapter primarily serves as a proof of concept for the capabilities of a transfer-printed UTC photodetector on SiN. To go beyond this device-level demonstrator, to a system-level

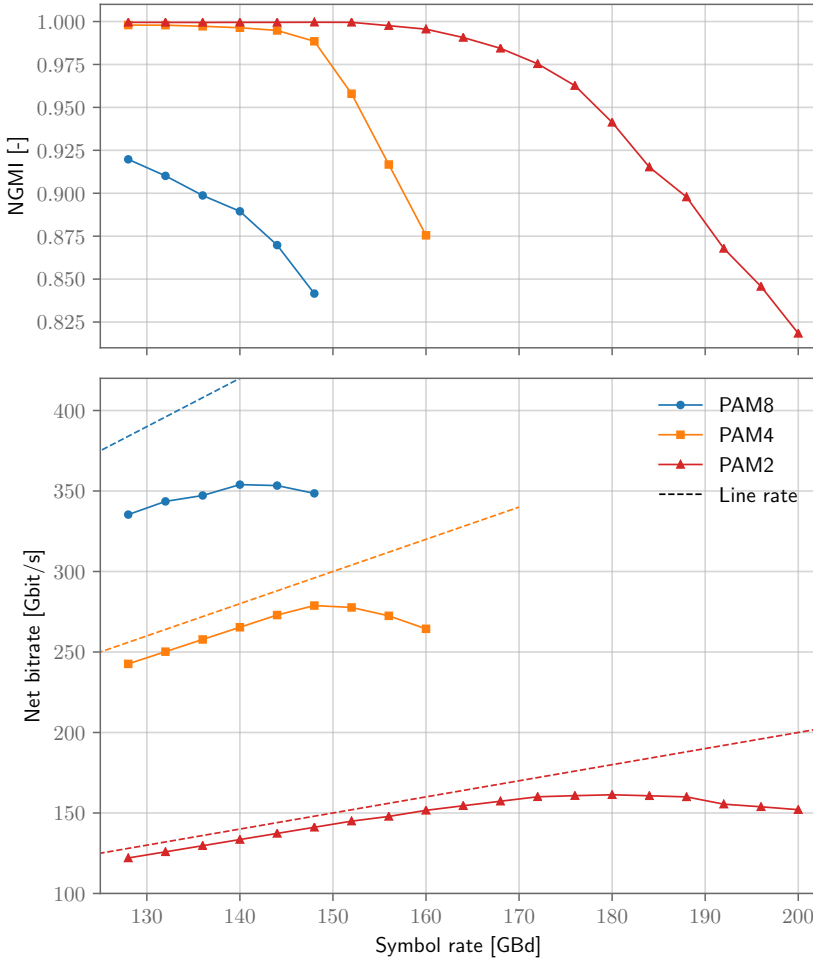


Figure 4.5: The normalized generalized mutual information (NGMI) for PAM-2, PAM-4 and PAM-8 (top) results in net bitrates (bottom) in excess of 350 Gbit/s (PAM-8 at 140 GBd). For PAM-2, symbol rates up to 200 GBd are achieved with a net bitrate beyond 150 Gbit/s

integration, a new chip is designed that makes use of the unique properties of SiN-based photonics. We set the goal to create a dual-channel coherent receiver chip on a commercial SiN platform. This not only represents a significantly more complex photonic integrated circuit (PIC) with advanced system-level circuitry, it also demonstrates the compatibility of micro-transfer printing UTC PDs on different photonic platforms. To further enhance this system, a Transimpedance Amplifier (TIA) chiplet has been co-designed to convert the output currents of the photodiodes to a strong voltage signal.

The selected silicon nitride (SiN) platform is one provided by Ligentec: the 800 nm-thick SiN platform (AN800) that offers Multi-Project Wafer (MPW) runs for academia. This platform has a comprehensive process development kit (PDK) and high-quality components like low-loss edge couplers, optimized multi-mode interferometers (MMIs), and the possibility to locally open up the top cladding. These so-called Local Cavities (LoCa's) are necessary for transfer printing waveguide-coupled PDs.

### 4.5.1 Chip design

A coherent receiver decodes both the amplitude and phase of an optical signal, allowing the system to demodulate signals encoded with advanced modulation schemes (e.g. QAM) that carry information in both amplitude and phase. The architecture of such a receiver centers on a design featuring a 90-degree hybrid coupler and two (pairs of) balanced photodiodes (BPDs): for this, we combine a 4x4 MMI building block with two pairs of identical UTC PD coupons. This balanced photodetection scheme offers improved noise rejection and enhanced sensitivity.

Its operation is conceptually illustrated in Figure 4.6 and can be described as follows:

1. **Optical 90-degree hybrid:** The hybrid takes two inputs: the optical signal ( $S$ ) carrying the information and a local oscillator (LO), a stable laser source. It splits and combines these inputs to generate four output signals:  $S + L$ ,  $S - L$ ,  $S + jL$ , and  $S - jL$ . These represent the in-phase (I) and quadrature (Q) components of the optical fields, where  $j$  indicates a 90-degree phase shift (corresponding to the imaginary axis in a complex plane).
2. **Balanced Photodiodes (BPDs):** The outputs of the hybrid are fed into two balanced photodiodes (made out of pairs of UTC PDs). A

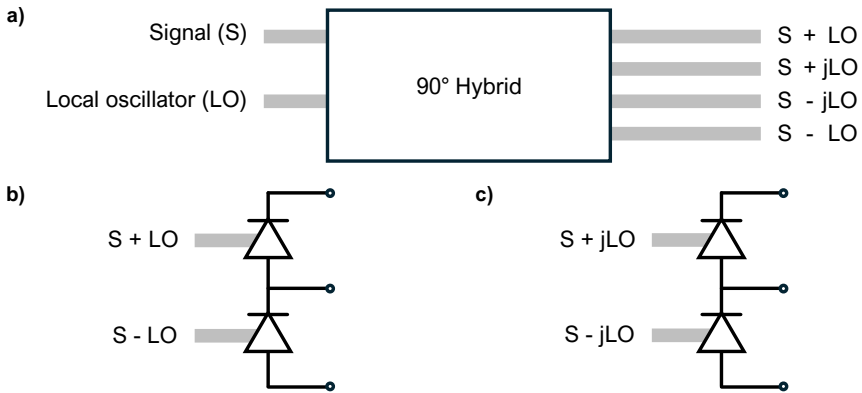


Figure 4.6: (a) A  $90^\circ$  hybrid provides four outputs with a different phase relationship between the received signal and local oscillator. In (b) and (c) the corresponding connections to the balanced PD inputs are shown.

balanced photodiode subtracts the photocurrents generated by two input optical fields:

- One balanced photodiode receives  $S + L$  and  $S - L$ , and calculates the difference, yielding a signal proportional to the in-phase component ( $I$ ).
- The other balanced photodiode receives  $S + jL$  and  $S - jL$ , and calculates a signal proportional to the quadrature component ( $Q$ ).

The balanced photodiodes convert the optical signals into electrical signals representing the real ( $I$ ) and imaginary ( $Q$ ) parts of the optical field. By combining these, the receiver reconstructs the full complex envelope of the signal, including both its amplitude and phase.

The full design can be seen in Figure 4.7, and covers an area of  $1.9 \times 2.6 \text{ mm}^2$  area on a larger multi-project chip. At its core, the design of this chip features two coherent receiver blocks, each capable of demodulating coherent optical signals. In Figure 4.7, eight UTC PD coupons are printed to form the four balanced output photodiode stages, but not yet metalized to connect the coupon to the bond pads. This is shown in Figure 4.8, where two coupons are combined with metal traces to create a single balanced photodiode pair.

To facilitate efficient light coupling into the chip, the design includes a low-loss edge coupler. This building block ensures minimal insertion losses, enabling high-quality signal transfer from external fibers to the integrated

waveguides. Alternatively, a grating coupler is also included as a backup way of characterizing the chip. The Mach-Zehnder Interferometer (MZI)-based splitter at the input of the chip is inherently a polarization beam splitter, but since there is no mechanism to manipulate polarization within this design, it will instead be utilized as a wavelength splitter, leveraging its ability to separate light based on wavelength.

The local oscillator (LO) signal input strategy is flexible, supporting two distinct pathways: a grating coupler input or an on-chip external cavity laser. By using transfer printing to include a semiconductor optical amplifier (SOA) in the central cavity, the chip can generate a coherent LO directly on the PIC. Initially, however, the focus will be on using an external laser source coupled into the chip via a grating coupler, providing a straightforward and reliable approach to validate the receiver's performance.

#### **4.5.2 Fabrication (and its challenges)**

After receiving the SiN chips from Ligentec, the fabrication involves multiple post-processing steps in the clean room of Ghent University. These processes, unfortunately, require significant optimization challenges.

1. First, the micro-transfer printing of the photodiodes (and optionally a laser coupon) in the foreseen local cavities (LoCa's). The initial coating with BCB using spin-coating gave covering issues. To get a thin, uniform, layer of BCB, we switched to a spray coating the samples using the EVG 101 system.
2. Secondly, vias needed to be etched in the coupons after printing, which proved problematic inside the LoCa. To address this issues, the more advanced coupons (discussed in Section 2.6) with pre-etched vias were used.
3. Thirdly, the interconnection of the coupons to the bond pads requires a final metallization step. For this we used a standard TI-35 photoresist recipe and 800 nm-thick gold layer.

Post-fabrication, the chip will be precisely diced, with its four output channels wire-bonded to the co-designed electrical transimpedance amplifier (TIA) developed in collaboration with the IDlab design group. The pitch of the bond pads on both dies is identical, to ensure minimal wire-bond distance and thus parasitics.

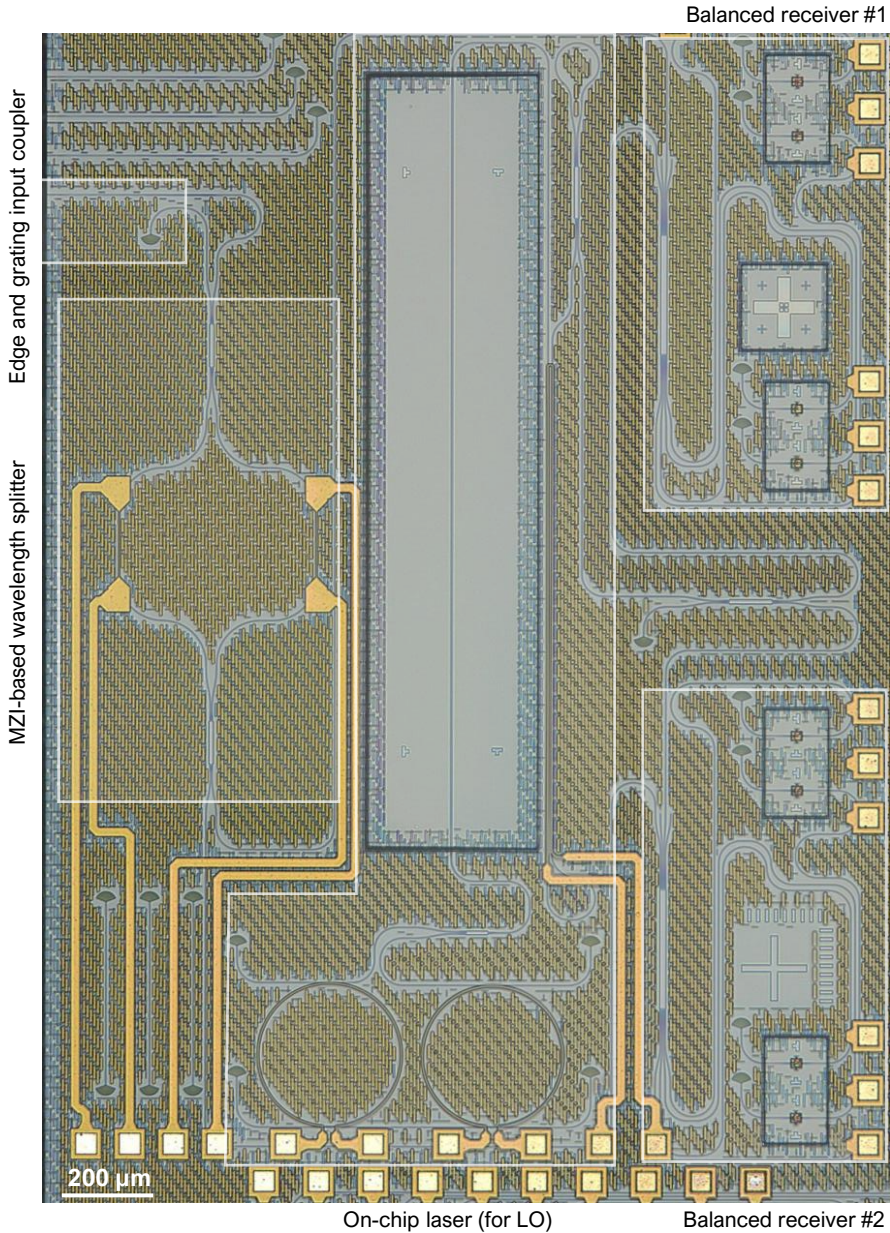


Figure 4.7: Picture of the Ligentec PIC with a dual-channel balanced receiver. Received signal can be coupled in with either grating or edge coupler (left top), and is then split by an MZI-based wavelength splitter. Support for an on-chip LO signal is foreseen (transfer-printed laser coupon). Two balanced receiver circuits are made out of a 4x4 MMI and two balanced photodiode (BPD) pairs.

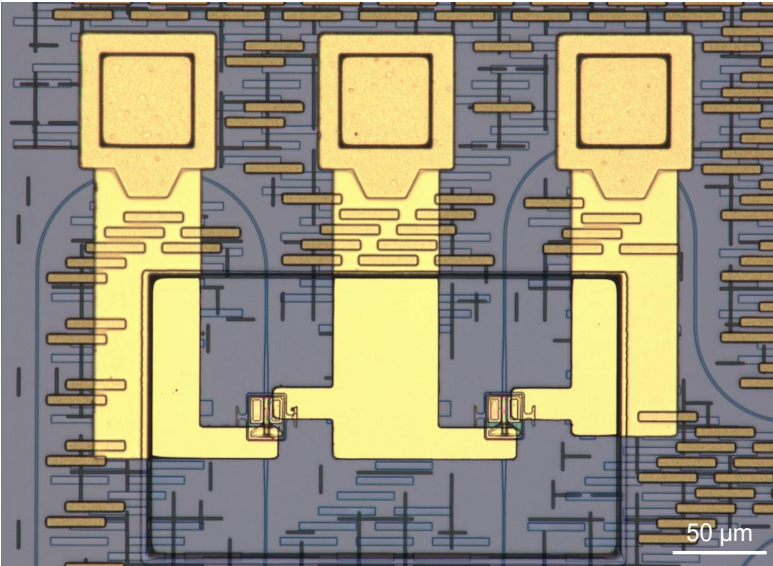


Figure 4.8: Two identical transfer-printed UTC PD coupons are combined to form a balanced photodiode (BPD).

As an alternative approach to the Ligentec-based coherent receiver, we explored the possibility of using our in-house 300-nm thick SiN platform to develop the coherent receiver. For this, an optimized 4x4 MMI was designed, with simulation results demonstrating promising performance (as shown in Fig. 4.9). This MMI was intended to form the core of the optical hybrid needed for coherent detection. However, initial measurements revealed larger-than-expected phase errors in the fabricated device, suggesting deviations from the design or imperfections in the fabrication process. These discrepancies highlight the need for further research to refine the design and improve the fabrication tolerances, ensuring that this alternative approach can achieve the required performance for practical applications.

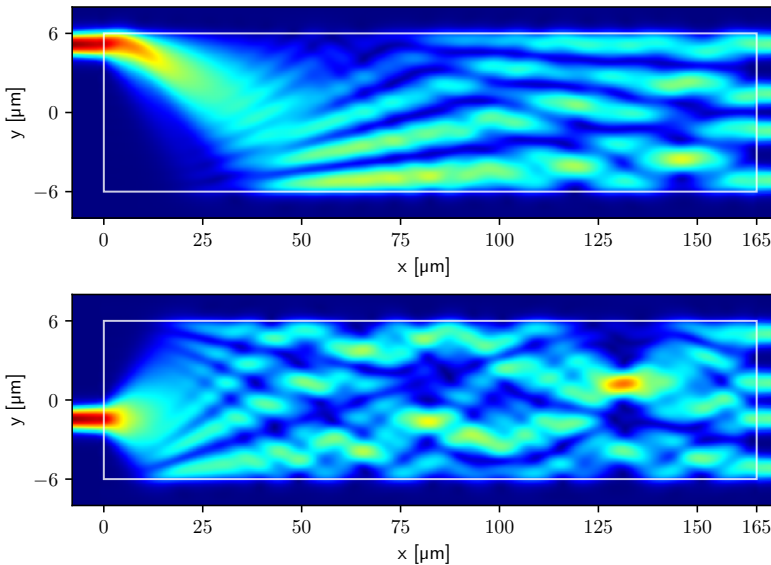


Figure 4.9: Simulation results for a 4x4 MMI on 300 nm-tick SiN platform using Lumerical EME. The edges of the core slab are highlighted in white.

## 4.6 Future work

This research on high-speed photodiodes on SiN platforms has opened up exciting avenues for future exploration and development. Building upon the results of this chapter, future work could pursue even higher data rates based on the current intensity modulation/direct detection (IM/DD) link. The setup presented in this chapter is limited by the bandwidth of the modulator and driver amplifier, which are the bottlenecks in achieving higher data rates. To address this, we propose replicating our experiments using more advanced components. In line with the high-speed photodiodes on SiN, one could use a modulator based on transfer-printing of Lithium Niobate (LN) on the same SiN platform. Recently, promising results have been shown with LN-based modulators with very high bandwidths [6]. These improvements should allow us to surpass our current 350 Gbit/s benchmark.

Secondly, as discussed in section 4.5, we are working on expanding the functionality of the SiN circuitry. Whereas the functionality of the PIC in the demonstrator of this chapter was limited to a proof of concept of the capabilities of SiN coupling and interconnects, the proposed dual-channel coherent receiver truly leverages the benefits of the SiN platform. The move

to coherent detection offers several advantages, including increased spectral efficiency for higher data rates within the same bandwidth, improved receiver sensitivity for extended reach, and the ability to compensate for various channel impairments through digital signal processing.

By pursuing these research directions, we aim to significantly advance the state-of-the-art in integrated photonics for high-speed optical communications. The combination of our transfer-printed photodiodes with advanced modulation techniques and coherent detection schemes has the potential to meet and exceed the demanding requirements of next-generation data center interconnects and telecommunications networks. As we continue this work, we anticipate uncovering new challenges and opportunities that will contribute to the future of optical communication technologies.

# 5

## Conclusion and Outlook

---

<b>5.1</b>	<b>General Conclusions . . . . .</b>	<b>77</b>
<b>5.2</b>	<b>Outlook &amp; Perspectives . . . . .</b>	<b>79</b>
5.2.1	Improved UTC photodiode chiplets . . . . .	79
5.2.2	Complex SiN-based photonic systems . . . . .	79
5.2.3	Opto-antennas for THz communication . . . . .	80
5.2.4	Micro-transfer printing at high TRL . . . . .	80

---

### 5.1 General Conclusions

This PhD thesis set out to address the challenges in developing integrated photonic solutions for terahertz (THz) communications, with a particular focus on creating faster transducers for THz photonics and integrating these devices on Silicon Nitride (SiN) photonic platforms. We tackled these challenges by searching for the overarching research questions set out in the introduction: how can we make faster transducers for THz photonics, how to fabricate these devices on SiN photonics, what is their performance, and how do we incorporate them in modern communication systems?

The most important achievement of this research is the successful integra-

tion of waveguide-coupled uni-traveling carrier (UTC) photodiodes on a SiN photonic integrated circuit (PIC) platform through micro-transfer printing. As discussed in detail in Chapter 2, our approach offers significant advantages by separately fabricating the III-V waveguide chiplet (coupon) and the SiN PIC. This approach also ensures efficient material usage and compatibility with industry-standard PIC manufacturing standards.

The UTC photodiodes developed in this work demonstrate remarkable characteristics, most notably a record-high bandwidth of 155 GHz at low bias voltages and 135 GHz at zero bias. To the best of our knowledge, these results represent the fastest photodiode integrated on a SiN platform and the fastest zero-bias photodiode across all platforms, marking a significant advancement in high-speed photodetectors.

The potential of these heterogeneously integrated photodiodes was demonstrated in two distinct application scenarios. The first experiment was set up in the realm of wireless communications in the sub-THz band. We successfully operated a UTC photodiode at 300 GHz, achieving impressive data rates up to 160 Gbit/s, while maintaining good signal integrity for various data constellations and symbol rates. This demonstration underscores the potential of our devices for next-generation wireless communication systems, addressing the growing demand for increased bandwidth in future networks.

The second demonstration, in the domain of fixed access interconnects, was discussed in Chapter 4. We showcased a short-reach C-band link capable of supporting net data rates, i.e. taking into account the overhead for error correction, exceeding 350 Gbit/s, and also NRZ transmissions achieving symbol rates up to 200 GBd. These results not only validate the potential of transfer-printed photodiodes on SiN for high-speed baseband optical communications but also highlight their versatility across different application domains.

It's important to recognize that this PhD project represents just one small step in the ongoing development of THz communication systems and SiN photonics. And while the vision of fully integrated on-chip THz transmit arrays remains a future goal, this work has made important contributions towards its realization. By developing novel components for THz generation through photomixing and advancing the SiN-based photonic platform, we have removed some technological roadblocks. As we – and other researchers around the world – continue to push the boundaries of speed, efficiency, and integration in photonic devices, each small step brings us closer to realizing the full potential of THz communications.

## 5.2 Outlook & Perspectives

Most innovations in science and technology are built on a series of incremental advancements, yet they are motivated by the perspective of a much larger leap of technological advancement and a vision of future systems. In each chapter of this dissertation, we already had a look at some new research questions that arose and the future research that is already being undertaken. In the following sections, we try to look at the bigger picture of the technologies being researched and the direction they are headed.

### 5.2.1 Improved UTC photodiode chiplets

To start, future research should stay close to the findings of this PhD and can look at incremental improvements to the photodiode chiplets for SiN PICs. New and improved designs and optimized fabrication techniques can further increase the bandwidth and power output of waveguide-coupled UTC photodiodes. Better fabrication accuracy can reduce the coupon size, consequently decreasing the RC-bandwidth limitation, which is the current bandwidth bottleneck. In doing so, the responsivity, but also fabrication yield and compatibility, should not be overlooked. Chapter 1 reveals some insight in what this might mean in the short term.

### 5.2.2 Complex SiN-based photonic systems

In this PhD work, we showed system demonstrations using newly developed technology. However, these experiments, discussed in chapters 3 and 4, still rely on many external, bulky, fiber-based components. A next step in this research would be to incorporate more components and functionality on a single chip, moving complexity from the characterization setup onto the photonic circuit. For example, by transfer printing laser coupons and making a modulator on the PIC, the whole optical part of the photomixing setup would move on chip, greatly reducing the complexity of the setup. In the outlook of chapter 4 we give initial results of more complex systems based on the waveguide-coupled photodiodes: a dual channel coherent receiver with balanced detectors, as well as a co-designed electrical amplifier. Research into such complex systems with also co-integrated electronics is needed.

### **5.2.3 Opto-antennas for THz communication**

One could also look at the electrical side of the photodetector, and make a chip with an integrated THz antenna. In this research, the co-design of the THz antenna with the transfer-printed photodetector could significantly improve the THz output by minimizing the interconnect losses, but also poses great challenges on the antenna design. Such a system, with an optical input, directly producing THz radiation, would be one of the first THz opt-antennas.

### **5.2.4 Micro-transfer printing at high TRL**

Looking ahead, at the future research of micro-transfer printing ( $\mu$ TP) as a technology in general, a demonstration of high-yield, wafer-scale performance will be crucial for industrial adoption of the technology. While this thesis has shown the potential of micro-transfer printing for integrating high-speed photodiodes on SiN, scaling this process to wafer level with consistent, high-yield results will be critical for commercial viability. Moving this technology to a higher Technology Readiness Level (TRL) will involve optimizing the transfer printing process by automating the printing process and ensuring uniformity across large areas. Furthermore,  $\mu$ TP could become a key enabling technology for not only next-generation photonic integrated circuits, but many sorts of microchips.



# Fabrication recipes

---

A.1 Dry etch recipes . . . . .	81
A.2 Wet etch recipes . . . . .	83
A.3 Lithography recipes . . . . .	84
A.4 Deposition recipes . . . . .	85

---

## A.1 Dry etch recipes

The following recipes are used for plasma etches, as described in Chapter 2.

### ICP recipes

A single recipe is used to etch all III/V-based semiconductors, i.e. InGaAs, InP, and InAlAs, in the Oxford Plasmalab 100 Inductively Coupled Plasma (ICP) etcher.

1. The first step in the recipe is a short clean of organic contaminations: O<sub>2</sub> plasma for 1 min.

2. The next step is the actual etch, which is performed in a cyclic manner: after every minute of etching, a descum step is performed to remove the volatile etched material from the chamber. This etch is done at a temperature of 60 °C and chamber pressure of 6 mTorr (or 0.8 Pa) with the gas flows shown in table A.1. The descum step takes 16 s and uses O<sub>2</sub>.
3. Finally, the chamber is purged with an inert gas (Ar) for 1 minute twice.

Table A.1: ICP etch recipes

Material	ICP power	RF power	H <sub>2</sub>	CH <sub>4</sub>	Etch speed
InP	200 W	110 W	10 sccm	30 sccm	80 nm/min
InGaAs	200 W	110 W	10 sccm	30 sccm	30 nm/min

## RIE recipes

Most other materials are dry etched in the Advanced Vacuum Vision 320 Reactive Ion Etcher (RIE). These etches are continuous (no descum step) and do not have a pre- and post-etch purge step with O<sub>2</sub>. All RIE-recipe details are given in Table A.2. Two different SiN<sub>x</sub> recipes are used: the first one is used to etch SiN waveguides in LPCVD SiN, and the second one, including SF<sub>4</sub> as well, is used to etch vias and tethers in PECVD layers of SiN.

Table A.2: RIE etch recipes

Material	Pressure	RF power	Gasses	Etch speed
SiN <sub>x</sub> (1)	20 mTorr	120 W	80 sccm CF <sub>4</sub> + 3 sccm H <sub>2</sub>	30 nm/min
SiN <sub>x</sub> (2)	20 mTorr	120 W	80 sccm CF <sub>4</sub> + 7 sccm H <sub>2</sub> + 3 sccm SF <sub>6</sub>	30 nm/min
BCB	10 mTorr	150 W	5 sccm SF <sub>6</sub> + 50 sccm O <sub>2</sub>	300 nm/min
Photoresist	100 mTorr	75 W	50 sccm O <sub>2</sub>	300 nm/min

## A.2 Wet etch recipes

The following recipes are used for wet etching, as described in Chapter 2.

1. Buffered HF (BHF): a short dip (5s) is performed before the first e-beam lithography step, to ensure good adhesion of the AR-P 6200 resist.
2. HCl:H<sub>3</sub>PO<sub>4</sub>: this acid solution is used to etch InP and has a high selectivity with respect to InGaAs (cathode). Etched for 45 s to finish the mesa etch after ICP etching. And a second 5 s dip was done after the *island* etch (i.e. the InP sub-contact layer).
3. H<sub>2</sub>SO<sub>4</sub>:H<sub>2</sub>O<sub>2</sub>:H<sub>2</sub>O (Piranha): etches InAlAs. This solution was used to anisotropically etch the InAlAs-release layer. A Etched for 60 s to finish the *release* etch after ICP etching.
4. FeCl<sub>3</sub>: etches InAlAs. Make sure the solution is chilled to 5 °C. Used to isotropically underetch the coupons. A single 25 minute release is enough to release all coupons.
5. H<sub>3</sub>PO<sub>4</sub>:H<sub>2</sub>O<sub>2</sub>:H<sub>2</sub>O: alternative to ICP for etching InGaAs. Although it works well, it needs to be timed very carefully as it is not fully anisotropic. Even a few seconds too long results in an undesired undercut of the metal anode contact.
6. HCl: used for quick dips before metallization to remove the native oxides on InGaAs layers.

All wet etch recipes are also summarized in Table A.3

Table A.3: Wet etch recipes

Material	Etchant(s) (ratio)	Etch speed	Comment
InP	HCl:H <sub>3</sub> PO <sub>4</sub> (1:4)	100 nm/min	
InAlAs	H <sub>2</sub> SO <sub>4</sub> :H <sub>2</sub> O <sub>2</sub> :H <sub>2</sub> O (1:1:20)	300 nm/min	Anisotropic
InAlAs	FeCl <sub>3</sub> -solution	500 nm/min (laterally)	Isotropic
InGaAs	H <sub>3</sub> PO <sub>4</sub> :H <sub>2</sub> O <sub>2</sub> :H <sub>2</sub> O (5:1:40)	2.5 nm/min	
InGaAs	HCl:H <sub>2</sub> O (1:20)		

## A.3 Lithography recipes

The following recipes are used for lithography as described in Chapter 2.

### EBL recipes

Most lithography steps are done using high-resolution e-beam lithography (EBL) with the Raith Voyager Electron Beam Nanolithography System.

1. Clean the sample with 20 min O<sub>2</sub>-plasma (TEPLA)
2. Spin coat AR-P 9200.13 for 60 s at 3500 rpm (yields  $\approx$  500 nm)
3. Soft bake for 1 min at 150 °C
4. Spin coat Elektra for 60 s at 2000 rpm
5. Soft bake for 2 min at 90 °C

In some situations, thicker layers of resist were desired, e.g. for etching vias in the SiN encapsulation after printing. For this, a double layer of ARP 6200.18 was spin coated at 2500 rpm for  $\approx$  2  $\mu$ m total resist thickness.

### UV lithography recipes

Lower resolution steps are done using UV lithography. A Suss Microtech Mask Aligner 6 (MA6) is used for alignment and exposure. All optical lithography steps on the source chip are done using the AZ MIR 701 resist, and TI 35E resist is used for metal lift-off on the target samples.

#### AZ MIR701

1. Spin coat for 40 s at 4000 rpm (yields  $\approx$  800 nm)
2. Soft bake for 60 s at 100 °C
3. Expose for 80 s with a 5 mW/cm<sup>2</sup> intensity (vacuum contact)
4. Post-exposure bake for 60 s at 110 °C
5. Develop for 60 s in AZ 726MIF developer (2:1 diluted)

**TI 35E (image reversal)**

1. Spin coat for 40 s at 4000 rpm (yields  $\approx 2 \mu\text{m}$ )
2. Soft bake for 3 min at  $100^\circ\text{C}$
3. Expose for 55 s with a  $5 \text{ mW}/\text{cm}^2$  intensity (vacuum contact)
4. Wait for at least 10 min (rehydration)
5. Post-exposure bake for 3 min at  $125^\circ\text{C}$
6. Flood exposure for 185 s
7. Develop for 60 to 90 s in AZ 400K developer (1:3 diluted)

**A.4 Deposition recipes**

The Advanced Vacuum Vision 310 Plasma-enhanced Chemical Vapor Deposition (PECVD) tool is used for the deposition of SiN layers for passivation and tethering of the photodiode coupons. The recipe used was *Mixed frequency Silicon Nitride* at a deposition temperature of  $270^\circ\text{C}$ , which also encompasses a very short SiOx deposition at the beginning of the recipe. To avoid instant oxidation of the sensitive mesa sidewall, the first SiN deposition was started at room temperature and ramped up to the desired  $270^\circ\text{C}$ .



# References

- [1] G. Roelkens, J. Zhang, L. Bogaert, M. Billet, D. Wang, B. Pan, C. J. Kruckel, E. Soltanian, D. Maes, T. Vanackere, T. Vandekerckhove, S. Cuyvers, J. De Witte, I. L. Lufungula, X. Guo, H. Li, S. Qin, G. Muliuk, S. Uvin, B. Haq, C. Op de Beeck, J. Goyvaerts, G. Lepage, P. Verheyen, J. Van Campenhout, G. Morthier, B. Kuyken, D. Van Thourhout, and R. Baets, "Micro-transfer printing for heterogeneous si photonic integrated circuits," *IEEE Journal of Selected Topics in Quantum Electronics*, vol. 29, no. 3: Photon. Elec. Co-Inte. and Adv. Trans. Print., pp. 1–14, 2023.
- [2] G. Roelkens, J. Zhang, L. Bogaert, E. Soltanian, M. Billet, A. Uzun, B. Pan, Y. Liu, E. Delli, D. Wang, V. B. Oliva, L. T. Ngoc Tran, X. Guo, H. Li, S. Qin, K. Akritidis, Y. Chen, Y. Xue, M. Niels, D. Maes, M. Kiewiet, T. Reep, T. Vanackere, T. Vandekerckhove, I. L. Lufungula, J. De Witte, L. Reis, S. Poelman, Y. Tan, H. Deng, W. Bogaerts, G. Morthier, D. Van Thourhout, and B. Kuyken, "Present and future of micro-transfer printing for heterogeneous photonic integrated circuits," *APL Photonics*, vol. 9, p. 010901, 01 2024.
- [3] J. Goyvaerts, A. Grabowski, J. Gustavsson, S. Kumari, A. Stassen, R. Baets, A. Larsson, and G. Roelkens, "Enabling vcsel-on-silicon nitride photonic integrated circuits with micro-transfer-printing," *Optica*, vol. 8, pp. 1573–1580, Dec 2021.
- [4] Z. Liu, G. Muliuk, J. Zhang, G. Roelkens, N. L. Thomas, and R. Baets, "Micro-transfer printed silicon nitride grating couplers for efficient on-chip light coupling," in *Integrated Optics: Devices, Materials, and Technologies XXVI* (S. M. García-Blanco and P. Cheben, eds.), vol. 12004, p. 1200404, International Society for Optics and Photonics, SPIE, 2022.
- [5] E. Soltanian, G. Muliuk, S. Uvin, D. Wang, G. Lepage, P. Verheyen, J. V. Campenhout, S. Ertl, J. Rimböck, N. Vaissiere, D. Néel, J. Ramirez, J. Decobert, B. Kuyken, J. Zhang, and G. Roelkens, "Micro-transfer-printed

- narrow-linewidth iii-v-on-si double laser structure with a combined 110 nm tuning range," *Opt. Express*, vol. 30, pp. 39329–39339, Oct 2022.
- [6] T. Vanackere, T. Vandekerckhove, L. Bogaert, M. Billet, S. Poelman, S. Cuyvers, J. V. Kerrebrouck, A. Moerman, O. Caytan, N. Singh, S. Lemey, G. Torfs, P. Ossieur, G. Roelkens, S. Clemmen, and B. Kuyken, "Heterogeneous integration of a high-speed lithium niobate modulator on silicon nitride using micro-transfer printing," *APL Photonics*, vol. 8, p. 086102, 08 2023.
- [7] J. Goyvaerts, S. Kumari, S. Uvin, J. Zhang, R. Baets, A. Gocalinska, E. Pelucchi, B. Corbett, and G. Roelkens, "Transfer-print integration of gaas p-i-n photodiodes onto silicon nitride waveguides for near-infrared applications," *Opt. Express*, vol. 28, pp. 21275–21285, Jul 2020.
- [8] M. Tonouchi, "Cutting-edge terahertz technology," *Nature photonics*, vol. 1, no. 2, pp. 97–105, 2007.
- [9] A. Y. Pawar, D. D. Sonawane, K. B. Erande, and D. V. Derle, "Terahertz technology and its applications," *Drug invention today*, vol. 5, no. 2, pp. 157–163, 2013.
- [10] T. Nagatsuma, "Terahertz technologies: present and future," *IEICE Electronics Express*, vol. 8, no. 14, pp. 1127–1142, 2011.
- [11] J. Federici and L. Moeller, "Review of terahertz and subterahertz wireless communications," *Journal of Applied Physics*, vol. 107, no. 11, 2010.
- [12] "Ericsson mobility report," tech. rep., Ericsson, June 2024. Accessed: 2024-08-17.
- [13] "Ericsson microwave outlook report," tech. rep., Ericsson, Oct. 2023. Accessed: 2024-08-17.
- [14] T. Nagatsuma, G. Ducournau, and C. C. Renaud, "Advances in terahertz communications accelerated by photonics," *Nature Photonics*, vol. 10, no. 6, pp. 371–379, 2016.
- [15] H.-J. Song and N. Lee, "Terahertz communications: Challenges in the next decade," *IEEE Transactions on Terahertz Science and Technology*, vol. 12, no. 2, pp. 105–117, 2021.
- [16] D. Maes, E. Peytavit, B. Kuyken, and S. Lemey, "Terahertz communication: a story of bandwidth and silicon photonic integration," in *Faculty of Engineering and Architecture Research Symposium 2022 (FEARS 2022)*, 2022.

- [17] Van den Brande, Quinten, *Highly efficient, ultra-wideband, air-filled substrate-integrated-waveguide antenna technology for next-generation wireless systems*. PhD thesis, Ghent University, 2021.
- [18] D. Maes, G. Roelkens, M. Zaknounge, C. O. de Beeck, S. Poelman, M. Bilet, M. Muneeb, S. Lemey, E. Peytavit, and B. Kuyken, "Heterogeneous integration of uni-travelling-carrier photodiodes using micro-transfer printing on a silicon-nitride platform," in *2021 Conference on Lasers and Electro-Optics Europe and European Quantum Electronics Conference*, p. ck\_4\_3, Optica Publishing Group, 2021.
- [19] D. Maes, S. Lemey, G. Roelkens, M. Zaknounge, V. Avramovic, E. Okada, P. Szriftgiser, E. Peytavit, G. Ducournau, and B. Kuyken, "High-speed uni-traveling-carrier photodiodes on silicon nitride," *APL Photonics*, vol. 8, p. 016104, 01 2023.
- [20] T. J. Kippenberg, A. L. Gaeta, M. Lipson, and M. L. Gorodetsky, "Dissipative kerr solitons in optical microresonators," *Science*, vol. 361, no. 6402, p. eaan8083, 2018.
- [21] C. Xiang, J. Guo, W. Jin, L. Wu, J. Peters, W. Xie, L. Chang, B. Shen, H. Wang, Q.-F. Yang, D. Kinghorn, M. Paniccia, K. J. Vahala, P. A. Morton, and J. E. Bowers, "High-performance lasers for fully integrated silicon nitride photonics," *Nature Communications*, vol. 12, Nov. 2021.
- [22] C. O. de Beeck, B. Haq, L. Elsinger, A. Gocalinska, E. Pelucchi, B. Corbett, G. Roelkens, and B. Kuyken, "Heterogeneous iii-v on silicon nitride amplifiers and lasers via microtransfer printing," *Optica*, vol. 7, pp. 386–393, May 2020.
- [23] S. Lischke, A. Peczek, J. S. Morgan, K. Sun, D. Steckler, Y. Yamamoto, F. Korndörfer, C. Mai, S. Marschmeyer, M. Fraschke, A. Krüger, A. Belling, and L. Zimmermann, "Ultra-fast germanium photodiode with 3-dB bandwidth of 265 GHz," *Nature Photonics*, vol. 15, pp. 925–931, Nov. 2021.
- [24] S. Lischke, D. Knoll, C. Mai, A. Hesse, G. Georgieva, A. Peczek, A. Kroh, M. Lisker, D. Schmidt, M. Fraschke, H. Richter, A. Krüger, U. Saarow, P. Heinrich, G. Winzer, K. Schulz, P. Kulse, A. Trusch, and L. Zimmermann, "Silicon nitride waveguide coupled 67+ ghz ge photodiode for non-soi pic and epic platforms," in *2019 IEEE International Electron Devices Meeting (IEDM)*, pp. 33.2.1–33.2.4, 2019.

- [25] E. Rouvalis, C. C. Renaud, D. G. Moodie, M. J. Robertson, and A. J. Seeds, "Traveling-wave uni-traveling carrier photodiodes for continuous wave thz generation," *Opt. Express*, vol. 18, pp. 11105–11110, May 2010.
- [26] F. Yu, K. Sun, Q. Yu, and A. Beling, "High-speed evanescently-coupled waveguide type-ii mutc photodiodes for zero-bias operation," *Journal of Lightwave Technology*, vol. 38, no. 24, pp. 6827–6832, 2020.
- [27] Q. Yu, J. Gao, N. Ye, B. Chen, K. Sun, L. Xie, K. Srinivasan, M. Zervas, G. Navickaite, M. Geiselmann, and A. Beling, "Heterogeneous photodiodes on silicon nitride waveguides," *Optics Express*, vol. 28, p. 14824, May 2020.
- [28] Q. Chen, X. Zhang, M. S. Sharawi, and R. Kashyap, "Advances in high-speed, high-power photodiodes: From fundamentals to applications," *Applied Sciences*, vol. 14, no. 8, 2024.
- [29] V. Rymanov, A. Stöhr, S. Dülme, and T. Tekin, "Triple transit region photodiodes (ttr-pds) providing high millimeter wave output power," *Opt. Express*, vol. 22, pp. 7550–7558, Apr 2014.
- [30] J.-M. Wun, Y.-W. Wang, and J.-W. Shi, "Ultrafast uni-traveling carrier photodiodes with  $\text{Ga}_{0.5}\text{Sb}_{0.5}/\text{In}_{0.53}\text{Ga}_{0.47}\text{As}$  type-ii hybrid absorbers for high-power operation at thz frequencies," *IEEE Journal of Selected Topics in Quantum Electronics*, vol. 24, no. 2, pp. 1–7, 2018.
- [31] X. Lin, M. Natrella, J. Seddon, C. Graham, C. C. Renaud, M. Tang, J. Wu, H. Liu, and A. J. Seeds, "High performance waveguide uni-travelling carrier photodiode grown by solid source molecular beam epitaxy," *Opt. Express*, vol. 27, pp. 37065–37086, Dec 2019.
- [32] Y. Tian, B. Xiong, C. Sun, Z. Hao, J. Wang, L. Wang, Y. Han, H. Li, L. Gan, and Y. Luo, "Ultrafast mutc photodiodes over 200ghz with high saturation power," *Opt. Express*, vol. 31, pp. 23790–23800, Jul 2023.
- [33] L. Li, L. Wang, T. Long, Z. Zhang, J. Lu, and B. Chen, "Ultra-fast waveguide mutc photodiodes over 220 ghz," *Journal of Lightwave Technology*, vol. 42, no. 21, pp. 7451–7457, 2024.
- [34] P. Latzel, F. Pavanello, M. Billet, S. Bretin, A. Beck, M. Vanwollegem, C. Coinon, X. Wallart, E. Peytavit, G. Ducournau, M. Zaknoune, and J.-F. Lampin, "Generation of mw level in the 300-ghz band using resonant-cavity-enhanced unitraveling carrier photodiodes," *IEEE Transactions on Terahertz Science and Technology*, vol. 7, no. 6, pp. 800–807, 2017.

- [35] J. O'Callaghan, R. Loi, E. E. Mura, B. Roycroft, A. J. Trindade, K. Thomas, A. Gocalinska, E. Pelucchi, J. Zhang, G. Roelkens, C. A. Bower, and B. Corbett, "Comparison of ingaas and inala sacrificial layers for release of in-p-based devices," *Opt. Mater. Express*, vol. 7, pp. 4408–4414, Dec 2017.
- [36] K. M. Gupta and N. Gupta, *Microwave Diodes (Varactor Diode, p-i-n Diode, IMPATT Diode, TRAPATT Diode, BARITT Diode, etc.)*, pp. 285–309. Cham: Springer International Publishing, 2016.
- [37] J. C. Lin, S. Y. Yu, and S. E. Mohny, "Characterization of low-resistance ohmic contacts to n- and p-type InGaAs," *Journal of Applied Physics*, vol. 114, p. 044504, 07 2013.
- [38] G. Muliuk, K. Van Gasse, J. Van Kerrebrouck, A. J. Trindade, B. Corbett, D. Van Thourhout, and G. Roelkens, "4 × 25 gbps polarization diversity silicon photonics receiver with transfer printed iii-v photodiodes," *IEEE Photonics Technology Letters*, vol. 31, p. 287–290, Feb 2019.
- [39] M. Verdun, G. Beaudoin, B. Portier, N. Bardou, C. Dupuis, I. Sagnes, R. Haïdar, F. Pardo, and J.-L. Pelouard, "Dark current investigation in thin p-i-n InGaAs photodiodes for nano-resonators," *Journal of Applied Physics*, vol. 120, p. 084501, Aug. 2016.
- [40] M. Natrella, C.-P. Liu, C. Graham, F. van Dijk, H. Liu, C. C. Renaud, and A. J. Seeds, "Accurate equivalent circuit model for millimetre-wave utc photodiodes," *Opt. Express*, vol. 24, pp. 4698–4713, Mar 2016.
- [41] "De-embedding using scikit-rf." <https://scikit-rf.readthedocs.io/en/latest/tutorials/Deembedding.html#Open-Short-De-embedding>. [Accessed 20-11-2024].
- [42] Rohde & Schwarz, *R&S NRP Power Meter Family Specifications*, May 2010. Version 10.00.
- [43] Virginia Diodes, Inc., *PM5 Operational Manual*, 2016. Version 10.00.
- [44] M. N. Feiginov, "Analysis of limitations of terahertz p-i-n uni-traveling-carrier photodiodes," *Journal of Applied Physics*, vol. 102, no. 8, p. 084510, 2007.
- [45] Keysight Technologies, *Keysight Infiniium UXR-Series Real-Time Oscilloscopes*, Aug 2023. Twentieth edition.
- [46] I. Keysight Technologies, "Evm normalization reference (digital demod)." <https://helpfiles.keysight.com/csg/89600B/Webhelp/>

- [Subsystems/digdemod/content/dlg\\_digdemod\\_comp\\_evmnormref.htm](#). Accessed: 2024-08-08.
- [47] Rhode and Schwarz, "Do you know your evm?" [https://www.rohde-schwarz.com/us/applications/do-you-know-your-evm-application-card\\_56279-787578.html](https://www.rohde-schwarz.com/us/applications/do-you-know-your-evm-application-card_56279-787578.html). Accessed: 2024-08-08.
- [48] R. A. Shafik, M. S. Rahman, and A. R. Islam, "On the extended relationships among evm, ber and snr as performance metrics," in *2006 International Conference on Electrical and Computer Engineering*, pp. 408–411, IEEE, 2006.
- [49] I. T. U. (ITU), "G.975.1: Forward error correction for high bit-rate dwdm submarine systems." <https://www.itu.int/rec/T-REC-G.975.1-200402-I/en>, Feb 2004.
- [50] Q. Cheng, M. Bahadori, M. Glick, S. Rumley, and K. Bergman, "Recent advances in optical technologies for data centers: a review," *Optica*, vol. 5, pp. 1354–1370, Nov 2018.
- [51] A. Rahim, E. Ryckeboer, A. Z. Subramanian, S. Clemmen, B. Kuyken, A. Dhakal, A. Raza, A. Hermans, M. Muneeb, S. Dhoore, Y. Li, U. Dave, P. Bienstman, N. Le Thomas, G. Roelkens, D. Van Thourhout, P. Helin, S. Severi, X. Rottenberg, and R. Baets, "Expanding the silicon photonics portfolio with silicon nitride photonic integrated circuits," *Journal of Lightwave Technology*, vol. 35, no. 4, pp. 639–649, 2017.
- [52] C. O. de Beeck, B. Haq, L. Elsinger, A. Gocalinska, E. Pelucchi, B. Corbett, G. Roelkens, and B. Kuyken, "Heterogeneous III-V on silicon nitride amplifiers and lasers via microtransfer printing," *Optica*, vol. 7, pp. 386–393, 5 2020.
- [53] Q. Hu, R. Borkowski, Y. Lefevre, J. Cho, F. Buchali, R. Bonk, K. Schuh, E. De Leo, H. Patrick, M. Destraz, N. Del Medico, H. Duran, V. Tedaldi, C. Funck, Y. Fedoryshyn, J. Leuthold, W. Heni, B. Baeuerle, and C. Hoessbacher, "Ultrahigh-net-bitrate 363 Gbit/s PAM-8 and 279 Gbit/s polybinary optical transmission using plasmonic Mach-Zehnder modulator," *Journal of Lightwave Technology*, 2022.
- [54] A. Alvarado, E. Agrell, D. Lavery, R. Maher, and P. Bayvel, "Replacing the soft-decision fec limit paradigm in the design of optical communication systems," *Journal of Lightwave Technology*, vol. 33, no. 20, pp. 4338–4352, 2015.



